Special 2-D and 3-D Geometrically Nonlinear Finite Elements for Analysis of Adhesively Bonded Joints

By

Raul H. Andruet

Dissertation submitted to the Faculty of the Virginia Polytechnic Institute and State University in partial fulfillment of the requirements for the degree of

Doctor of Philosophy

in

Engineering Science and Mechanics

APPROVED:

_____	_____
D. A. Dillard, Chairman	S.M. Holzer, Co-chairman
_____	_____
E. R. Johnson	B.J. Love

_____

R. D. Kriz

April, 1998
Blacksburg, Virginia

Special 2-D and 3-D Geometrically Nonlinear Finite Elements for Analysis of Adhesively Bonded Joints

By

Raul H. Andruet
David A. Dillard, Chairman
Siegfried M. Holzer, Co-chairman

Engineering Science and Mechanics

(ABSTRACT)

Finite element models have been successfully used to analyze adhesive bonds in actual structures, but this takes a considerable amount of time and a high computational cost. The objective of this study is to develop a simple and cost-effective finite element model for adhesively bonded joints which could be used in industry. Stress and durability analyses of crack patch geometries are possible applications of this finite element model. For example, the lifetime of aging aircraft can be economically extended by the application of patches bonded over the flaws located in the wings or the fuselage.

Special two and three- dimensional adhesive elements have been developed for stress and displacement analyses in adhesively bonded joints. Both the 2-D and 3-D elements are used to model the whole adhesive system: adherends and adhesive layer. In the 2-D elements, adherends are represented by Bernoulli beam elements with axial deformation and the adhesive layer by plane stress or plane strain elements. The nodes of the plane stress-strain elements that lie in the adherend-adhesive interface are rigidly linked with the nodes of the beam elements. The 3-D elements consist of shell elements that represent the adherends and solid brick elements to model the adhesive. This technique results in smaller models with faster convergence than ordinary finite element models. The resulting mesh can represent arbitrary geometries of the adhesive layer and include cracks. Since large displacements are often observed in adhesively bonded joints, geometric nonlinearity is modeled.

2-D and 3-D stress analyses of single lap joints are presented. Important 3-D effects can be appreciated. Fracture mechanics parameters are computed for both cases. A stress analysis of a crack patch geometry is presented. A numerical simulation of the debonding of the patch is also included.

Acknowledgements

I would like to express my sincere appreciation and gratitude to Dr. S.M. Holzer for his teaching, guidance, patience, friendship, and support. I admire him as a teacher, as a leader, and, above all, as a friend. I also want to express my gratitude to Dr. D.A. Dillard for providing me expert advice in the mechanics of adhesives, and for his support and understanding. I want to extend my gratitude to Dr. E.R. Johnson, Dr. B.J. Love, and R.D. Kriz for serving on the dissertation committee, and to Dr R.H. Plaut for serving on my examining committee.

Aida Mendez-Delgado for her smile, support, care, and for being always there when I needed her.

My infinite gratitude goes to Marcela Ruiz-Funez, Gustavo Maldonado, Daniela Verthelyi and Eduardo Romano for their friendship and hospitality. To them I am forever grateful.

I am grateful to all my friends who made my stay in Virginia an unforgettable experience, to Virgilio Centeno, Tatiana Boluarte, Paul Prato, Clara Diaz, Eduardo Miles, Alberto and Patricia Perez Rigau, Juan Sabate, Margarita, Cristina y Mario Sanchez, Diana Rubio, Mercedes Pastor, Luis Moreschi , Guillermo Aberboch, Daniel Quinones, and many other exceptional friends.

Very special thanks to Jacem Tissaoui, Samruam Tongtoe, and Amara Loulizi . I learned a great deal and was honored to work with them.

My gratitude goes forever to Gail, Siegfried, Mathew, and Michael Holzer for their generosity, friendship, and hospitality, for making me feel at home.

I would like to thank Gustavo Maldonado and Sergio Preidikman for their friendship and the long conversations we had about this work. Special thanks to Azar Alizadeh for her dedication and patient in helping me with my writing, and for being an unconditional friend.

This work was partially supported by CASS, Center for Adhesive and Sealant Sciences.

Finally, I would like to dedicate this work to my family; to my parents, Titi and Nene, to my brothers, Carlos, Luis y Mario, to my sisters in law, Ines, Raquel, and Viviana, and to my nieces and nephews, Florencia, Maria Belen, Tomas, Maria Jose, Agustin, Virginia, and Maria Ines.

Table of Contents

List of Figures

List of Tables

Chapter 1

Introduction

1.1 Background

The use of adhesive bonding has dramatically increased in the past two decades. Adhesives are used extensively to bond metallic and composite components in many fields where structures are subject to high levels of service. The aerospace industry, and particularly aircraft repair, are examples of fields where the application of adhesive bonding is flourishing. Adhesive bonding distributes stresses over the whole bonded region; therefore, stress concentrations are less likely to occur than in conventional fastening techniques. Application of adhesive bonding does not require high temperatures of welding or bracing, which improves the appearance of the joint and reduces its weight. Holes are not required in structural components as in the case for rivets, thereby avoiding reduced cross-sections in the bonded region. In spite of its increasing use and great potential, adhesive bonding presents some inconveniences: it is almost always irreversible, which means that disassembly without damaging the structural components is not easy. Adhesives are usually less resistant to chemical actions, and also are more susceptible to aging than mechanical fastenings.

Summarizing, the use of adhesive bonding is increasing but there are still important issues, such as the durability of the joints, to be better understood. The study of the durability of the joints involves the consideration of a variety of geometries, materials, loading conditions, fatigue, and moisture effects. To perform a durability analysis requires a reliable and efficient analysis tool to obtain stresses, strains, and fracture parameters of bonded joints.

A large variety of models has been developed to analyze adhesively bonded joints. Some of these techniques yield closed-form solutions, which generally involve some symplifying assumptions. Many of them are limited to a certain range of geometries or

loading conditions.

Numerical methods provide a general tool to analyze arbitrary geometries and loading conditions. Among the numerical methods, finite element analysis has been extensively used with success; however, this kind of analysis requires the generation of a large set of data in order to obtain reasonably accurate results. This translates into a large investment in engineering time and computer resources.

1.2 Objectives

The main objective of this study is to develop a finite element model to predict the behavior of adhesively bonded joints. The following features are included:

- A three-dimensional formulation
- The minimization of the number of degrees of freedom to make the element suitable for smaller computers.
- The effect of geometric nonlinearity; adhesively bonded joints are often subjected to large displacements, which alter the load paths.
- The inclusion of fracture mechanics parameters, such as energy release rates.
- The inclusion of a fatigue life prediction law.
- The modeling of the debonding process with reasonable computational effort.
- The inclusion of small moisture effects in the elements.

1.3 Significance

The aim of the proposed research is to produce a simple finite element that will include the most relevant factors of the behavior of adhesively bonded joints with reasonable analysis and computational efforts.

The finite element developed could be included in the element library of a general finite

element program, such as ABAQUS (1997). It could also be part of a small program that could run on a personal computer in a reasonable time. This program could be used by small design and consulting firms that cannot afford large computing facilities. Moreover, this program could be used by engineers who need a quick and relatively accurate estimation of the stresses and displacements of adhesively bonded joints consisting of plates or shell-like adherends.

1.4 Limitations

The present element has a wide range of applications; however, the model is intended to be applied to analyze joints whose adherends are plate or shell-like structures. Relatively stiff epoxy adhesive layers are supposed to glue those adherends.

.

Chapter 2

Literature Review

2.1 Adhesively Bonded Joints

An adhesively bonded joint is a structure composed of two adherends joined by an adhesive. Adams and Wake (1991) define adhesive as “a polymeric material which, when applied to surfaces, can join them together and resist separation” and adherends as members of a structure that are joined together by an adhesive.

There are two basic approaches to analyze adhesively bonded joints: closed-form and numerical solutions. In the first approach, a set of differential equations and boundary conditions is formulated. The solutions of these equations are analytical expressions which give values of stresses at any point of the joint. In the second approach, solutions of differential equations are obtained by numerical methods or the continuum is represented by a discrete model at the outset. In the latter, a system of algebraic equations is derived, commonly from energy functionals. Consequently, no general expressions are obtained for the solution and, therefore, stresses are given at specific points, such as Gauss points. A brief summary of the evolution of closed-form solutions and numerical methods is presented in the next two sections.

2.1.1 Closed-Form Solutions

Many models for adhesively bonded joints were developed using single lap-joint geometries (Fig. 2.1). This configuration has been adopted by the American Society of Testing Materials as a standard mechanical test for the determination of shear strength.

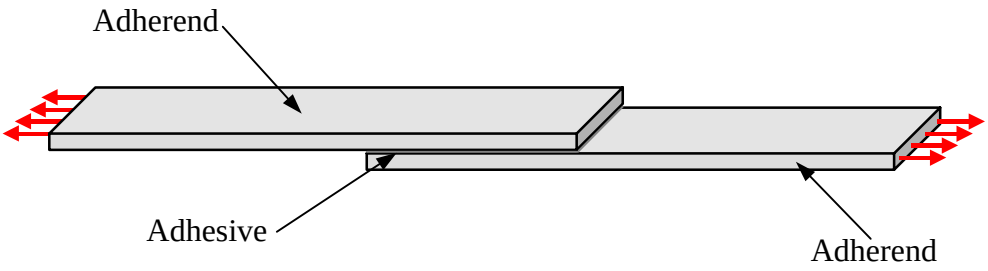

Figure 2.1. Single lap joint configuration.

Single lap joint configurations have been studied for about sixty years and numerous analytical and numerical models have been developed. Volkerson (1938) proposed the first approach, known as the shear lag solution, to analyze this kind of structure. In this model only shear deformation of the adhesive and axial deformation of the adherends are considered. Demarkles (1955) improved the model by including shear deformation of the adherends.

These analyses do not include the bending produced by the eccentric load path. The bending effect results in stresses normal to the adhesive plane, called peel stresses, which are important at the joint edges. Goland and Reissner (1944) were the first to include the effect of the eccentric load path by applying moments at the edges of the joint. These moments were computed considering the geometry, material properties, and acting load. The influence of the adhesive layer was neglected in the calculation of edge moments, so adhesive properties do not appear in the expression proposed by Goland and Reissner (1944). However, geometric nonlinearities are included, for both the outer adherends and the joint overlap. In this landmark work, Goland and Reissner (1944) studied two

bonding cases: rigid adhesive layer and flexible adhesive layer. The first case applies to joints with relatively thin and rigid adhesive layers and the second to joints with relatively thick, flexible adhesive layers.

The most controversial assumption made in this analysis was that the upper and lower adherends within the joint overlap are lumped together. Hart-Smith (1973) formulated a model that basically has the same assumptions as Goland and Reissner's (1944) but the deformations of the upper and lower adherends are considered separately as if they were beams on an elastic foundation. This model neglects the influence of large displacements in the overlap joint. Oplinger (1991) included large deformations of the upper and lower adherends.

Tsai and Morton (1994a) analyzed the influence of large deflections of the overlap joint on the computation of the edge moments. They concluded that the influence of the deflections on the edge moments is negligible if the joint is short. Consequently, Tsai and Morton (1994) asserted that Goland and Reissner's (1944) results are very accurate for short overlaps but not for large overlaps. Although Hart-Smith's (1973) solution is more accurate than Goland and Reissner's (1944), it is still limited to relatively short joints because it does not include large deformations of the overlap joint. Oplinger's model should give the most accurate results for any overlap joint length because the edge moment expression was obtained considering large deflections of all the components of the single lap joint structure.

All of these models have maximum shear stress at the joint edges, which is not realistic since the joint edges are traction-free. This problem was solved by Renton and Vinton (1977) who developed a model whose shear stresses are zero at the edges. Allman (1977) produced a model that allows linear variation of the peel stress through the adhesive thickness and gives zero shear stress at the overlap joint edges. Chen and Cheng (1983) also formulated a two-dimensional model that results in zero shear stresses at the joint edges.

Summarizing, closed-form solutions, such as those presented here for single lap joint, provide a good insight into the behavior of adhesively bonded joints. They are also useful for analysis and planning of tests and for parametric analysis which can lead to the establishment of design criteria. However, the use of these methods in real applications is very limited because they are based on restrictive assumptions and a very limited number of geometries. Most of these methods are not directly applicable to situations where a three-dimensional analysis is required.

2.1.2 Numerical Solutions

The rapid development of computers has made the use of numerical techniques more appealing and feasible. Numerical methods can be used to analyze models with arbitrary geometries and load conditions. They are suitable for the analysis of structures comprised of different materials.

Numerical methods can be applied to solve differential equations which represent structural behavior. Bigwood and Crocombe (1989) used the finite difference method to solve the differential equation that represents the peel and shear stresses in an adhesive layer. Bigwood and Crocombe (1990) included nonlinear effects in the previous work and Crocombe and Bigwood (1992) developed an elasto-plastic analysis of adhesively bonded joints using the same approach.

Another discretization procedure is to divide the structure into small parts and to formulate the model of each one of these parts and then to re-assemble those small parts to model the whole structure. This finite element method is widely used in engineering. The finite element method and its application to the determination of stresses in adhesively bonded joint structures are described in the next section.

2.1.3 Finite Element Solutions

This method has been used in many scientific and engineering fields including fluid flow, heat conduction, and structural analysis. This review is confined to the use of the finite element method for adhesively bonded joints.

Cook et al. (1989) defined the finite element method as a " piecewise approximation in which the approximating function ϕ is formed by connecting simple functions, each defined over a small region." Each small region is called a finite element; the assembly of these elements composes the whole structure to be analyzed. A finite element is " a region in space in which the function ϕ is interpolated from nodal values of ϕ on the boundary of the region…(Cook et al. (1989). These are the two most important features of the finite element method: discretization of the domain and approximation of the solution using the nodal values of the solution on the element boundary. The nodes are points at which the elements are assumed to be interconnected.

Cook et al. (1989) proposed the following steps to carry out the finite element analysis of a structure:

- Divide the structure into finite elements (discretization).
- Formulate the properties of each element, which implies generating the element stiffness matrix.
- Assemble the element matrices to obtain the global finite element model.
- Apply the loads, which sometimes implies generating the nodal loads from some load distribution.
- Apply the boundary conditions.
- Solve the simultaneous linear algebraic equations to determine the nodal displacements.
- Obtain the needed results, which usually are stresses in structural analysis.

The finite element method gives an approximate solution. The accuracy of the solution

depends mainly on the type of element and the fineness of the finite element mesh. The engineer should select the best combination of element complexity and mesh refinement in order to get a solution with the required accuracy.

2.1.4 Two-dimensional Solutions

A large number of two-dimensional finite element analyses of adhesively bonded joints have been performed. While these analyses produce accurate results for some situations and require less modeling effort than three-dimensional analyses, they may still require a considerable amount of data generation and computer time.

The two-dimensional finite element analysis of adhesively bonded joints can be carried out using conventional plane strain or plane stress elements. When this approach is followed, very fine meshes are required, particularly in the adhesive layer, in order to obtain a reasonable accuracy. Wooley and Carver (1971) made one of the first finite element analyses of a single lap joint. They used plane stress elements and their results were comparable with those from the Goland and Reissner (1944) solution. Wooley and Carver (1971) showed stress concentrations at the edges of the overlap joint. Cooper and Sawyer (1979) performed a two-dimensional finite element analysis of a single lap joint using nonlinear plane-stress elements. They modeled the adhesive layer using five rows of elements. Adams and Peppiatt (1973) used a two-dimensional finite element model. They found that an adhesive layer with a spew has lower intensity stress concentrations than a square-edge adhesive layer.

Harris and Adams (1984) developed a geometrically nonlinear finite element that included the elasto-plastic response of adhesive and adherend components. A quadrilateral plane strain element was used for the analysis. They performed the analysis of a standard single lap joint and of a single lap joint with fillets at the edges of the overlaps. Failure conditions were considered using Von Mises' yield criterion for the adherends and the modified Von Mises criterion for the adhesive layer. Their results agreed with those obtained by Goland and Reissner (1944) for the standard single lap

joint and with Allman's (1977) solution for the single lap joint with fillets. Harris and Adams (1984) emphasized the importance of the nonlinear effects in the analysis.

All the cited studies have in common the use of quadrilateral plane stress or plane strain elements. This type of element requires fine meshes to get adequate accuracy. For this reason, efforts have been made to reduce the size of the models. The first approach was made by Yadagiri et al. (1987) who modeled the adhesive layer using only one row of six-node plane elements. As mentioned by Taylor (1996), this approach only reduced the number of degrees of freedom of the adhesive layer. Carpenter and Barsoum (1989) modeled the adherends using two-node beam elements and the adhesive layer by a linear plane element with offset nodes. The number of degrees of freedom is reduced appreciably by this approach because the adherends and the adhesive use the same nodes. The results agreed with the ones from Goland and Reissner's (1944) expressions and other finite element models. The displacements of the adherends were incompatible with the displacements of the adhesive since the former followed a cubic law and the latter a linear one. This produced wholes in the adherend-adhesive interface. Therefore, the convergence was slow and fine meshes were required.

Apparently unknown to Carpenter and Barsoum (1989), Amijima and Fujii (1987) had previously solved this problem by requiring that the displacements in the longitudinal, axial, transverse, and vertical directions are determined by the surface displacements of the adherends. Their model was tested on a single lap joint and on a sandwich cantilever beam. Very good agreement with the theoretical results was achieved using coarse meshes. A similar approach was followed by Taylor (1996); the adherends were modeled by Euler/Bernoulli beams and the adhesive layer by a four-node plane element with offset nodes; the displacement followed a cubic law in the adherend-adhesive interfaces and a linear law in the transverse direction. Again, the results obtained are comparable with those obtained with conventional finite elements using much finer meshes. Another interesting approach was proposed by Adams and Mallick (1992) who modeled adherends and adhesive together by a two node element. The model included plastic deformations, but it can only be used for a single lap and double lap joints.

The flexibility and power of the finite element method is apparent from the number and variety of applications, Jeandrau (1991) used the finite element method to compute stresses in single lap joints and in tubular lap joints in tension and torsion; a finite element code that included elastic, elasto-plastic, and plastic results was used. Chiu and Jones (1992) analyzed single and double lap joints. They made a series of analyses varying the thickness of adherends and adhesive and obtained stress distributions. The objective was to apply this analysis to characterize the adhesive used in the aerospace repair industry. Tsai and Morton (1994a) performed geometrically nonlinear finite element analyses of single lap joints and compared their results with those from analytical solutions, such as that by Goland and Reissner (1944). They explained discrepancies and coincidences among different results.

2.1.5 Three-dimensional Solutions

Stresses in adhesive joints are sometimes obtained with reasonable accuracy from one or two-dimensional analyses. However, there are many cases where a two-dimensional analysis is not applicable or does not produce acceptable accuracy. Even for the standard single lap joint, a three-dimensional analysis may be required if accurate determination of stress variations across the width is desired. Adams and Peppiatt (1973) analyzed the variation of shear stresses along the width and the length of a single lap joint. They found that the distribution of shear stresses is not uniform along the width of the joint and that these stresses are higher at the edges of the joint. Plane-strain analyses gives smaller shear stresses than plane-stress analyses. In a single lap joint, the points that are at the edges of the joint behave as if they were under a plane-stress condition, while the points at the center of the specimen exhibit a behavior close to plane-strain. None of the points of the joint may be under “true” plane-stress or plane-strain conditions. Therefore, the application of two-dimensional analyses does not exactly represent what happens at any point in the structure. Although this may not be a overly significant for a single-lap joint

geometry, it could be significant for cases like crack-patch configurations because three-dimensional effects are very important in this geometry.

In cases where a three-dimensional analysis is required, finite element models are the best tool available. The main advantage in using this method is that no special assumption is needed. The principal disadvantage is the increase of data preparation and computer time. This is shown by Tsai and Morton (1994b) who performed a three-dimensional analysis of a single lap joint using brick elements for the adhesive and the adherend which was a natural extension of the two-dimensional model proposed by the same authors. The modeling required a significant amount of time.

Some attempts to simplify modeling have been made. Richardson et al. (1993) proposed a two-dimensional analysis to represent a three-dimensional behavior. Specifically, a series of three-dimensional analyses were carried out for a range of adhesive joints. From these analyses, equivalent loads were obtained to apply to two-dimensional models which would give stresses closer to those given by three-dimensional models.

Taylor (1996) developed a simplified three-dimensional model of an adhesively bonded joint. The adherends were represented by nine-node Mindlin plate elements and the adhesive was modeled by special brick elements with eighteen offset nodes. Analogous to the two-dimensional model, the adhesive and the adherends share nodes, reducing the number of degrees of freedom of the joint. The displacements of the adherends and adhesive were compatible at the interfaces, so no holes occurred during deformation. Consequently, coarse meshes gave accurate results. Single lap joint and crack-patch geometries were analyzed with this technique. Results showed clearly the variation of peel and shear stresses along the width of the specimen.

2.1.6 Nonlinear Finite Element Methods

From the finite element point of view, an element whose stiffness matrix is not constant is a nonlinear finite element. Equation 2.1 expresses a one degree of freedom

representation of a nonlinear finite element model.

$$P = K(u)u \tag{2.1}$$

where

u = displacement

P = external load

K(u) = stiffness which is a function of the displacement u

Cook et al. (1989) classified the nonlinearities in two main categories:

- Geometric nonlinearity due to large displacements.
- Material nonlinearity due to changes in the material properties.

Bathe (1995) divided geometric nonlinearities in two groups:

- Geometric nonlinearities with small strains: displacements and rotations may be large, but strains are small.
- Geometric nonlinearities with large strains: displacements, rotations, and strains may be large.

The material law can be either linear or nonlinear in both cases. Figure 2.2 illustrates the two geometric nonlinearities.

As a direct consequence of geometrical nonlinearity, the stiffness matrix of the finite element model is not constant, it is a function of the residual displacements. Therefore, an iterative procedure is required to obtain the equilibrium state. For a given load there are two main formulations depending on the configuration to which the variables involved in each step are referred: (1) the total Lagrangian formulation where all variables are referred to the initial configuration; and (2) the updated Lagrangian formulation where all the variables are referred to the configuration at the beginning of the load step considered.

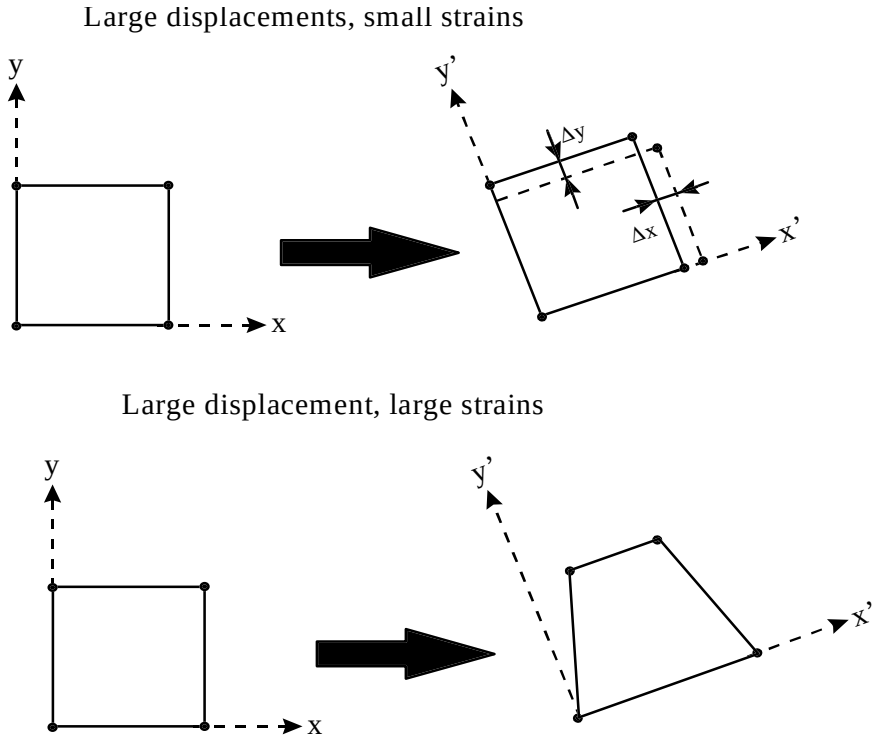

Figure 2.2. Geometric nonlinearities in a finite element: (a) large displacements, small strains; (b) large displacements, large strains.

ABAQUS (1997) and other finite element computer programs use the updated Lagrangian formulation because it is considered numerically more efficient than the total formulation.

The nonlinear finite element analysis consists of a series of linear analyses resulting in successive approximations of the equilibrium state. Hence, it is more time consuming than linear analysis. Although nonlinear analysis has become more feasible with the introduction of powerful computers, it still requires a considerable investment of computer time.

There are several approaches to perform a nonlinear finite element analysis. Most of them divide the total load in steps to track the equilibrium paths. The Newton-Raphson method is widely used in nonlinear analysis. The equilibrium point is approached by successive approximations to reduce the unbalanced load (difference between the applied and the

internal nodal forces) in each iteration. The following expressions relate the displacement variation with the unbalanced load.

$$k_t \Delta u_i = P_B - P_A \tag{2.3}$$

where

k_t = tangent stiffness matrix

Δu_i = displacement increment of the iteration “i”

P_B = applied load

P_A = nodal force

(P_A , u_A) = reference equilibrium state

Figure 2. 3 represents graphically the Newton-Raphson method.

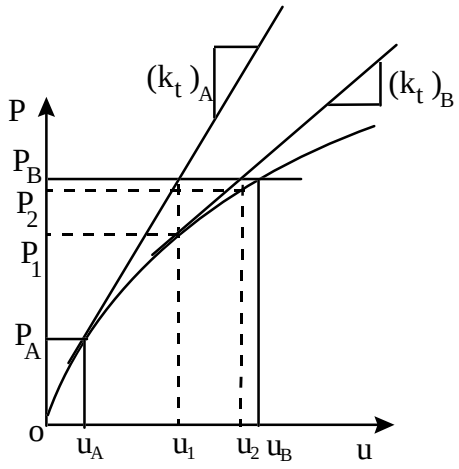

Figure 2.3. Graphical representation of the Newton-Raphson method.

In stability analyses of structures, the Newton-Raphson method tends to diverge in the vicinity of the critical point because the tangent stiffness matrix becomes singular. The Riks/Wempner method, developed independently by Riks and Wempner and is presented by Holzer et al. (1981), overcomes this problem by selecting a generalized arc length that

controls progress along the equilibrium path (Fig. 2.4).

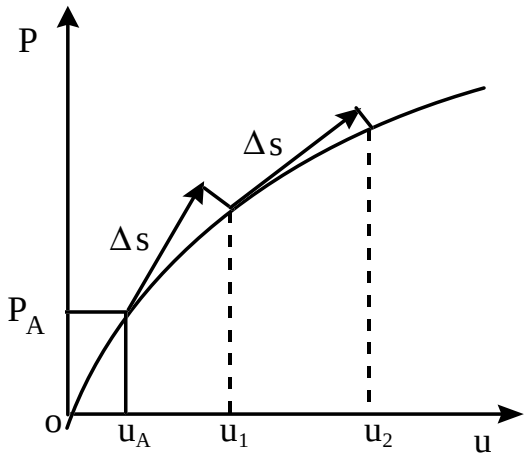

Figure 2.4. Graphical representation of the Riks/Wempner method.

Specifically, the length of the tangent to the equilibrium path, Δs, is prescribed. Each new point is the intersection of the normal plane to the tangent with the equilibrium path. Crisfield (1981) proposed using spherical surfaces with radius Δs and center at the currrent equilibrium point instead of normal planes.

Among the bibliography on nonlinear analysis of adhesive joints, we can cite the work of Harris and Adams (1984) on geometrically nonlinear analysis of single lap joints using plane strain. Their model contains elasto-plastic effects and a failure criterion. Jeandrau (1991) determined stresses in a single lap joint using a finite element model with material nonlinearities. Tsai and Morton (1994b) also performed a geometrically nonlinear finite element analysis of single lap joints using plane strain elements. Bathe (1996) presents a comprehensive and detailed explanation of nonlinear finite element analysis of solid and structural finite elements.

All of these 3-D nonlinear finite element analyses require fine meshes, resulting in a large system of equations that only a powerful computer can solve. This emphasizes the need of simplified methods which reduce the size of the models.

2.2 Crack Analysis Using Finite Elements

Every real material has some defects, cracks, etc. which affect the strength durability of structures. Fracture mechanics is the science that provides the methods, theoretical and experimental, needed to quantify the effect of cracks in structures. Specifically, fracture mechanics provides the tools to determine if a crack is stable and how it might propagate. The literature on fracture mechanics is extensive; the basic concepts of this field, which will be used in this work, are presented in the following paragraphs (Meguid 1989).

The stress intensity factor is one of the key concepts in fracture mechanics. The stress intensity factor is a measure of the "importance" of the flaw. It depends on the mode of loading and the geometry of the specimen; its computation is derived from elasticity considerations. Figure 2.5 shows the three modes of loading traditionally used in fracture mechanics analysis.

To assess if the crack is stable, the stress intensity factor is compared with the toughness of the material, sometimes referred to as the critical stress intensity factor. The crack will extend if the toughness is smaller than the stress intensity factor. Values of toughness are experimentally obtained and tabulated for different materials. There are tables of stress intensity factors for different geometries and load conditions, but unfortunately only relatively simple cases are covered.

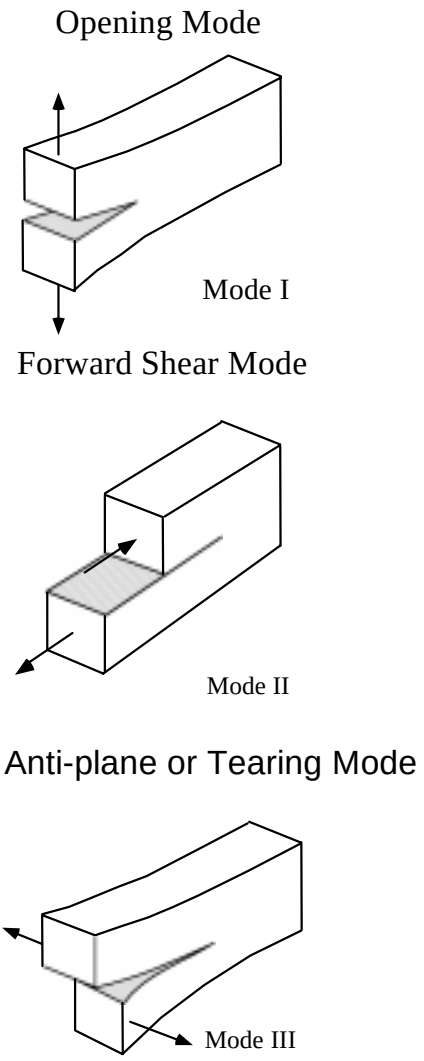

Figure 2.5. Three fractures modes.

For loading mode I the stress intensity factors are related to displacements and stresses as follows:

$$u_i = \frac{K_I}{G}\sqrt{\frac{r}{2\pi}}\, f_i(\theta,\mu) \qquad (2.4)$$

$$\sigma_{ij} = \frac{K_I}{\sqrt{2\pi r}} f_{ij}(\theta) \tag{2.5}$$

where

u_i = displacement

K_I = stress intensity factor

G = shear modulus

ν = Poisson's ratio

r, θ = cylindrical coordinates of a generic point (Fig. 2. 4)

f_i = function of angle θ and Poisson's ratio ν

f_{ij} = function of angle θ and Poisson's ratio ν

Equation 2.5 shows that the stress grows indefinitely as r approaches zero (crack tip). In an actual structure, this is not the case because there is a plastic region in the neighborhood of the crack tip.

Griffith postulated that a crack is unstable when the elastic strain energy per unit of area exceeds the surface energy of the material. This is the basis of the strain energy release rate approach. Mathematically, the strain energy release rate for displacement control is defined as

$$G = -\frac{dU}{da} \tag{2.6}$$

where

G = strain energy release rate

U = strain energy

a = crack extension

The strain energy release rate can be specialized for three loading modes as follows:

$$G_I = \frac{(\kappa+1)}{8\nu} K_I^2 \tag{2.7}$$

$$G = -\frac{dU}{da} \tag{2.8}$$

$$G_I = \frac{(\kappa+1)}{8\nu} K_I^2 \tag{2.9}$$

where

$$\kappa = \begin{cases} 3-4\nu & \text{for plane strain} \\ \dfrac{3-\nu}{1+\nu} & \text{for plane stress} \end{cases}$$

The strain energy release rate is a concept valid only for linear elastic materials. When a crack occurs, a plastic region is generated at the crack tip. Depending on the size of that plastic region, the concept of strain energy release rate cannot be applied directly, but the energy balance must still be achieved. To account for large plastic regions, Rice (1968) proposed using the path independent integral, called the J-integral:

$$J = \int_{\Gamma} \left(U dy - t_i \frac{\partial u_i}{\partial x} ds \right) \tag{2.10}$$

where

U = strain energy density

t_i = traction vector

u_i = displacement vector

ds = differential element of arc Γ

Figure 2.6 shows the elements of the J integral definition. Under certain restrictions, the J-integral is valid for plastic behavior. One restriction is monotonically increasing loads without any unloading. In this case the J-integral represents the input of energy to the system but not the amount of energy recoverable on unloading.

The most important feature of the use of the path-independent J-integral is the fact that the characterization of discontinuities of stresses or strains can be obtained from results

of integrals over a path lying at some distance from the discontinuity.

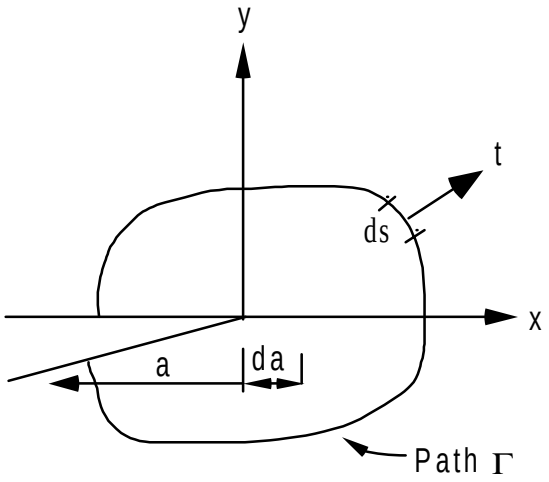

Figure 2.6. J-integral notation and parameters.

2.2.1 Two-dimensional Crack Analysis

The computation of stress intensity factors and strain energy release rates is not an easy task when a complex structure is considered; in this case a numerical approach is required. The finite element method has been used for fracture mechanics parameter calculations with remarkable success.

The first task consists of modeling the singularity using finite elements. The first attempts involved ordinary finite elements with fine meshes (Chan et al. 1970). Linear elements were used which gave constant stresses over the elements. Although the use of higher-order elements improved the results obtained with linear elements, there was a need for a more realistic representation of the stresses inside the cracked elements. As mentioned by Owens and Fawkes (1983), the first approach was made by Tracey (1971) who developed a triangular element with a polynomial representation of the displacements. Tracey and Cook (1977) extended the model to quadrilateral elements. They modeled a singularity of order r^{-p} using a potential function of order p for the

displacements. Other approaches to model singularities by special displacement functions are given by Akin (1976) and Benzley (1974). A breakthrough was introduced independently by Henshell and Shaw (1975) and Barsoum (1976) who developed a method to model a singularity of order $r^{--1/2}$ for the stresses at the crack tip. The method consists of displacing the mid-side nodes of a rectangular quadratic plane element to the quarter positions next to the crack tip as shown in Fig. 2.7.

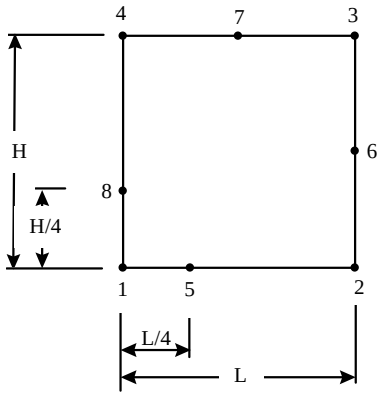

Figure 2.7. Quarter-point two dimensional continuum finite element

This element is called a quarter-point or singular element. Quarter-point elements give a singularity $r^{-1/2}$ for the stresses but only along the two sides containing the displaced nodes. Approaching the crack tip along any other direction will not necessarily give an $r^{1/2}$ singularity for the stresses. Barsoum (1976) solved this problem by collapsing a quadrilateral element into a triangular element. This is done by coalescing the nodes next to the crack tip (Fig. 2.8). This approach produces an $r^{-1/2}$ singularity along rays emanating from the crack tip.

A quarter-point element produces a stress singularity of type $r^{-1/2}$ exactly at the crack tip. If the middle point is moved away from the quarter position, the singularity moves too. If the point is exactly at the midpoint of the element's side, the singularity moves to a point infinitely distant, effectively resulting in a non-singular element.

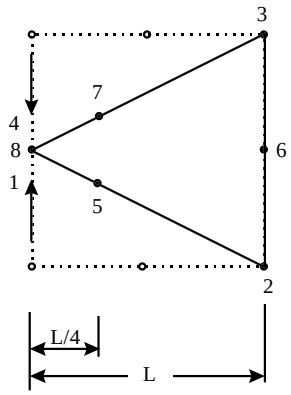

Figure 2.8. Collapsed quarter-point two dimensional continuum finite element

Another approach is the use of analytical solutions to model the whole crack field, not only the singularity at the tip. Only one element models the crack region and the position of the crack can be modified during the crack extension procedure. Byskov (1970) used this approach by modeling the stresses with special complex functions developed by Muskhelishvili (1963). Although equilibrium is satisfied over the element, compatibility between displacements of the cracked and the uncracked elements is not achieved. Rao et al. (1971) used analytical solutions to model the presence of a crack in a continuum. In that study the regions with stress concentrations were modeled with "primary" elements, which can include singularities, and the remaining structure was modeled with "secondary" elements, namely ordinary plane finite elements.

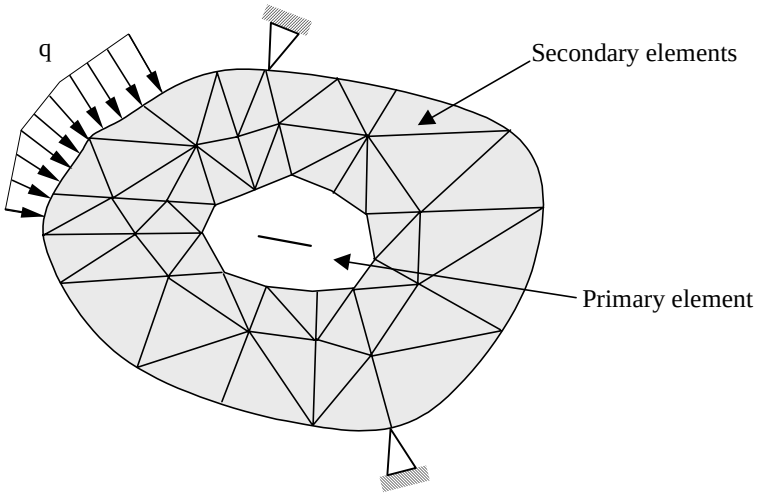

Figure 2.9. Arbitrary body with a region with a stress concentration.

Recently, Davidson et al. (1995) developed an analytical crack-tip element to predict energy release rates for interfacial fracture problems. This approach combined the analytical solution with the results from a finite element analysis.

The cited formulations satisfy internal equilibrium and compatibility conditions but do not satisfy compatibility of displacements between the singular elements and the elements surrounding them. To solve this problem, the displacements of the boundary between ordinary and singular elements are forced to be equal by using Lagrange multipliers in the energy formulation. Finite elements derived using this method are called hybrid elements. Tong et al. (1973) used this approach to handle crack analysis of plane structures. They modeled the cracked region with a super-element that included the singularity associated with the crack. The method yielded compatibility between the displacements of the cracked super-element and the ordinary finite elements surrounding it. Aminpour and Holsapple (1991) developed a hybrid-displacement finite element to analyze a propagating crack at the interface of two materials. The analysis included anisotropic materials and remeshing of the structure to simulate the propagating crack.

Once a good representation of stresses is achieved, the next step is to compute fracture mechanics parameters, particularly stress intensity factors or strain energy release rates. There are numerous ways to compute stress intensity factors using finite element methods. They are summarized as follows:

- Displacement approach: it consists of correlating the analytical expressions for the displacements with the values obtained from the finite element model (Meguid, 1989). Therefore, using Eq. 2.4, one obtains the stress intensity factor for mode I as

$$K_I = \sqrt{\frac{2\pi}{r}} \frac{G}{f_i(\theta, \nu)} u_i^* \tag{2.11}$$

where

u^*_i = displacements of a node i with coordinates r and θ from the finite element analysis.

This value is as accurate as the displacements obtained from the analysis. Extrapolations are used in order to improve the results. Stress intensity factors for the other loading modes can be obtained using the same approach.

- Stress approach: it is basically the same procedure as the displacement approach except the stress expressions are correlated with the stresses from the finite element analysis. Thus, the stress intensity factor can be obtained from Eq. 2.5 as

$$K_I = \frac{\sqrt{2\pi r}}{f_{ij}(\theta)} \sigma^*_{ij} \tag{2.12}$$

where σ^*_{ij} are the stresses of a node with coordinates r and θ.

- Stress energy release method: from the definition of strain energy release rate for displacement control

$$G = -\frac{dU}{da} \tag{2.13}$$

the following approximation can be:

$$G = -\frac{\delta U}{\delta a} = -\frac{U_2 - U_1}{\Delta a} \tag{2.14}$$

where

U_1 = strain energy of the original crack configuration

U_2 = strain energy of the extended crack configuration

Therefore, two finite element meshes must be analyzed: the original one and another one with the crack extended by a distance Δa.

- Virtual crack extensions method: the main objective is to avoid two analyses of the

complete structure to obtain strain energy release rates. The method consists of doing a finite element analysis of the whole structure for the original crack configuration and finding the values of ΔK (K= stiffness matrix) for a crack extension Δa and storing these values so that they can be used in the subsequent crack extensions. In this way, a numerical procedure is postulated that requires only one analysis of the successive crack extensions. The values of ΔK need to be stored only for the elements with a node in the crack tip. Hellen (1975) provided a simple expression for computing dK/da as the summation of scalar terms derived from the reduction of the system of equations by Gauss elimination. Haber and Koh (1985) formulated an explicit expression for energy changes due to virtual crack extensions. The crack singularity was modeled using quarter point elements and the remaining structure by ordinary isoparametric solid elements. The method seems to give accurate results even for relatively coarse meshes.

Hellen (1989) expanded the application of the virtual crack extension method to nonlinear elastic materials. Using incremental theory, elasto-plastic material conditions can be modeled.

Barbero and Reddy (1992) proposed the Jacobian derivative method, a variation of the virtual crack extension method, to obtain the displacements and, from them, the stress intensity factors. This method needs a single finite element analysis and does not require a definition of a virtual crack extension. The motivation for the study was the analysis of delamination problems in composite laminates. The basic idea of the method is that the potential energy depends only on the displacements and the nodal coordinates. This is true in isoparametric elements because displacements and coordinates are interpolated using the same functions. The authors applied the procedure to two and three-dimensional problems.

- J-integral method: Performing the numerical integration of Eq. 2.10, values of strain energy release rates are obtained for the linear case. These values are related to the stress intensity factor by the following expression:

$$K = \left(\frac{8\mu J}{1+\kappa} \right)^{1/2} \tag{2.15}$$

To discriminate between K_I, K_{II}, and K_{III}, the integral must be evaluated for the three loading cases. Each case produces either mode I, II, or III.

An innovative approach presented by Rybicki and Kanninen (1977) is based on the crack closure integral postulated by Irwin. This method, called the modified crack closure integral, is based on the finite element discretization of the crack closure integral and the following expressions:

$$G_I = \lim_{\Delta a \to 0} \frac{1}{2\Delta a} F_c (v_c - v_d) \tag{2.16}$$

$$G_{II} = \lim_{\Delta a \to 0} \frac{1}{2\Delta a} T_c (u_c - u_d) \tag{2.17}$$

where

F_c = force needed to close the crack in the vertical direction

T_c = force needed to close the crack in the horizontal direction

u_c, u_d = horizontal displacement of nodes c and d

v_c, v_d = vertical displacement of nodes c and d

Δa = crack extension

All components of Eqs. 2.16 and 2.17 are shown in Fig. 2. 8.

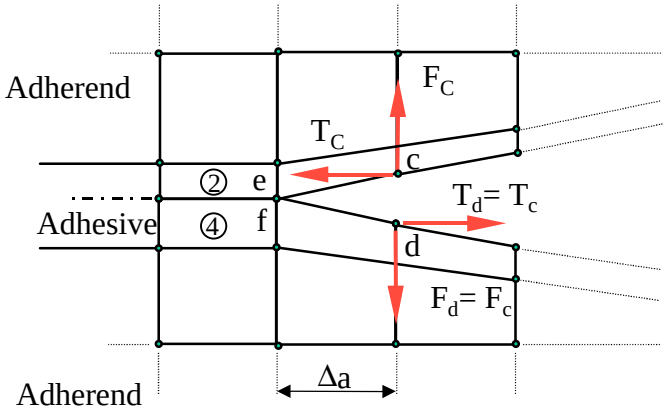

Figure 2.10. Modified crack closure integral method parameters and notation.

To apply this method, a fine mesh should be used to model the neighborhood surrounding the crack tip. Elements 2 and 4 have different nodes (e and f, respectively) at the crack tip (Fig. 2.10). However, they are connected by strong springs acting in the horizontal and vertical directions. From these springs, which do not allow the nodes to separate from each other, the forces T_c and F_c are obtained. The results of this method show good agreement with other solutions. Many researchers have used the modified crack closure integral since it was published in 1987. Badari Narayana et al. (1994) applied this method to three-dimensional cases using 8-node brick elements. Weissberg and Arcan (1992) used this method to investigate the influence of the adhesive stiffness on the behavior of adhesive bonded joints. They analyzed the influence of a crack-tip on the stress intensity factor singularity and the stress concentration factor of a free adhesive edge singularity.

Belytschko and co-workers (1994) applied the element-free Galerkin method to problems of fracture and static crack growth. Element-free Galerkin methods are used for solving partial differential equations that require nodal and geometry data but element connectivity is not needed. The authors discussed two main approaches for the solution of growing cracks: (1) finite element methods with re-meshing and boundary element methods; and (2) finite element methods with re-meshing involving a large amount of programming and codification effort. Belytschko et al. (1994) state that “it is almost impossible to automatically re-mesh finite elements about arbitrarily growing cracks.”

Boundary element methods avoid a large part of the re-meshing, but the requirement of Green functions limits the scope of the problems they can solve. The basic idea of the element-free Galerkin methods is the use of moving least-squares interpolation functions. Belytschko et al. (1994) extended the element-free Galerkin method to the problems of arbitrary crack growth using a moving array of nodes around the crack tip. Specifically the authors developed a strategy that requires 20 nodes about the crack tip and a problem dependent number of nodes behind the crack tip. Special strategies were developed for dealing with essential boundary conditions. The method was applied to edge cracks and cracks emanating from circular holes. In both cases, two-dimensional analyses were performed and excellent results were obtained.

The literature contains various approaches for computing strain energy release rates. To establish a basis for comparison, Johnson (1987) asked a group of researchers to obtain values of strain energy release rates for two crack-lap shear geometries. The participants in the ASTM round-robin were free to select the method of their preference. They were also free to use more than one method. Two closed-form solutions, three linear finite element analyses, four geometrically nonlinear finite element analyses, and one mixed solution combining beam theory with linear finite element analysis were collected. Only one solution was obtained by a three-dimensional finite element analysis. Three-dimensional effects and nonlinearities were shown to play important roles in the behavior of the studied geometry.

2.2.2 Three-dimensional Crack Analysis

In some cases, the third dimension of the crack cannot be neglected. For example, configurations with through, part-through, or embedded cracks require three dimensional analysis. Moreover, cracks in thick solids and cracked structures with arbitrary shapes generally present important three-dimensional effects. Therefore, the effect of cracks in such geometries cannot be predicted by analytical expressions or two-dimensional finite elements; thus three-dimensional finite elements are required.

The need for the computation of fracture mechanics parameters for three-dimensional cases was already addressed in the early 1970's. Hellen (1975) gave values of stress intensity factors for a cracked plate using the virtual crack extension method. This method required two finite element analyses for two crack configurations. The virtual crack extension method was later extended to account for material nonlinearities (Hellen, 1989).

A further variation of the virtual crack extension method was postulated by Nikishkov and Atluri (1987). The equivalent domain integral method was aimed at finding values of the J-integral for a general three-dimensional case. In this method, the J-integral and strain energy release rate for mode III are redefined as follows:

$$J_k f = -\int_A \left(W n_k - \sigma_{ij} \frac{\partial u_i}{\partial x_k} n_j \right) s \, dA \tag{2.18}$$

$$G_{III} f = -\int_A \left(W^{III} n_1 - \sigma_{3j} \frac{\partial u_3}{\partial x_1} n_j \right) s \, dA \tag{2.19}$$

where

s = arbitrary continuous function which is zero on the outer boundary of A

f = area under s

A = integration surface; it is divided into A_o and A_e

Figure 2.11 shows a possible s-function.

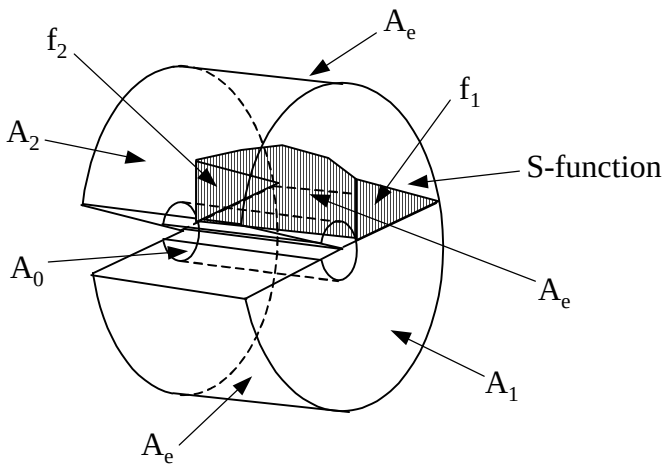

Figure 2.11. Virtual crack extension method (from Nikishkov and Atluri 1987).

By selecting an appropriate arbitrary function s and by using the divergence theorem, values for J_I, J_{II}, and G_{III} can be obtained. These values can then be used in the expressions given by Hellen (1975) to compute K_I, K_{II}, and K_{III}.

Barbero and Reddy (1990) used a Jacobian derivative method for the computation of three-dimensional cases. This method is appealing because of its generality and computational simplicity. The authors presented the analysis of a cylinder with a circular crack in the surface. Good agreement between their results and a well known analytical expression was found.

Badari Narayana et al. (1994) showed that the modified crack closure integral method can be used for three-dimensional analysis. They developed a procedure for the derivation of the modified crack closure integral method for eight-node brick elements. They presented the derivation on the basis of virtual crack closing over the full elemental area in the plane of the crack. This approach gives average values of strain energy release rates over each elemental length along the crack front. They introduced the concept of sub-area integration in which the crack front inside the element is divided into a number of segments. Therefore, on the basis of the same approach, strain energy release rates at several points inside the element can be computed without refining the finite element mesh. Two standard problems were presented as examples: a thick center-cracked tension

specimen and a semi-elliptical surface crack in a thick slab. Fast convergence and accurate results were obtained. This method can be applied to linear and nonlinear cases, and no special elements are required. Its computational simplicity is an additional advantage.

Some other researchers worked in the application of the modified crack closure integral method to three-dimensional problems. For example, Shivakumar et al. (1988) obtained modified crack closure integral method expressions for eight- and twenty-node brick elements. Derivations of modified crack closure integral expressions for different kind of elements can be found in the literature, such as triangular elements Buhholz (1984) as referred into Badari Narayana (1994).

2.3 Fatigue Life Prediction of Adhesively-Bonded Joints

Structures subjected to cyclic loads are prone to fail under loads smaller than the predicted critical static load. This phenomenon, called fatigue, produces slow crack growth at stress intensity factors lower than the critical value. Fracture mechanics parameters, such as the stress intensity factor, are related to fatigue crack growth. It was experimentally found that for cracked specimens subjected to cyclic loads, the stress mean value has an important impact on the crack growth rate per cycle. Lin and Liechti (1987) stated that for adhesively bonded joints, the correlation between debond growth rates and the change in the stress intensity factor has the same sigmoidal shape as the fatigue crack propagation in metals. Meguid (1989) showed the relation between fatigue crack propagation rate, da/dN, and the stress intensity range, $\Delta K = K_{max} - K_{min}$ (Fig. 2.10), for the Paris-Erdogan equation.

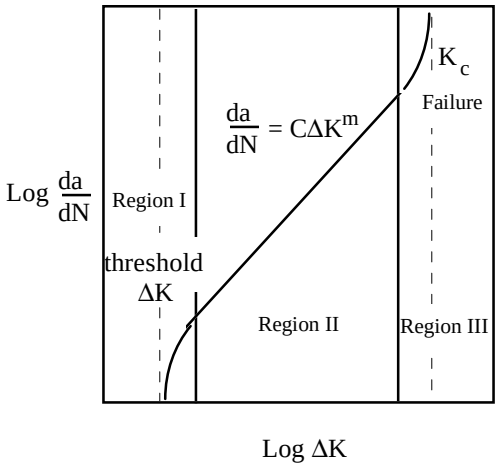

Figure 2.12. Fatigue crack extension law.

Three regions are displayed in Fig. 2.12: in region I the existence of a threshold value below which there is no fatigue failure is shown; in region II the relation between the log(ΔK) and log(dN/da) is practically linear. Finally, in region III there is fast crack growth rate. In this region, K_{max} is close to K_c. Therefore, the crack extension is produced by the failure mechanism $K_{max} > K_c$. The shape of this curve, called the crack growth rate curve, is valid for most materials, and it is obtained by fitting measured crack growth rates.

There have been many attempts to model the relation between the fatigue crack propagation rate, da/dN, and the stress intensity range. The relation most commonly found in the literature was given by Paris and Erdogan (1963):

$$\frac{da}{dN} = C(\Delta K)^m \tag{2.20}$$

where m and C are related material-dependent constants. This equation is valid only in region II of the crack growth rate curve and does not take into account the effect of the mean stress. Forman et al. (1967) improved the model to account for the influence of the mean stress:

$$\frac{da}{dN} = \frac{C(\Delta K)^m}{(1-R)K_c - \Delta K} \tag{2.21}$$

where

R = $\sigma_{max}/\sigma_{min}$

K_c = critical stress intensity factor

Ewalds and Wanhill (1984) postulated the following equation that models the complete crack growth rate curve:

$$\frac{da}{dN} = C(\Delta K)^m \frac{C(\Delta K)^m}{(1-R)K_c - \Delta K}\left[\frac{1-\left(\frac{\Delta K_{th}}{\Delta K}\right)^{n1}}{1-\left(\frac{K_{max}}{K_c}\right)^{n2}}\right]^{n3} \tag{2.22}$$

where n1, n2, and n3 are material-dependent constants.

Fatigue in adhesively bonded joints was first studied by Mostovoy and Ripling (1975) and Brussat and Chiu (1978) (as cited by Lin and Liechti 1987). They concluded that linear fracture mechanics gives reasonable accuracy in the description of debond crack growth due to fatigue. Dattaguru et al. (1984) showed that nonlinearities played an important role in these types of joints.

Lin and Liechti (1987) correlated debond growth rates to strain energy release rates for four specimens. They found that geometrically nonlinear analysis was needed for the computation of energy release rates. Similarity was found in debond growth rate curves for three of the specimens studied. The fourth specimen presented a different shape for the debond growth rate curve.

Kinloch and Osiyemi (1993) used a double cantilever beam to correlate experimentally measured crack growth rates with analytically obtained strain energy release rates. A fatigue crack growth rate curve was determined with this data and used for fatigue life prediction of single-lap joint specimens. Good agreement between the predicted and

experimental results was found.

The analysis of adhesively bonded composite crack-patch repair of a metallic structure (Fig. 2.13) is of special interest. This kind of scenario can be found in aging aircraft and ships. A bonded composite patch retards crack growth, and thus extends the life of the structure at a relatively low cost.

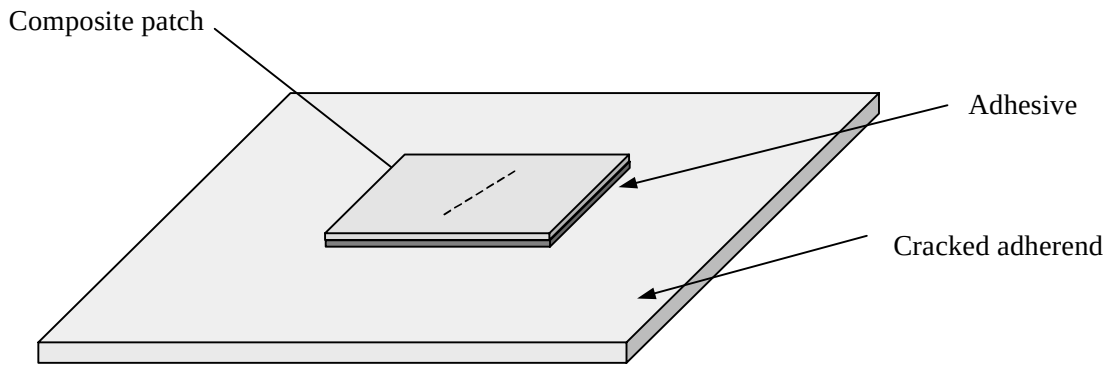

Figure 2.13. Crack-Patch repair configuration.

Some work has been done on crack-patch configurations. Naboulsi and Mall (1997) studied thermal effects on a cracked plate repaired with a composite patch, adhesively bonded. Due to the mismatch of stiffness matrices and thermal expansion coefficients of the three components, large stresses developed within the adhesive layer. Because of the small thickness of the adhesive layer, a conventional finite element analysis required a large number of elements across the thickness of the adhesive. For this reason, the authors used an approach called the three-layer model. This technique consists of modeling the adherends, the cracked plate and the composite patch, and the adhesive layer with Mindlin plate elements with transverse shear deformation. Constraint equations were used to enforce compatibility at the adhesive/adherend interfaces. Two configurations were studied: a single sided repair, and a double sided repair. Three patch materials, boron/epoxy, graphite/epoxy, and glare were used to study the influence of stiffness and thermal coefficients mismatch among the different structural components. Strain energy release rates were computed using the modified crack closure integral

method extended to three-dimensional configurations. The three-layer-model method was validated with previous results and conclusions were obtained from different analyses.

Chapter 3

Geometrically Nonlinear Finite Element Formulation

3.1 Introduction

A geometrically nonlinear finite element model is formulated, which is valid for the following isoparametric elements used to model adhesively bonded joints: 2-D and 3-D continuum elements and a shell element. The components of these elements, such us strain-displacement matrices, are formulated in separate chapters. They are used to compute the stiffness matrices of the elements.

3.2 Incremental Deformation of a Continuum

The present formulation is an adaptation of the one presented by Bathe (1996). When a body is subjected to large displacements, its position is described by the three coordinates and a time variable, t. This variable can represent real time or simply a measure of progress along the equilibrium path.

Consider a body in a stationary Cartesian coordinate system subjected to large displacements as shown in Fig. 3.1. P is a point in the body with a volume V and surrounding surface A. The goal is to evaluate the equilibrium configuration at time $t+\Delta t$. Solutions for all variables are assumed to be known for all configurations at discrete times from 0 to t. Once the equilibrium configuration is found at time $t+\Delta t$, the solution procedure is applied repeatedly until the final configuration is achieved. Therefore, the equilibrium path of the body from one configuration to the other can be traced. Such description of motion, where the body is tracked from the initial to the final configuration, is called Lagrangian or material formulation. This approach is generally used in the analysis of solids. In contrast, the Eulerian formulation where attention is centered in the motion of material through a stationary volume control, is used in the analysis of fluids problems.

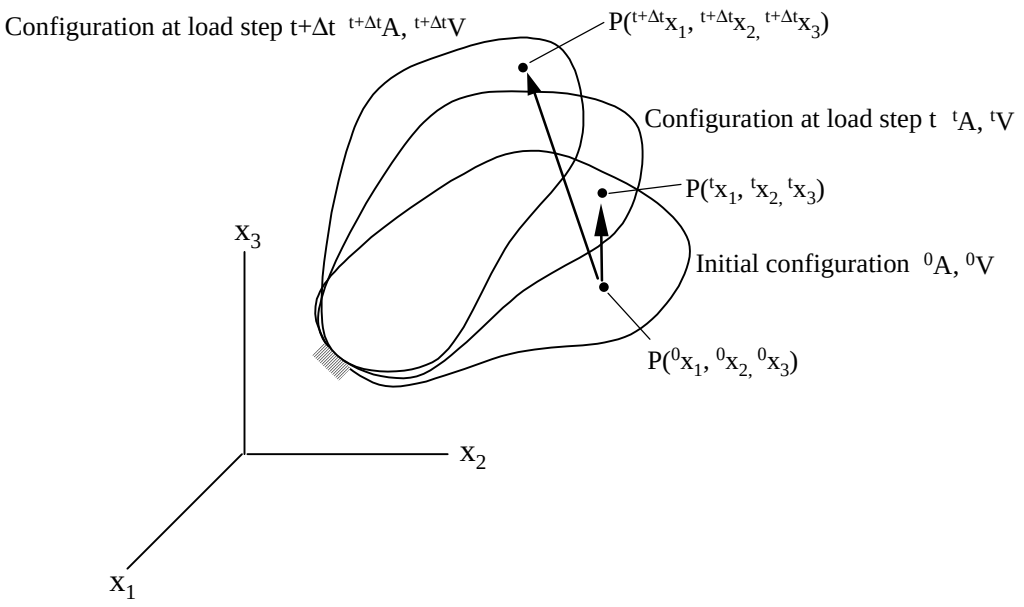

Figure 3.1 Large displacements of a body in stationary Cartesian coordinate system.

In the Lagrangian incremental analysis approach, equilibrium is established using the principle of virtual work. Accordingly, the configuration at time t+Δt is in equilibrium if

$$\int_{{}^{t+\Delta t}V} {}^{t+\Delta t}\tau_{ij}\, \delta\, {}_{t+\Delta t}e_{ij}\ {}^{t+\Delta t}dV = {}^{t+\Delta t}\Re \tag{3.1}$$

where

${}^{t+\Delta t}\tau_{ij}$ = Cauchy stress tensor at time t+Δt

$\delta_{t+\Delta t}e_{ij}$ = virtual strain tensor at time t+Δt

${}^{t+\Delta t}dV$ = differential volume at time t+Δt

${}^{t+\Delta t}\Re$ = virtual work of the external loads at time t+Δt

If body and surface forces are applied, ${}^{t+\Delta t}\Re$ is defined as

$${}^{t+\Delta t}\Re = \int_{{}^{t+\Delta t}V} {}^{t+\Delta t}f_i^B \delta u_i\, d^{t+\Delta t}V + \int_{{}^{t+\Delta t}V} {}^{t+\Delta t}f_i^S \delta u_i^S\, d^{t+\Delta t}S \tag{3.2}$$

where

${}^{t+\Delta t}f_i^B$ = components of externally applied body forces at time t+Δt

${}^{t+\Delta t}f_i^S$ = components of externally applied surface tractions at time t+Δt

$d^{t+\Delta t}S$ = differential surface at time $t+\Delta t$

δu_i^S = component of virtual displacements of surface ${}^{t+\Delta t}S$

In this work, Bathe's (1996) notation is used in the formulation of the geometrically nonlinear finite element model. The left superscript refers to the configuration of the body and the right subscript to the coordinate axes. Therefore, the position of a generic point in the body at time t = 0 is defined by the three coordinates ${}^0x_1$, ${}^0x_2$, ${}^0x_3$; the same point at time t is defined by ${}^tx_1$, ${}^tx_2$, ${}^tx_3$. The displacements of a point in the body at time t + Δt are defined by ${}^{t+\Delta t}u_1$, ${}^{t+\Delta t}u_2$, ${}^{t+\Delta t}u_3$. The following definitions are used:

$$u_i = {}^{t+\Delta t}u_i - {}^tu_i$$
$${}^tx_i = {}^0x_i + {}^tu_i$$
$${}^{t+\Delta t}x_i = {}^0x_i + {}^{t+\Delta t}u_i$$
$${}^{t+\Delta t}x_i = {}^tx_i + u_i$$

A left superscript indicates in which configuration the quantity occurs, and a left subscript refers to the configuration relative to which the quantity is measured. So ${}^{t+\Delta t}_{t}\tau_{ij}$ means the "i,j" component of the Cauchy stress tensor at time $t+\Delta t$ referred to the configuration at time t. If the quantity occurs in the same configuration in which it is measured, the left subscript is not used. So the "i,j" element of the Cauchy stress tensor at time t referred to the configuration at time t is expressed as ${}^t\tau_{ij}$.

Derivatives are also presented in the formulation and a convenient notation must be established to represent them. In this work a comma is used to denote differentiation with respect to the cordinate following the comma. So, the derivative of the displacement u_i at time $t+\Delta t$, measured in the configuration at time 0 with respect to the coordinate x_j is expressed as

$${}^{t+\Delta t}_{0}u_{i,j} = \frac{\partial {}^{t+\Delta t}u_i}{\partial {}^0x_j}$$

There is a basic difficulty in the solution of Eq. 3.1: the configuration at time t+Δt is unknown, and so are the Cauchy stresses and the strains which cannot be referred to an unknown configuration. Cauchy stresses at time t+Δt cannot be computed by simply adding the incremental stresses to the Cauchy stresses at time t.

Problems due to changes in the configuration of a body subjected to large displacements can be resolved by using appropiate strain and stress measures and constitutive relations (Bathe 1996). Specifically, Eq. 3.1 can be expressed in terms of measures of stress and strain referred to a known configuration. Different descriptions of stress and strain can be used, but the strain energy of the body must be the same regardless of which description is used. So a necessary requirement to obtain the strain energy is the use of a stress and strain description energetically conjugate. Since Cauchy stresses are energetically conjugate to actual strains and 2nd Piola-Kirchoff stresses and Green-Lagrange strains are also energetically conjugate, the following expression is valid:

$$\int_{{}^tV} {}^t\tau_{ij}\, \delta_t e_{ij}\, {}^t dV = \int_{{}^0V} {}^t_0 s_{ij}\, \delta {}^t_0\varepsilon_{ij}\, {}^0 dV \tag{3.3}$$

where

${}^t_0 s_{ij}$ = 2nd Piola-Kirchoff stress tensor

${}^t_0\varepsilon_{ij}$ = Green-Lagrange strain tensor

${}^0V, {}^tV$ = Volume of the body at times 0 and t, respectively

On the right-hand side of Eq. 3.3, all terms are referred to the initial configuration. This is the key principle used in the development of the incremental Lagrangian equations of motion.

The 2nd Piola-Kirchoff stress tensor is defined as follows:

$${}^t_0 s_{ij} = \frac{{}^0\rho}{{}^t\rho}\, {}^0_t x_{i,m}\, {}^t\tau_{mn}\, {}^0_t x_{j,m} \tag{3.4}$$

where

${}^{0}\rho, {}^{t}\rho$ = Mass density at times 0 and t, respectively

${}^{t}_{0}x_{i,m}$ = Element (i,m) of the deformation gradient matrix (${}^{t}_{0}x_{i,m} = \frac{\partial {}^{t}x_{i}}{\partial {}^{0}x_{m}}$)

Reciprocally, the Cauchy stress tensor can be expressed as a function of the 2nd Piola-Kirchoff tensor as

$$ {}^{t}\tau_{ij} = \frac{{}^{t}\rho}{{}^{0}\rho} {}^{t}_{0}x_{i,m} {}^{t}_{0}s_{mn} {}^{t}_{0}x_{j,m} \tag{3.5} $$

Using the principle of conservation of mass, the following relation can be obtained:

$$ {}^{0}\rho = {}^{t}\rho \det {}^{t}_{0}X \tag{3.6} $$

where ${}^{t}_{0}X$ is the deformation gradient matrix.

The Green-Lagrange strain tensor is defined as

$$ {}^{t}_{0}\varepsilon_{ij} = \frac{1}{2}\left({}^{t}_{0}u_{i,j} + {}^{t}_{0}u_{j,i} + {}^{t}_{0}u_{k,i} {}^{t}_{0}u_{k,j} \right) \tag{3.7} $$

or

$$ {}^{t}_{0}\varepsilon_{ij} = {}^{t}_{0}e_{i,j} + {}^{t}_{0}\eta_{i,j} \tag{3.8} $$

where

$$ {}^{t}_{0}e_{ij} = \frac{1}{2}\left({}^{t}_{0}u_{i,j} + {}^{t}_{0}u_{j,i} \right) $$

$$ {}^{t}_{0}\eta_{ij} = \frac{1}{2}\left({}^{t}_{0}u_{k,i} {}^{t}_{0}u_{k,j} \right) $$

By means of Eq. 3.3, the incremental Lagrangian equation of motion can be obtained, referring stresses and strains to the initial configuration at time 0. In principle, any position of equilibrium can be used to refer stresses and strains. Basically there are two approaches: the total Lagrangian formulation in which all quantities are referred to the configuration at the initial time 0; and the updated Lagrangian formulation where all quantities are refered to the configuration at the beginning of a load step, in other words, at a determined time t. Using Eqs. 3.1 and 3.2, the equilibrium equation can be expressed for the total Lagrangian formulation as

$$\int_{{}^{t}V} {}^{t+\Delta t}_{0}S_{ij}\ \delta\,{}^{t+\Delta t}_{0}\varepsilon_{ij}\ {}^{0}dV = {}^{t+\Delta t}\Re \tag{3.9}$$

and for the updated Lagrangian formulation as

$$\int_{{}^{t}V} {}^{t+\Delta t}_{t}S_{ij}\ \delta\,{}^{t+\Delta t}_{t}\varepsilon_{ij}\ {}^{t}dV = {}^{t+\Delta t}\Re \tag{3.10}$$

Both formulations give the same result if the appropriate constitutive tensor is used in each case. The selection of one or the other formulation depends on its numerical efficiency. There is no well established criterion regarding which is the most efficient formulation. In this work, the updated Lagrangian formulation is used because the expressions are simpler than the ones in the total Lagrangian. This is a consequence of the initial displacement terms that appear in the total Lagrangian formulation.

The following definitions are used to obtain the incremental equations of equilibrium that enable one to determine the displacements at time t+Δt if the equilibrium configuration at time t is known:

$$\begin{aligned} {}^{t+\Delta t}_{t}S_{ij} &= {}^{t}_{t}S_{ij} + {}_{t}S_{ij} \\ {}^{t}_{t}S_{ij} &= {}^{t}\tau_{ij} \\ {}_{t}S_{ij} &= {}_{t}C_{ijrs}\,{}_{t}\varepsilon_{rs} \end{aligned}$$

where ${}_{t}C_{ijrs}$ is the strain-stress relation or elasticity tensor. This is often called the generalized Hooke's law. Therefore

$${}^{t+\Delta t}_{t}S_{ij} = {}^{t}\tau_{ij} + {}_{t}S_{ij} \tag{3.11}$$

The strain tensor is defined as

$${}^{t+\Delta t}_{t}\varepsilon_{ij} = {}_{t}\varepsilon_{ij}$$

where

$${}_{t}\varepsilon_{ij} = {}_{t}e_{ij} + {}_{t}\eta_{ij} \tag{3.12}$$

Substituting Eqs. 3.11 and 3.12 in Eq. 3.10, one obtains the equilibrium equation

$$\int_{{}^tV} {}_t s_{ij}\delta_t\varepsilon_{ij}\ {}^t dV + \int_{{}^tV} {}^t\tau_{ij}\ \delta_t\eta_{ij}\ {}^t dV = {}^{t+\Delta t}\Re - \int_{{}^tV} {}^t\tau_{ij}\ \delta_t e_{ij}\ {}^t dV \qquad (3.13)$$

Using the linearizing approximation

$${}_t s_{ij} = {}_t C_{ijrs}\, {}_t e_{rs}$$

$$\delta_t\varepsilon_{ij} = \delta_t\varepsilon_{ij}$$

the linearized equation of equilibrium is obtained:

$$\int_{{}^tV} {}_t C_{ijrs}\, {}_t e_{rs}\ \delta_t e_{ij}\ {}^t dV + \int_{{}^tV} {}^t\tau_{ij}\ \delta_t\eta_{ij}\ {}^t dV = {}^{t+\Delta t}\Re - \int_{{}^tV} {}^t\tau_{ij}\ \delta_t e_{ij}\ {}^t dV \qquad (3.14)$$

The right-hand-side of Eq. 3.14 gives the virtual work done by the external loads minus the virtual work done by the internal forces in the body at time t. The left-hand-side gives the virtual work done by the internal forces during the time Δt. If the geometry is updated including the new displacements computed from Eq. 3.14, equilibrium is not achieved due to the approximations made. An iterative procedure can reduce the unbalanced virtual energy. The following expressions correspond to a modified Newton iteration method:

$$\int_{{}^tV} {}_t C_{ijrs}\Delta_t e_{rs}^{(k)}\ \delta_t e_{ij}\ {}^t dV + \int_{{}^tV} {}^t\tau_{ij}\ \delta\Delta_t\eta_{ij}^{(k)}\ {}^t dV = {}^{t+\Delta t}\Re - \int_{{}^{t+\Delta t}V^{(k-1)}} {}^t\tau_{ij}^{(k-1)}\ \delta_{t+\Delta t} e_{ij}^{(k-1)}\ {}^{t+\Delta t} dV \qquad (3.15)$$

where the superscripts in parentheses indicate the iteration number and $\Delta_t e_{rs}^{(k)}, \Delta_t\eta_{ij}^{(k)}$ are the increments in the linear and nonlinear terms of the strain tensor.

3.3 Isoparametric Finite Element Discretization

In this section the governing finite element equations are developed from the general continuum mechanics equations presented in the previous section.

The basic assumption is the approximation of displacements and coordinates at any point of the element using appropriate interpolation functions. The displacements are expressed as follows:

$$u_i = \sum_{k=11}^{n} N_k u_i^k \tag{3.16}$$

and the coordinates

$$x_i = \sum_{k=1}^{n} N_k x_i^k \tag{3.17}$$

where

u_i = displacement of a generic point of the body in the i direction

u_i^k = displacement of node k in the i direction

x_i = i coordinate of a generic point of the body

x_i^k = i coordinate of node k

N_k = interpolation function correponding to node k

For isoparametric elements, the interpolation functions are the same for displacements and coordinates. The second step is to use Eqs. 3.16 and 3.17 to transform the strain-displacement relations of continuum mechanics into the matrix equation

$$\{\varepsilon\} = [B]\{u\} \tag{3.18}$$

where

$\{\varepsilon\}$ = strain vector

[B] = the transformation matrix

{u}= the displacement vector.

Finally , a constitutive law must be defined. Hooke's law is used in this study, and has the form

$$\{\sigma\} = [C]\{\varepsilon\} \tag{3.19}$$

Substituting Eqs. 3.14, 3.15, 3.16, and 3.17 into Eq. 3.15, the finite element model is

obtained in matrix form:

$$\left({}^{t}_{t}K_{L} + {}^{t}_{t}K_{NL}\right)\Delta U^{(i)} = {}^{t+\Delta t}R - {}^{t+\Delta t}_{t+\Delta t}F^{(i-1)} \tag{3.20}$$

where

${}^{t}_{t}K_{L}$ = linear stiffness matrix

${}^{t}_{t}K_{NL}$ = nonlinear stiffness matrix

${}^{t+\Delta t}R$ = vector of externally applied loads at time $t+\Delta t$

${}^{t+\Delta t}_{t+\Delta t}F^{(i-1)}$ = vector of nodal forces equivalent to the elements stresses at time $t+\Delta t$ for iteration (i-1)

$\Delta U^{(i)}$ = vector of increments in nodal displacements in iteration i

The following equations define the matrices K_L and K_{NL} and the corresponding terms in Eq. 3.15:

$$\int_{{}^{t}V} {}^{t}C_{ijrs}\, {}^{t}e_{rs}\, {}^{t}\delta e_{rs}\, {}^{t}dV \quad \Leftrightarrow \quad {}^{t}_{t}K_{L} = \int_{{}^{t}V} {}^{t}_{t}B_{L}^{T}\, {}^{t}_{t}C\, {}^{t}_{t}B_{L}\, {}^{t}dV$$

$$\int_{{}^{t}V} {}^{t}\tau_{ij}\, {}^{t}\delta\eta_{ij}\, {}^{t}dV \quad \Leftrightarrow \quad {}^{t}_{t}K_{NL} = \int_{{}^{t}V} {}^{t}_{t}B_{NL}^{T}\, {}^{t}\tau\, {}^{t}_{t}B_{NL}\, {}^{t}dV \tag{3.21}$$

$$\int_{{}^{t}V} {}^{t}\tau_{ij}\, {}^{t}\delta e_{ij}\, {}^{t}dV \quad \Leftrightarrow \quad {}^{t}_{t}F = \int_{{}^{t}V} {}^{t}_{t}B_{NL}^{T}\, {}^{t}\hat{\tau}\, {}^{t}dV$$

where ${}^{t}\hat{\tau}$ is the Cauchy stress vector, which will be defined for each element in the following sections.

3.4 Solution Technique for Nonlinear Finite Element Analysis

The nonlinear Eq. 3.20 is solved using the modified Newton-Raphson method. The procedure is illustrated in Fig. 3.2 for a one-degree-of-freedom system. The stiffness or slope of the force-displacement curve is updated only at the beginning of each load step. In the original Newton-Raphson method, the stiffness matrix is updated at each iteration. This speeds up covergence but can result in loss of computer efficiency.

The modified Newton-Raphson method, which is simple and generally converges in a

few iterations, is explained briefly in the following paragraphs. Let

$$^{t+\Delta t}f^{(i-1)} = {}^{t+\Delta t}R - {}^{t+\Delta t}F^{(i-1)} \tag{3.22}$$

Thus,

$$\left({}^{t}_{t}K_{L} + {}^{t}_{t}K_{NL}\right)\Delta U^{(i)} = {}^{t+\Delta t}f^{(i-1)} \tag{3.23}$$

The solution of Eq. 3.23, $\Delta U^{(i)}$, is used to obtain an improved prediction of the equilibrium configuration:

$$^{t+\Delta t}U^{(i)} = {}^{t+\Delta t}U^{(i-1)} + \Delta U^{(i)}$$

A new unbalanced force, $^{t+\Delta t}f^{(i)}$, and a new increment of displacement, $\Delta U^{(i+1)}$ are obtained for the next iteration. The iterative procedure continues until the unbalanced force, $^{t+\Delta t}f^{(i)}$, is smaller than a predetermined tolerance.

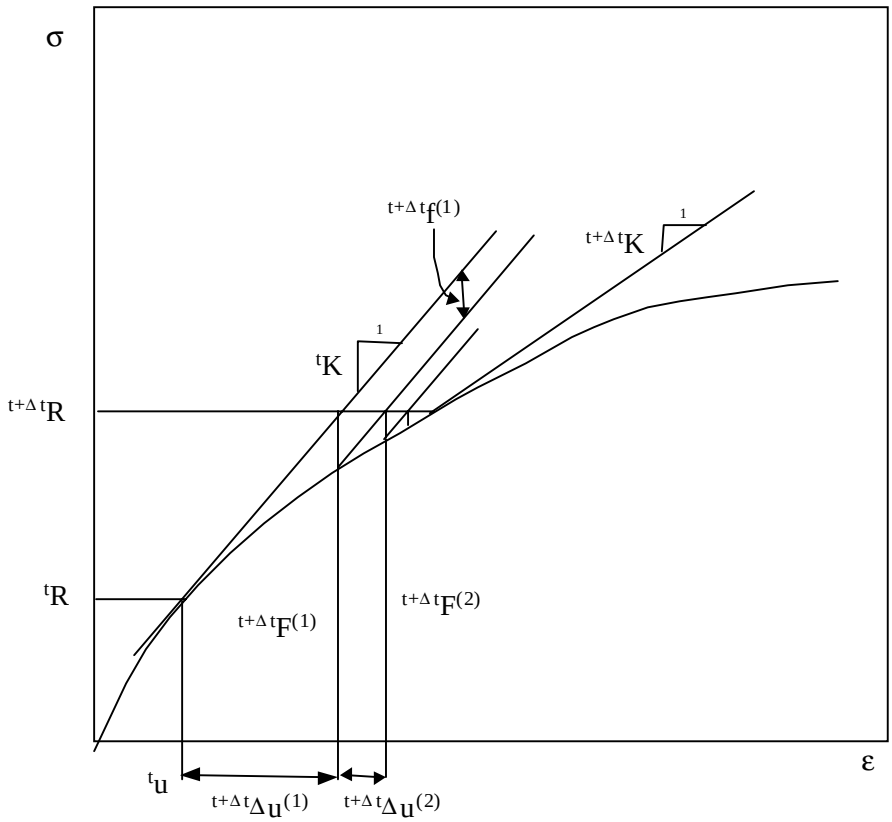

Figure 3.2 Modified Newton-Raphson method.

Chapter 4

Two-Dimensional Adhesive Finite Element

4.1 Introduction

Many successful analytical approaches have been formulated to compute stresses and displacements in two-dimensional specimens. All of them have limitations when arbitrary geometries are considered. Finite element methods give results for any geometry but at a high cost of computational and human resources. This chapter presents an extension of the 2-D finite element model of adhesives developed by Taylor (1996). The new version of the adhesive finite element model includes geometric nonlinearities in the adherends and in the adhesive layer.

4.2 Formulation

The adherends are modeled as Bernoulli/Euler beam elements with axial and bending deformation modes. The adhesive is a standard plane-strain quadrilateral element except that the nodes are offset to coincide with the midplane of the corresponding adherend. The beams and special adhesive elements, called ADH2D, are shown in Fig. 4.1. The formulation is similar to that of Carpenter and Barsoum (1989), except that the interpolation functions for the adhesive element were chosen to be compatible with the deformations of the beam-truss elements. These compatible elements were shown to converge to known closed form solutions much more rapidly than the incompatible elements (Taylor, 1996).

In the next section, the two components of the adhesive joint, the adherends and the adhesive, are formulated.

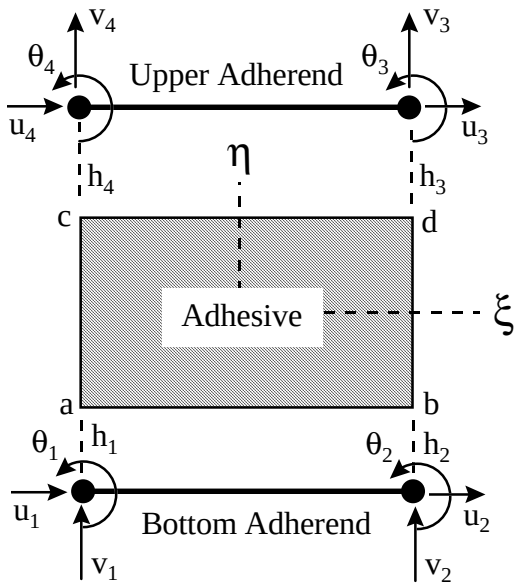

Figure 4.1 Two-dimensional adhesive finite element

4.2.1 Adherends

Large-displacement Bernoulli-Euler beam elements model the adherends. The formulation of this element can be found in the literature (Reddy, 1992). A summary of that formulation is presented in this section. The primary variables are:

$$u, \quad v, \quad \frac{dv}{dx}$$

where u and v are axial and transverse displacements, respectively. These variables are approximated by the following interpolation functions:

$$u = \sum_{i}^{2} \psi_i u_i , \quad v = \sum_{i}^{4} \phi_i s_i \tag{4.1}$$

where:

u_i , s_i = nodal displacements (Fig. 4.2)

ψ_i = linear Lagrange interpolation functions

ϕ_i = cubic Hermite interpolation functions

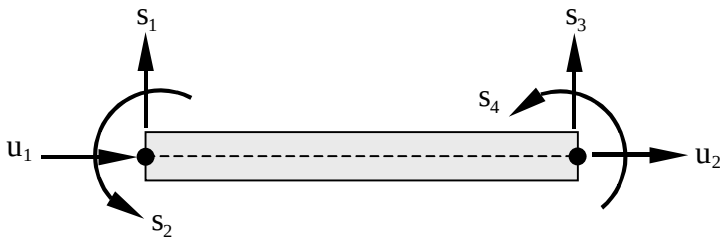

Figure 4.2 Nonlinear beam, generalized displacements.

Substituting Eqs. 4.1 into the virtual work expression, one obtains the finite element model of the adherends as

$$[K(\{\Delta\})]\{\Delta\} = \{F\} \tag{4.2}$$

where

$\{\Delta\}$ = nodal displacement vector, $\{u_1, u_2, s_1, s_2, s_3, s_4\}$

$K(\{\Delta\})$ = stiffness matrix

$\{F\}$ = nodal load vector, $\left\{F_1^1, F_2^1, F_1^2, F_2^2, F_3^2, F_4^2\right\}$

The equilibrium equation (4.2) can be expanded:

$$\begin{bmatrix} [K^{11}] & [K^{12}] \\ [K^{21}] & [K^{22}] \end{bmatrix} \begin{Bmatrix} \{u\} \\ \{v\} \end{Bmatrix} = \begin{Bmatrix} \{F^1\} \\ \{F^2\} \end{Bmatrix} \tag{4.3}$$

where

$$K_{ij}^{11} = \int_0^L \frac{EA}{L} \frac{d\psi_i}{dx} \frac{d\psi_j}{dx} dx$$

$$K_{ij}^{12} = \int_0^L \frac{EA}{2L} \frac{dw}{dx} \frac{d\psi_i}{dx} \frac{d\phi_j}{dx} dx$$

$$K_{ij}^{21} = \int_0^L \frac{EA}{L} \frac{dw}{dx} \frac{d\phi_i}{dx} \frac{d\psi_j}{dx} dx$$

$$K_{ij}^{22} = \int_0^L \frac{EI}{L} \frac{d^2\phi_i}{dx^2} \frac{d^2\phi_j}{dx^2} dx + \int_0^L \frac{EA}{2L} \left(\frac{dw}{dx}\right)^2 \frac{d\phi_i}{dx} \frac{d\phi_j}{dx} dx$$

E = Young's modulus

A = Cross-sectional area

I = Moment of inertia of cross-section

L = Length of the element

F^1 , F^2 = Applied loads (Fig. 4.3)

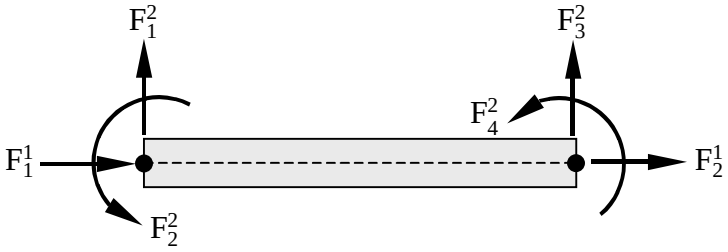

Figure 4.3 Nonlinear beam, generalized displacements.

4.2.2 Adhesive

The adhesive layer is represented by a plane-stress/strain solid element with offset nodes. In order to make the displacements in the adhesive-adherend interfaces compatible, special interpolations functions are used.

In the finite element discretization, coordinates of any point in the adhesive can be expressed as a function of the nodal coordinates of the element:

$$\{x\} = \sum [N_i] \{x_i\}$$

where

$\{x\}=\{x,y\}$ = coordinates of a generic point in the adhesive

$\{x_i\}= \{x_i,y_i\}$ = nodal coordinates

$[N_i]$= linear interpolation functions of local coordinates ξ and η

The displacements in the adhesive element are also represented by interpolation polynomial functions:

$$\{u_{adhes}\} = [N_i]_{adhes} \{u_i\}_{adhes}$$

where

$$\{u_{adhes}\} = \begin{Bmatrix} u \\ v \end{Bmatrix}_{adhes}$$

$$\{u_i\}_{adhes} = \{u_1 \quad v_1 \quad u_2 \quad v_2 \quad u_3 \quad v_3 \quad u_4 \quad v_4\}_{adhes}$$

$[N_i]_{adhes}$ = interpolation functions in the adhesive layer

The objective is to obtain the interpolation functions for the adhesive element; the final expressions can be found in Taylor (1996). A brief summary follows.

The $[N_i]_{adhes}$ are obtained by imposing equal displacement of the adhesive and the adherends in both interfaces ab and cd (see Fig 4.1). The displacements of the bottom adherend are

$$\{u_{adher}\}_b = [N_i]_{adher}\{u_i\}_{adher_b}$$

where

$$\{u_{adher}\}_b = \begin{Bmatrix} u \\ v \end{Bmatrix}_{adher_b}$$

$$\{u_i\}_{adher_b} = \{u_1 \quad v_1 \quad \theta_1 \quad u_2 \quad v_2 \quad \theta_2\}$$

$$[N_i]_{adher} = \begin{bmatrix} N_1' & 0 & -h_1 N_1'' & N_2' & 0 & -h_2 N_2'' \\ 0 & N_1''' & N_1''' & 0 & N_2''' & N_2''' \end{bmatrix}_{adher}$$

$N_i', N_i'', \text{and } N_i'''$ = linear, quadratic, and cubic interpolation functions

h_i = distance from the neutral axis of the adherend

Similar expressions can be obtained for the displacements in the upper adherend. In the adherend-adhesive interfaces, ab and cd (Fig 4.1), the following equations must be satisfied:

$$\{u_{adhes}\}_{ab} = \sum_i^4 [N_{i\,ab}]_{adhes}\{u_i\}_{adhes} = \{u_{adher}\}_b = \sum_i^2 [N_{i\,top}]_{adher}\{u_i\}_{adher_b} \qquad (4.4)$$

$$\{u_{adhes}\}_{cd} = \sum_{i}^{4} [N_{i\,cd}]_{adhes} \{u_i\}_{adhes} = \{u_{adher}\}_{u} = \sum_{i}^{2} [N_{i\,bottom}]_{adher} \{u_i\}_{adher_u} \qquad (4.5)$$

where

$[N_{i\,ab}]_{adhes}$ and $[N_{i\,cd}]_{adhes}$ = are the interpolation functions for the adhesive evaluated at the ab and cd interfaces, respectively.

$[N_{i_{top}}]_{adher}$ and $[N_{i_{bottom}}]_{adher}$ = interpolation functions for the upper and bottom adherends evaluated at the cd and ab interfaces, respectively. These functions are known.

$\{u_{adhes}\}_{cd}$ and $\{u_{adhes}\}_{ab}$ = displacements of the adhesive at the cd and ab interfaces, respectively.

$\{u_{adher}\}_{b}$ and $\{u_{adher}\}_{u}$ = displacements of the bottom adherend at the ab interface and the upper adherend at the cd interface, respectively.

$[u_i]_{adhes}$ = nodal displacements of the adhesive.

$[u_i]_{adher_u}$ and $[u_i]_{adher_b}$ = nodal displacements of the upper and bottom adherends, respectively.

The vertical displacement, v, is defined as the product of a complete cubic polynomial in ξ and a complete linear polynomial in η. In the same way, the horizontal displacement, u, is defined as the product of a complete quadratic polynomial in ξ and a complete linear polynomial in η. By substituting the polynomial expressions of the vertical and horizontal displacements in Eqs. 4.5 and 4.6, cubic and parabolic interpolation functions are obtained for the vertical and horizontal displacement which make compatible displacements in the adhesive and adherend interface. So

$$u(\xi,\eta) = \sum_{i=1}^{N} h_i \delta_i$$
$$v(\xi,\eta) = \sum_{i=1}^{N} \psi_i \delta_i \qquad (4.6)$$

where

$$h_i(\xi,\eta) = \begin{Bmatrix} h_i^u \\ h_i^v \\ h_i^\theta \end{Bmatrix} = \text{interpolation functions for the horizontal displacements}$$

$$\psi_i(\xi,\eta) = \begin{Bmatrix} 0 \\ \psi_i^v \\ \psi_i^\theta \end{Bmatrix} = \text{interpolation functions for the vertical displacements}$$

δ_i = displacement vector of node i $\{u_i, v_i, \theta_i)$

With the displacements defined, the different components of Eq. 3.18 can be determined. The incremental strains are

$$\begin{aligned}
{}_t\varepsilon_{11} &= {}_t u_{1,1} + \frac{1}{2}\left(\left({}_t u_{1,1}\right)^2 + \left({}_t u_{2,1}\right)^2\right) \\
{}_t\varepsilon_{22} &= {}_t u_{2,2} + \frac{1}{2}\left(\left({}_t u_{1,2}\right)^2 + \left({}_t u_{2,2}\right)^2\right) \\
{}_t\varepsilon_{12} &= \frac{1}{2}\left(\left({}_t u_{1,2}\right)^2 + \left({}_t u_{2,1}\right)^2\right) + \frac{1}{2}\left({}_t u_{1,1}\,{}_t u_{1,2} + {}_t u_{2,1}\,{}_t u_{2,2}\right)
\end{aligned} \tag{4.7}$$

where

$$\left\{{}_t u\right\} = \begin{Bmatrix} {}_t u_1 \\ {}_t u_2 \end{Bmatrix} = \begin{Bmatrix} {}_t u \\ {}_t v \end{Bmatrix}$$

Since ${}_t e = {}_t^t B_L\, {}_t u$ and defining

$$u = \sum_{i=1}^{4} \phi_i \delta_i = \sum_{i=1}^{4} \begin{Bmatrix} h_i \\ \psi_i \end{Bmatrix} \delta_i, \tag{4.8}$$

and then, combining Eqs. 4.6, 4.7, and 4.8, the strain-displacement matrices are as follows:

$${}_t^t B_L = \begin{bmatrix}
{}_t h_{1,1}^u & {}_t h_{1,1}^v & {}_t h_{1,1}^\theta & {}_t h_{2,1}^u & {}_t h_{2,1}^v & {}_t h_{2,1}^\theta & \cdots \\
0 & {}_t \psi_{1,2}^v & {}_t \psi_{1,2}^\theta & 0 & {}_t \psi_{2,2}^v & {}_t \psi_{2,2}^\theta & \cdots \\
{}_t h_{1,2}^u & {}_t h_{1,2}^v + {}_t \psi_{1,1}^v & {}_t h_{1,2}^\theta + {}_t \psi_{1,1}^\theta & {}_t h_{2,2}^u & {}_t h_{2,2}^v + {}_t \psi_{2,1}^v & {}_t h_{2,2}^\theta + {}_t \psi_{2,1}^\theta & \cdots
\end{bmatrix}$$

$$\begin{bmatrix}
\cdots & {}_t h_{N,1}^u & {}_t h_{N,1}^v & {}_t h_{N,1}^\theta \\
\cdots & 0 & {}_t \psi_{N,1}^v & {}_t \psi_{N,1}^\theta \\
\cdots & {}_t h_{N,2}^u & {}_t h_{N,1}^v + {}_t \psi_{N,1}^v & {}_t h_{N,1}^\theta + {}_t \psi_{N,1}^\theta
\end{bmatrix} \tag{4.9}$$

and

$$ {}_t^t B_{NL} = \begin{bmatrix} {}_t h^u_{1,1} & {}_t h^v_{1,1} & {}_t h^\theta_{1,1} & {}_t h^u_{2,1} & {}_t h^v_{2,1} & {}_t h^\theta_{2,1} & \cdots & {}_t h^u_{N,1} & {}_t h^v_{N,1} & {}_t h^\theta_{N,1} \\ {}_t h^u_{1,2} & {}_t h^v_{1,2} & {}_t h^\theta_{1,2} & {}_t h^u_{2,2} & {}_t h^v_{2,2} & {}_t h^\theta_{2,2} & \cdots & {}_t h^u_{N,2} & {}_t h^v_{N,2} & {}_t h^\theta_{N,2} \\ 0 & {}_t \psi^v_{1,1} & {}_t \psi^\theta_{1,1} & 0 & {}_t \psi^v_{2,1} & {}_t \psi^\theta_{2,1} & \cdots & 0 & {}_t \psi^v_{N,1} & {}_t \psi^\theta_{N,1} \\ 0 & {}_t \psi^v_{1,2} & {}_t \psi^\theta_{1,2} & 0 & {}_t \psi^v_{2,2} & {}_t \psi^\theta_{2,2} & \cdots & 0 & {}_t \psi^v_{N,2} & {}_t \psi^\theta_{N,2} \end{bmatrix} \quad (4.10) $$

and the Cauchy stresses are

$$ {}^t\tau = \begin{bmatrix} {}^t\tau_{11} & {}^t\tau_{12} & & \\ {}^t\tau_{21} & {}^t\tau_{22} & & \\ & & {}^t\tau_{11} & {}^t\tau_{12} \\ & & {}^t\tau_{21} & {}^t\tau_{22} \end{bmatrix}; \quad {}^t\hat{\tau} = \begin{Bmatrix} {}^t\tau_{11} \\ {}^t\tau_{22} \\ {}^t\tau_{12} \end{Bmatrix} \quad (4.11) $$

where ${}^t\tau_{ij}$ is the stress tensor matrix and ${}^t\hat{\tau}$ is the Cauchy stress vector

The constitutive law for the adhesive is

$$ {}_t C_{ijrs} = D = \underbrace{\frac{E}{1-\nu^2}\begin{bmatrix} 1 & \nu & 0 \\ \nu & 1 & 0 \\ 0 & 0 & \frac{1-\nu}{2} \end{bmatrix}}_{\text{Plane Stress}} \quad \text{or} \quad D = \underbrace{\frac{E}{(1+\nu)(1-2\nu)}\begin{bmatrix} 1-\nu & \nu & 0 \\ \nu & 1-\nu & 0 \\ 0 & 0 & \frac{1-2\nu}{2} \end{bmatrix}}_{\text{Plane Strain}} \quad (4.12) $$

where E is the elastic modulus and ν the Poisson's ratio.

As was mentioned in chapter 3, all the incremental equations of motion are referred to the equilibrium configuration at time t. In other words, the updated Lagrangian formulation is used in this work.

4.2.3 Thermal and Moisture Effects

Thermal and moisture effects are taken into account by defining an initial strain $\varepsilon_{0,}$ which does not produce stress. Accordingly,

$$ \sigma = D(\varepsilon - \varepsilon_0) \quad (4.13) $$

and

$$\varepsilon_0 = \begin{Bmatrix} \alpha\Delta T + \beta\Delta M \\ \alpha\Delta T + \beta\Delta M \\ 0 \end{Bmatrix} \tag{4.14}$$

for plane stress and

$$\varepsilon_0 = (1+\nu)\begin{Bmatrix} \alpha\Delta T + \beta\Delta M \\ \alpha\Delta T + \beta\Delta M \\ 0 \end{Bmatrix} \tag{4.15}$$

for plane strain. α and β are the thermal and moisture coefficients, respectively, and ΔT and ΔM are the temperature and moisture variations relative to the initial values.

4.2.5 Single Lap Joint Example

A single lap joint (SLJ) shown in Fig. 4.4 was analyzed using the special adhesive finite element (ADH2D). This geometry is very popular in industrial applications as a benchmark test and the bibliography about this kind of joint is very extensive; there are many analytical solutions and test results. For this reason, this specimen was chosen to test the performance of the model.

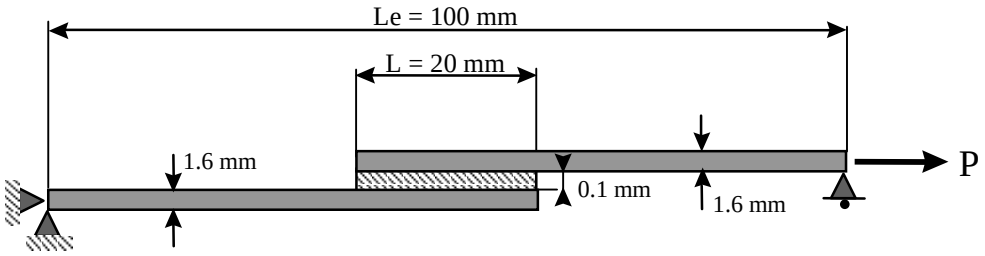

Figure 4.4 Single lap joint specimen.

The properties of the materials are given in Table 4.1.

Table 4.1. Mechanical properties of the materials of the single lap joint specimen.

	Adherend	Adhesive
E [GPa]	68.3	2.5
ν	0.3	0.3

The finite element model is shown in Figure 4.5.

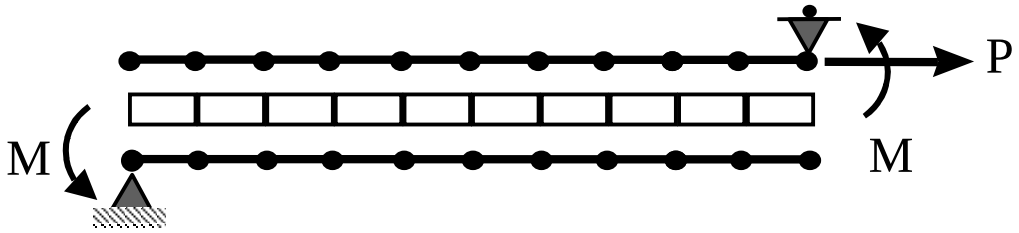

Figure 4.5 Finite element model of a single lap joint.

Peel and shear stresses were obtained performing a linear analysis with ADH2D elements. They were compared with those from a finite element analysis with ABAQUS, using 2-D plane-stress finite elements (Fig. 4.6 and 4.7). The ADH2D model and the ABAQUS analysis required 350 and 1200 degrees of freedom, respectively. It is noticeable that the ADH2D elements give almost the same answer with a remarkable reduction of the number of degrees of freedom. Therefore, smaller systems of equations than for ordinary finite elements, like the 2-D solid elements used in ABAQUS, can be used and consequently less computational effort is required.

In Taylor (1996), the performance of this element was compared with other models such as those of Carpenter and Barsoum (1989), Delale and Erdogan (1981), and Goland and Reissner (1944). In all cases the element showed accurate results for relatively coarse meshes. The maximum normal and peel stresses are within 1.5% of the analytical solution by Delale and Erdogan (1981).

Since only the overlap was modeled, see Fig 4.5, moments must be applied to account for the geometrically nonlinear effects acting on a single lap joint configuration. Those moments were obtained using Goland and Reissner's (1944) formulation.

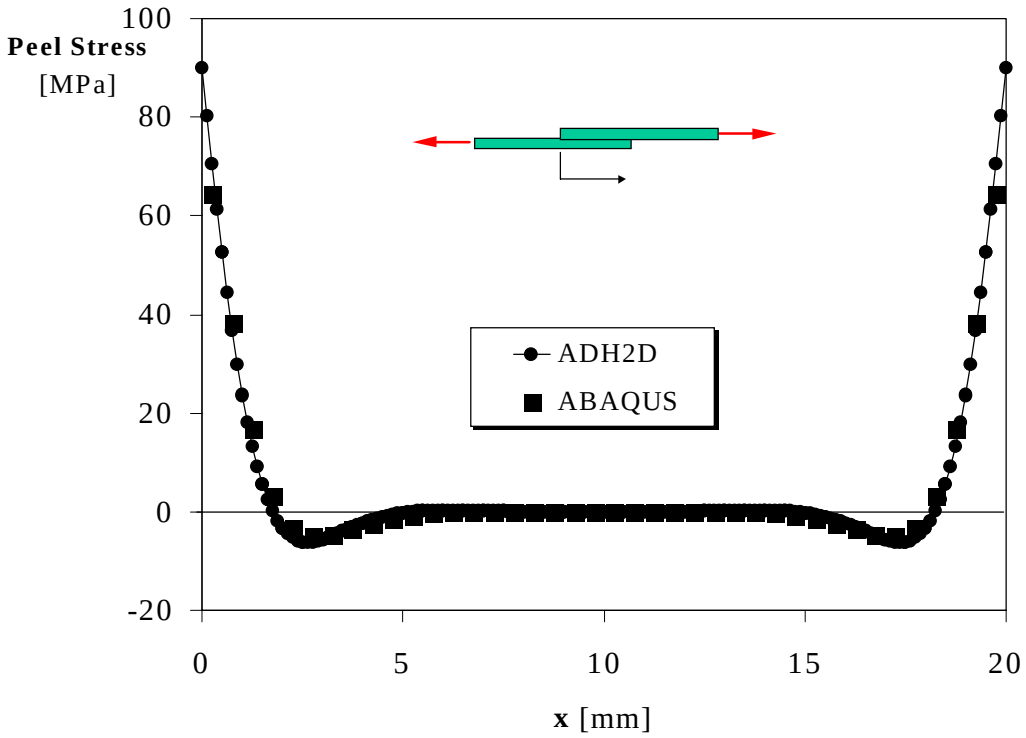

Figure 4.6. Peel stress distribution for a single lap joint.

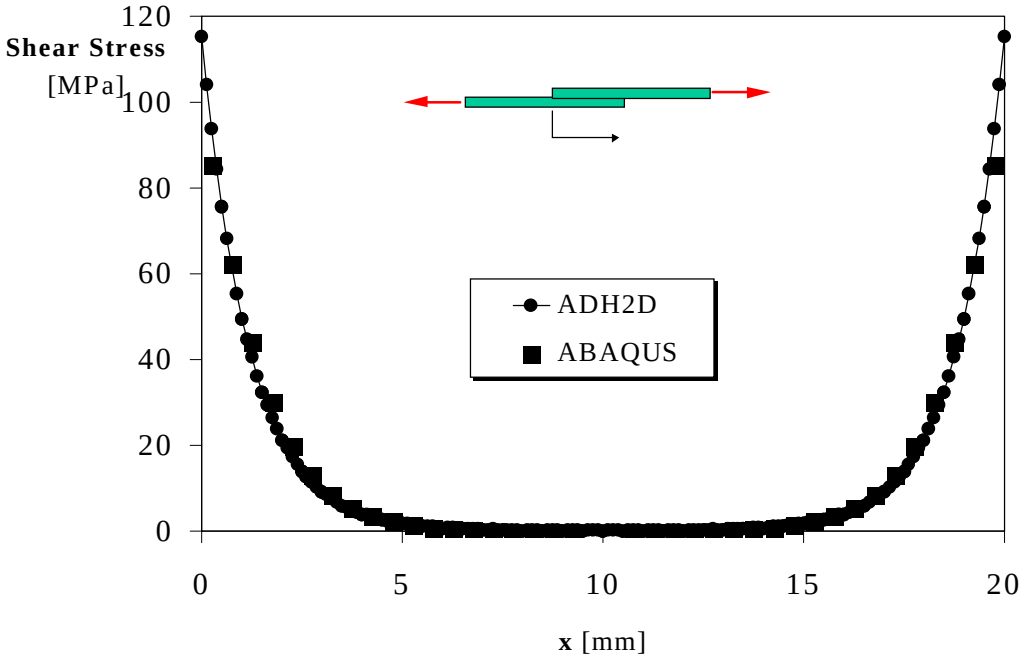

Figure 4.7 Shear stress distribution for a single lap joint.

The main contribution of the present work to Taylor's 2-D model is the inclusion of geometric nonlinearities in the finite element formulation. The same specimen depicted in Fig. 4.3 was analyzed with geometric nonlinearities included. Figs. 4.9 and 4.10 show the effect of this nonlinearity in the peel and shear stress distributions. The finite element model is shown in Fig. 4.8. This time the whole structure was modeled, so the moments at the beginning of the overlap are no longer required.

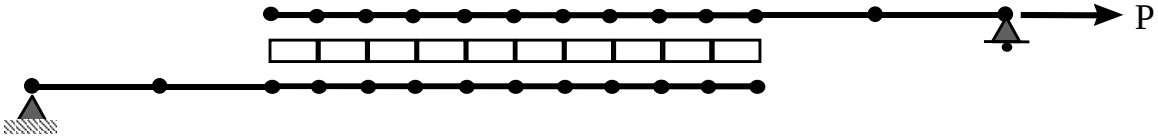

Figure 4.8 Finite element model of a simple lap joint for a Geometrically Nonlinear Analysis.

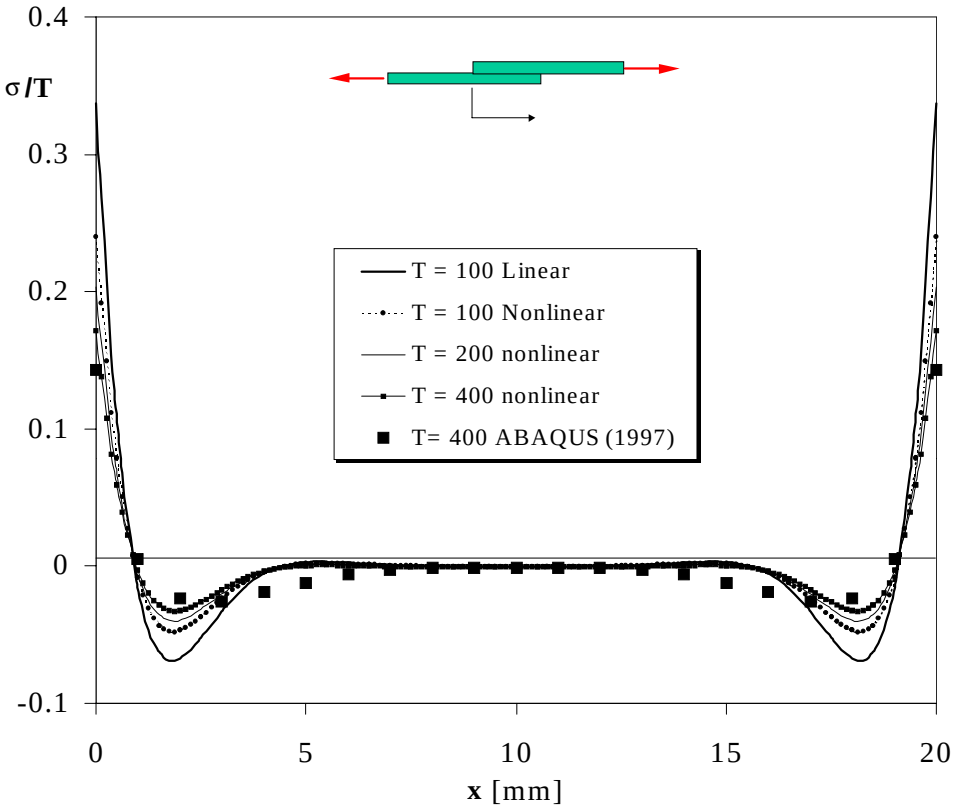

Figure 4.9. Peel stress distribution for a single lap joint. Geometric nonlinearity is included. Dimensions of T are N/mm^2.

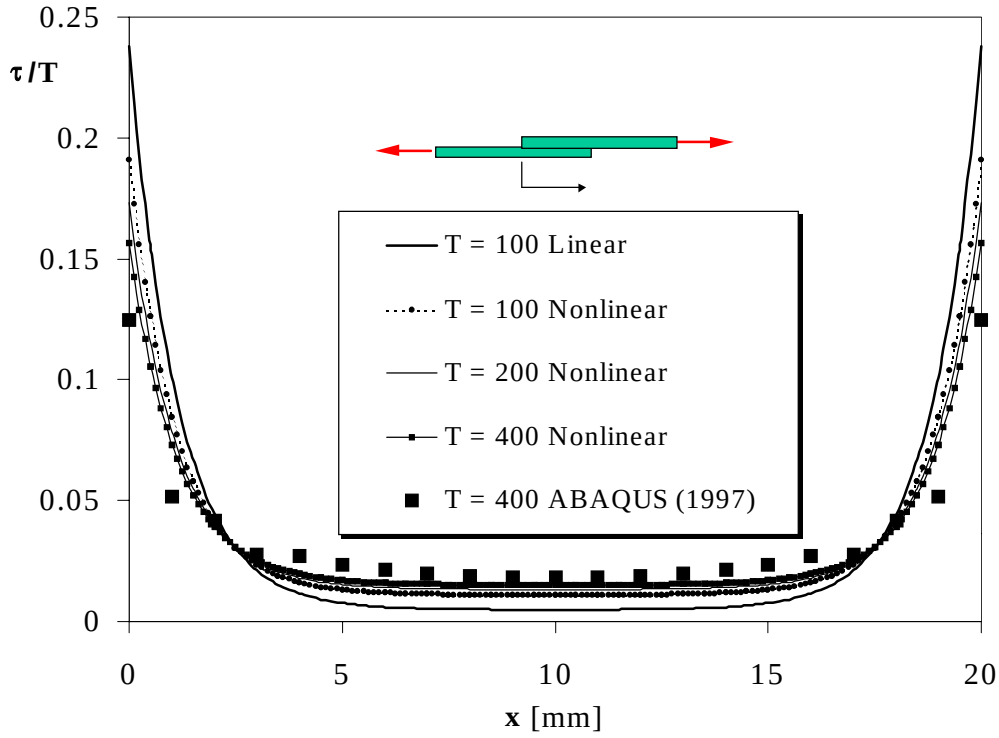

Figure 4.10. Shear stress distribution for a single lap joint. Geometric nonlinearity included. Dimensions of T are N/mm^2.

The specimen was subjected to different levels of load. T is the total load divided by the thickness and the width of the adherends. Figs. 4.9 and 4.10 show that stress concentrations at the overlap ends for peel and shear stress distributions decrease as the load increases. This is the result of the reduction of the moment arm of the two eccentric loads as their magnitude increases.

There is a physical limit for that reduction of the moment arm, which is when the two loads are collinear. Therefore, it is reasonable to expect that the change in the stress concentration between two load levels becomes less important as the load increases.

4.3 Fracture Mechanics Analysis

Several approaches for determining strain energy release rates in finite element analysis have been proposed. One commonly used approach is the crack closure method, introduced by Rybicki and Kanninen (1977), in which the components of the energy release rate are determined as follows:

$$G_I = \lim_{\Delta a \to 0} \frac{1}{2\Delta a} F_c \left(v_c - v_d \right) \tag{4.16}$$

$$G_{II} = \lim_{\Delta a \to 0} \frac{1}{2\Delta a} T_c \left(u_c - u_d \right) \tag{4.17}$$

where Δa represents the length of crack closed by the normal forces, F_c and F_d, and tangential forces, T_c and T_d; $(v_c\text{-}v_d)$ and $(u_c\text{-}u_d)$ represent the normal and tangential separation of the nodes before they are closed (Fig. 3.11). This approach has been used in this study along with a standard compliance approach for comparison purposes of the linear models.

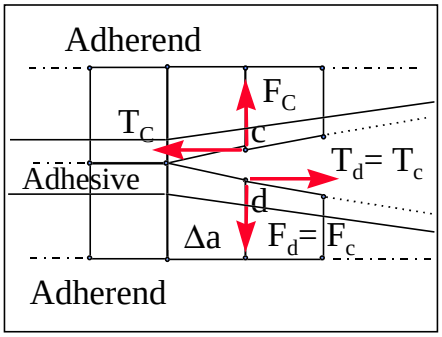

Figure 4.11. Modified Crack Closure Integral Method.

Preliminary results have been obtained for analyzing simple adhesive bond test geometries using 2-D elements. The double cantilever beam specimen (DCB) is widely used in fracture and fatigue testing of adhesive bonds. The analytical solution for a symmetrically loaded DCB is given by

$$G_I = \frac{4P^2\left(3a^2 + h^2\right)}{Eb^2h^3} \tag{4.18}$$

where P is the applied force, a is the debond length, h is the thickness of the adherends, E is Young's modulus for the adherend, and b is the adherend (and bond) width. This solution neglects the flexibility of the adhesive layer.

The specimen shown in Fig. 4.12 was modeled using 2-D plane-strain elements from ABAQUS (1997) and the ADH2D special adhesive. The specimen width and adhesive thickness were 25.4 mm and 0.13 mm, respectively. Young's moduli and Poisson's ratios were 72.45 GPa and 0.33 for the adherends and 1.932 GPa and 0.4 for the adhesive.

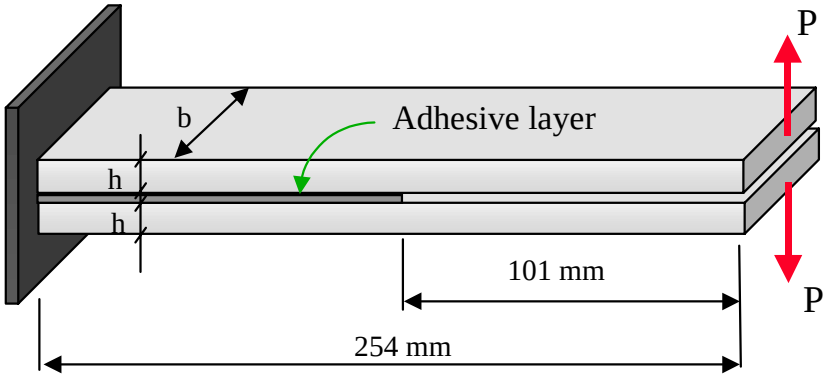

Figure 4.12. Double Cantilever Beam (DCB) Specimen.

Values of energy release rates from both finite element models were obtained by applying Eqs. 4.16 and 4.17 and also by a standard compliance derivative. Since geometric nonlinearities are not relevant for DCB specimens with small deflections, only linear cases were studied. Table 3.2 summarizes the results obtained, showing differences about 5% among the different approaches.

Table 4.2. Energy Release Rates for a Double Cantilever Beam.

Method	Energy Release Rate [J/m^2]
2-D Solid Elements (ABAQUS)	109.4
ADH2D Crack Closure	104.0
ADH2D Compliance Derivative	103.9
Analytical Expression	103.9

A second example considered is the cracked lap shear (CLS) geometry shown in Fig. 4.13.

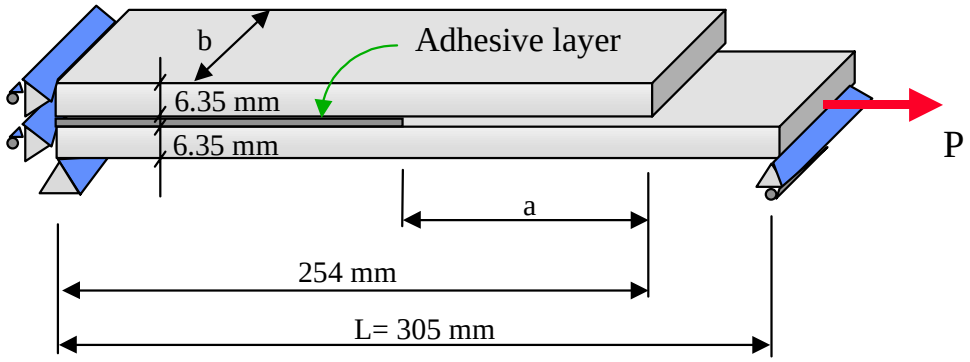

Figure 4.13. Crack Lap Shear (CLS) Specimen.

As in the DCB specimen, the adhesive thickness was 0.13 mm and the width for both adhesive and adherends was 25.4 mm. The material properties used were 72.45 GPa and 1.932 GPa for the Young's moduli, and 0.33 and 0.4 for the Poisson's ratios of adherend and adhesive, respectively. This configuration is the same as the one appearing in Johnson's round-robin study (1987) as the proposed equal thickness adherend specimen.

In order to determine whether geometric nonlinearities are important for this specimen, several runs with different loads were made. The results in Fig 4.14 show a definite deviation from the linear case as the load increases. Therefore, the problem was analyzed using both linear and nonlinear models.

Using the same specimen with a load of 11.120 kN, values of energy release rates were obtained from ordinary 2-D elements (ABAQUS) and from ADH2D elements applying the crack closure method in both cases. The 2-D solid element mesh is composed of 3270 nodes and 1014 elements, while the ADH2D mesh has only 207 nodes and 117 elements. Another value of energy release rate was obtained using singular elements to model the crack tip and the J-Integral option from ABAQUS. Table 4.3 summarizes the results obtained; once again good agreement was found.

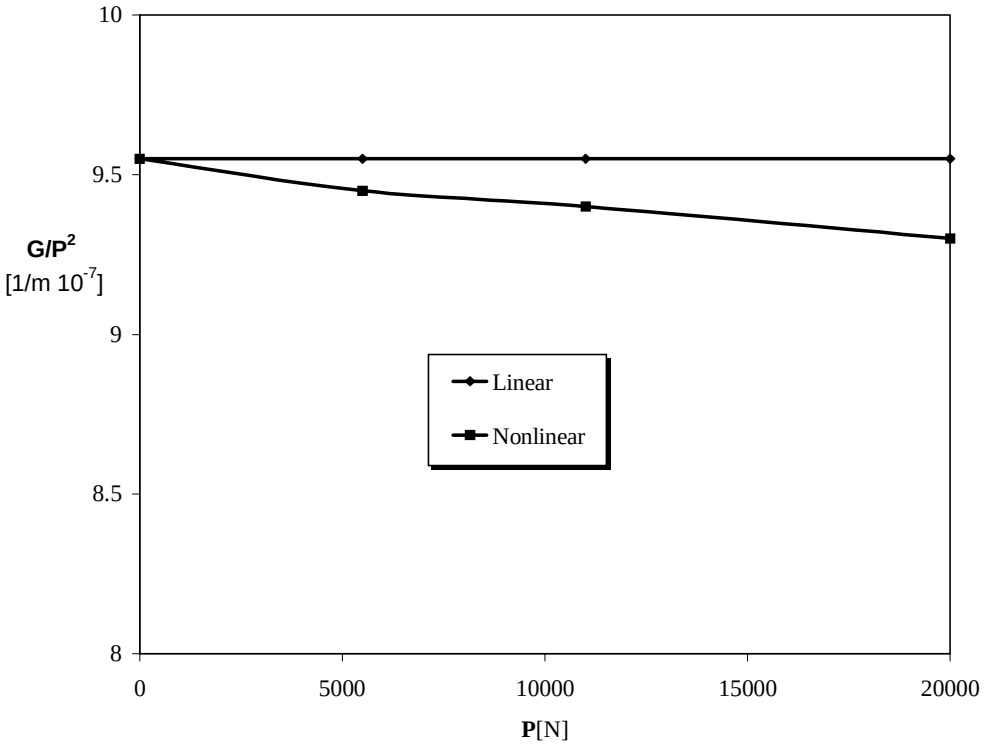

Figure 4.14. Strain energy release rate vs. applied load.

Johnson (1987) has summarized the results from a number of individuals who participated in an ASTM round-robin study of the CLS specimen. A number of approaches were used, and considerable variation in the results was found. Figs. 4.15 and 3.16 show the total energy release rate and the mode mix ratio, including ADH2D results. There is good agreement between the ADH2D element results and those reported in the round-robin study.

Table 4.3. Energy release rates for a crack lap shear.

Method	Energy Release Rate, $[J/m^2]$
2-D Solid Elements (ABAQUS) Crack Closure	120.9
2-D Solid Elements (ABAQUS) Singular Elements	119.9
ADH2D Crack Closure	118.1
Analytical Expression (Brussat and Chiu 1978)	103.9

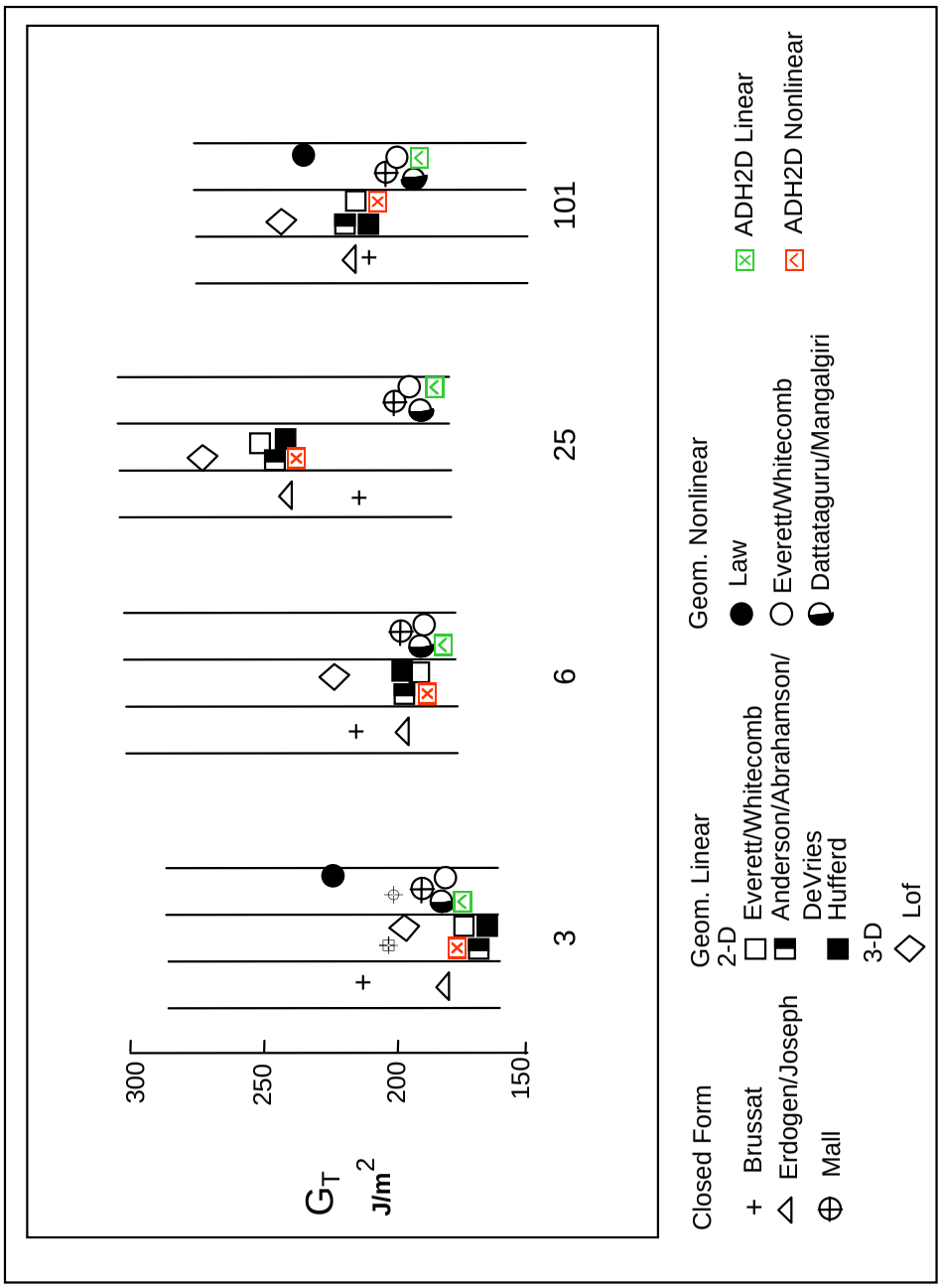

Figure 4.15. Total strain energy release rate results of ASTM round-robin crack lap shear specimen including new results from ADH2D approach.

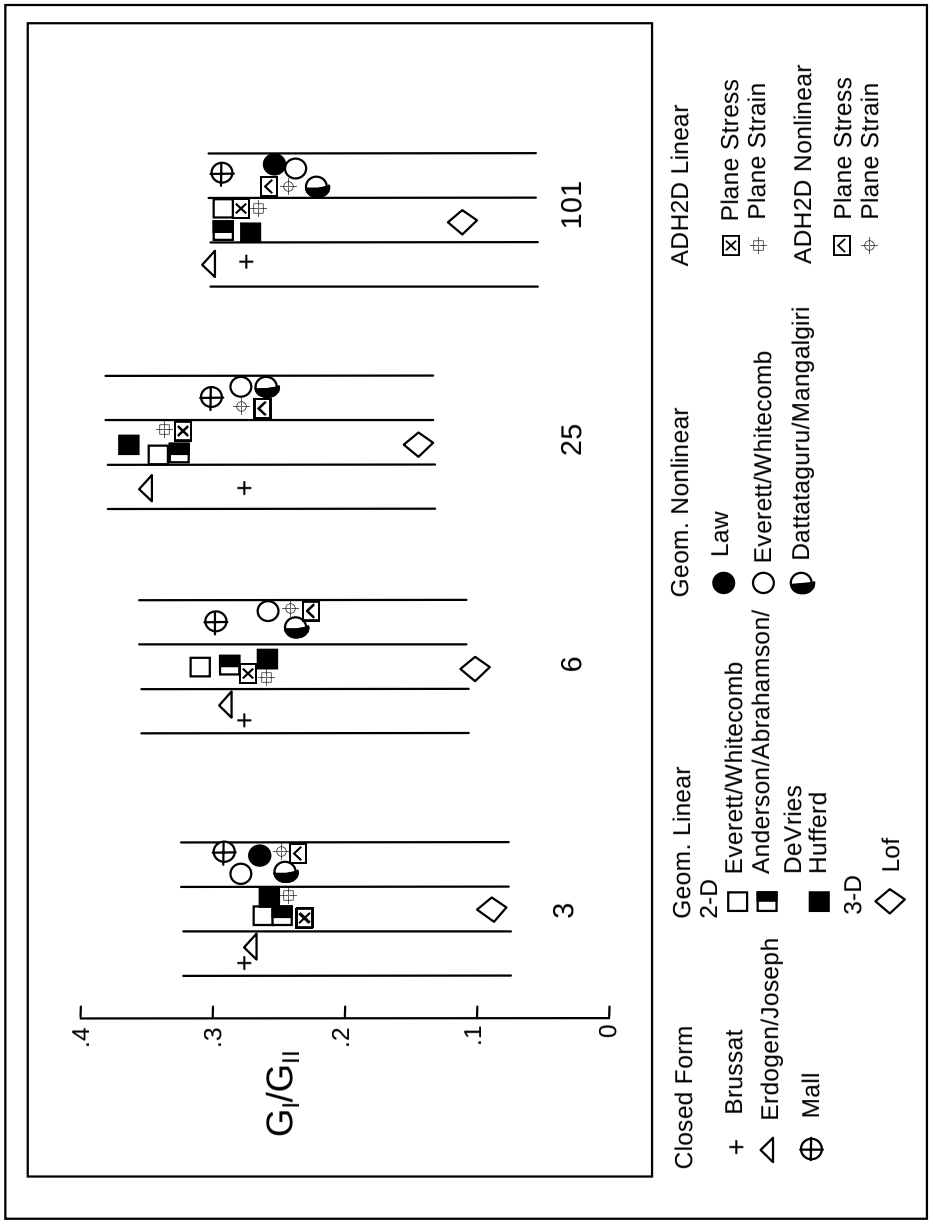

Figure 4.16. Mode mix results of ASTM round-robin crack lap shear specimen including new results from ADH2D approach.

In the Johnson round-robin study (1987), all of the 2-D finite element analyses used plane-strain elements. The 3-D finite element analysis by Lof (Johnson, 1987)did not require such assumption. The more compliant specimen resulted in higher energy release rates than any of the other linear FEA. In the analytical solution by Brussat et al. (1977), E rather than $E/(1-\mu^2)$ was apparently used, corresponding to an assumption of plane-stress.

Fig. 4.17 shows values of energy release rates vs. debond length for the round-robin paper specimen. These values were obtained with the ADH2D finite element model using both linear and geometric nonlinear analyses, the Brussat et al. (1977) expression, and the Lai and Dillard (1995) analytical expression. The agreement among these solutions is remarkable. Also, Fig. 4.17 shows the importance of using geometrically nonlinear elements in order to obtain accurate results for the CLS specimen.

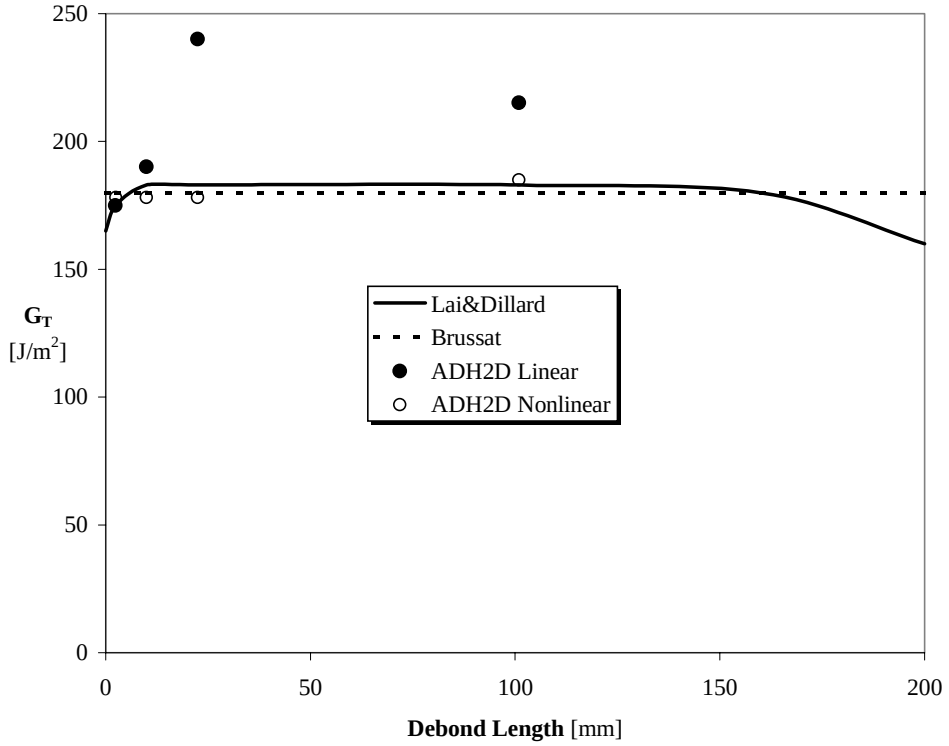

Figure 4.17. Comparison between different analyses of strain energy release rate values *vs* debond length for the equal adherend thickness CLS specimen of the round-robin study (Johnson 1987).

4.4 Conclusions

Simple 2-D finite element for obtaining “strength of materials” level solutions for stresses in bonded joints was developed. Although the simple elements are not capable of capturing the singular stress fields which occur at bimaterial interfaces or debond tips, the magnitudes of the non-singular stresses are believed to be useful for many design and analysis purposes. The simple models of this approach require minimal computational time as well as minimal pre- and post-processing time from the stress analyst. Even complicated bonded structures made of thin-walled components can easily be modeled with these elements.

The technique seems to be applicable to evaluate the fracture parameters of bonded geometries. Using ADH2D elements, values of strain energy release rate and mode mix were found to be in good agreement with analytical solutions and finite element analyses using conventional elements for both the DCB and CLS geometries.

Chapter 5

Three-Dimensional Adhesive Finite Element

5.1 Introduction

The formulation of the proposed 3-D finite element is an extension of the adhesive element developed by Taylor (1996). As in that work, the model of the adhesively bonded joint has two main components: the adhesive layer and the adherends. These components are combined in a sandwich type configuration as shown in Fig. 5.1.

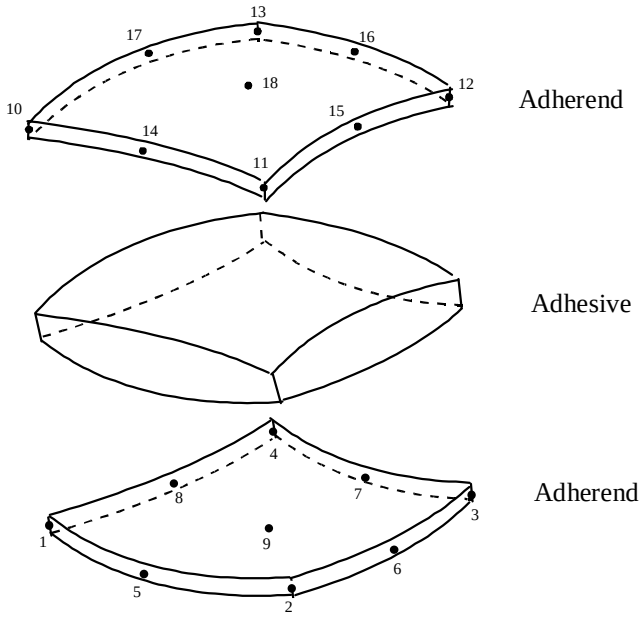

Figure 5.1. Configuration of the adhesive element.

The model consists of two adherends represented by general shell elements and the adhesive layer modeled as a solid element with offset nodes in the mid-planes of the adherends. In the work by Taylor (1996), the adherends are modeled by Mindlin plate elements. Since curved structures are modeled better with shell than with plate elements, the newly formulated element enhances the rate of converge for practical joint configurations.

The new version of the element includes geometrical nonlinearities in the formulation. This is an important improvement since adhesive joints are generally subjected to large displacements. For example, Dattaguru (1984) demonstrated the importance of the inclusion of geometrical nonlinearities in the modeling of adhesive joints.

In chapter 2, the basic incremental equations of equilibrium for a geometric nonlinear isoparametric finite element was presented. In the next two sections the basic components of those incremental equations are presented for the adherends and the adhesive.

5.2 Adherends

In the modeling of the adherends as shell elements, the formulation given by Bathe (1995) is followed. Fig. 5.2 shows the element configuration.

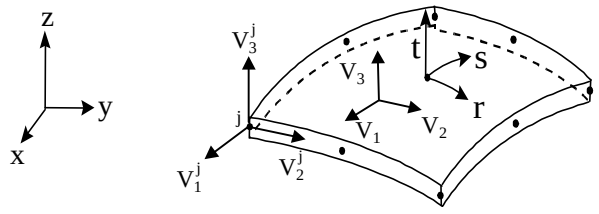

Figure 5.2. Adherend element configuration.

V_1, V_2, and V_3 are orthonormal vectors; V_1 and V_2 are tangent to the shell's midplane, and V_3 is the vector normal to the mid-plane of the shell. The variables r, s, and t are the element local coordinates and x, y, and z are the global coordinates.

The number of degrees of freedom per node of the adherend element differs from those of an ordinary shell element. Usually shell elements can be modeled using five degrees of freedom per node. However, the adherend shell element has six degrees of freedom per node to give the element the flexibility to be used in ABAQUS and to be connected with any arbitrary element. Fig. 5.3 shows the degrees of freedom used by the adherend shell

element for each node.

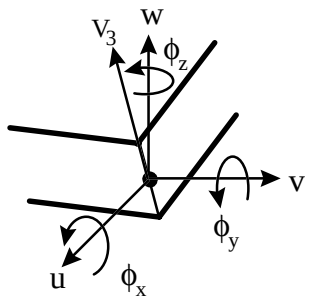

Figure 5.3. Degrees of freedom per node.

The displacement vector

$$\begin{Bmatrix} u \\ v \\ w \end{Bmatrix} = \sum N_i \begin{Bmatrix} u_i \\ v_i \\ w_i \end{Bmatrix} + \sum N_i t \frac{h_i}{2} \begin{Bmatrix} \phi_{xi} \\ \phi_{yi} \\ \phi_{zi} \end{Bmatrix} x V_{3_i} \tag{5.1}$$

where

u, v, and w	=	displacements in the three global directions
N_i	=	quadratic Lagrange interpolation polynomial
u_i, v_i, and w_i	=	displacements of node i
t	=	element coordinate in the V_3 direction
h_i	=	thickness of the plate at node i
ϕ_{xi}, ϕ_{yi}, and ϕ_{zi}	=	rotations of node i about the global coordinates axes

Eq. 5.1 can be expressed generically as

$$u = \sum N_k u^k + \sum N_k t \vec{\phi}^k x \vec{V}_{3_k} \tag{5.2}$$

where

$$u = \begin{Bmatrix} u \\ v \\ w \end{Bmatrix} = \begin{Bmatrix} u_1 \\ u_2 \\ u_3 \end{Bmatrix} \tag{5.3}$$

u_i = displacement vector component in the i^{th} global direction

$$u^k = \begin{Bmatrix} u_1^k \\ u_2^k \\ u_3^k \end{Bmatrix} \tag{5.4}$$

u_i^k = displacement vector component of node k^{th} in the i^{th} global direction

$$\vec{\phi}^k = \begin{Bmatrix} \phi_x^k \\ \phi_y^k \\ \phi_z^k \end{Bmatrix} = \begin{Bmatrix} \phi_1^k \\ \phi_2^k \\ \phi_3^k \end{Bmatrix} \tag{5.5}$$

The B matrix can be computed using Eq. 5.2 and obtaining the corresponding derivatives of the displacements. These derivatives are

$$\begin{Bmatrix} u_{1,x} \\ u_{1,y} \\ u_{1,z} \\ u_{2,x} \\ \vdots \\ u_{3,z} \end{Bmatrix} = \begin{bmatrix} J^{-1} & 0 & 0 \\ 0 & J^{-1} & 0 \\ 0 & 0 & J^{-1} \end{bmatrix} \begin{Bmatrix} u_{1,r} \\ u_{1,s} \\ u_{1,t} \\ u_{2,r} \\ \vdots \\ u_{3,t} \end{Bmatrix} \tag{5.6}$$

where J^{-1} is the inverse of the Jacobian matrix defined as

$$J = \begin{bmatrix} \partial^t x_1 / \partial r & \partial^t x_2 / \partial r & \partial^t x_3 / \partial r \\ \partial^t x_1 / \partial s & \partial^t x_2 / \partial s & \partial^t x_3 / \partial s \\ \partial^t x_1 / \partial t & \partial^t x_2 / \partial t & \partial^t x_3 / \partial t \end{bmatrix} \tag{5.7}$$

Particularly, the expression for the derivative of the displacement in the i direction with respect to the j coordinate, both referred to time t, is

$$\frac{\partial^t u_i}{\partial^t x_j} = \sum_k N_{k,1} u_i^{k\,t} J_{j1}^{-1} + \sum_k N_{k,2} u_i^{k\,t} J_{j2}^{-1} + \sum_k N_{k,1} t\vec{\phi}_i^k x \vec{V}_{3_k}{}^t J_{j1}^{-1} + \sum_k N_{k,2} t\vec{\phi}_i^k x \vec{V}_{3_k}{}^t J_{j2}^{-1} + \sum_k N_k \vec{\phi}_i^k x \vec{V}_{3_k}{}^t J_{j3}^{-1} \tag{5.8}$$

$\left(\vec{\phi}^k x \vec{V}_{3k}\right)_i$ = component in the i direction of the cross product between the angle displacement vector and the normal to the adherend midplane.

The strain vector referred to the element coordinate system is

$$\begin{Bmatrix} u_{1,r} \\ u_{1,s} \\ u_{1,t} \\ u_{2,r} \\ \vdots \\ u_{3,t} \end{Bmatrix} = \sum_{i}^{N} \begin{bmatrix} N_{i,r} & 0 & 0 & 0 & \frac{th_i N_{i,r} \ell_3}{2} & -\frac{th_i N_{i,r} \ell_2}{2} \\ N_{i,s} & 0 & 0 & 0 & \frac{th_i N_{i,s} \ell_3}{2} & -\frac{th_i N_{i,s} \ell_2}{2} \\ 0 & 0 & 0 & 0 & \frac{h_i N_i \ell_3}{2} & -\frac{h_i N_i \ell_2}{2} \\ 0 & N_{i,r} & 0 & -\frac{th_i N_{i,r} \ell_3}{2} & 0 & \frac{th_i N_{i,r} \ell_1}{2} \\ \vdots & \vdots & \vdots & \vdots & \vdots & \vdots \\ 0 & 0 & 0 & \frac{h_i N_i \ell_2}{2} & -\frac{h_i N_i \ell_1}{2} & 0 \end{bmatrix} \begin{Bmatrix} u_1 \\ u_2 \\ u_3 \\ \phi_1 \\ \phi_2 \\ \phi_3 \end{Bmatrix}_i \tag{5.9}$$

This can also be expressed as

$$\underbrace{\begin{Bmatrix} u_{1,r} \\ u_{1,s} \\ u_{1,t} \\ u_{2,r} \\ \vdots \\ u_{3,t} \end{Bmatrix}}_{\{u_{,i}\}} = \underbrace{\begin{bmatrix} N_{i,r} & 0 & 0 & 0 & \frac{th_i N_{i,r} \ell_3}{2} & -\frac{th_i N_{i,r} \ell_2}{2} & \\ N_{i,s} & 0 & 0 & 0 & \frac{th_i N_{i,s} \ell_3}{2} & -\frac{th_i N_{i,s} \ell_2}{2} & \\ \cdots\ 0 & 0 & 0 & 0 & \frac{h_i N_i \ell_3}{2} & -\frac{h_i N_i \ell_2}{2} & \cdots \\ 0 & N_{i,r} & 0 & -\frac{th_i N_{i,r} \ell_3}{2} & 0 & \frac{th_i N_{i,r} \ell_1}{2} & \\ \vdots & \vdots & \vdots & \vdots & \vdots & \vdots & \\ 0 & 0 & 0 & \frac{h_i N_i \ell_2}{2} & -\frac{h_i N_i \ell_1}{2} & 0 & \end{bmatrix}}_{[T]} \underbrace{\begin{Bmatrix} \vdots \\ u_1^i \\ u_2^i \\ u_3^i \\ \phi_1^i \\ \phi_2^i \\ \phi_3^i \\ \vdots \end{Bmatrix}}_{\{\delta\}} \tag{5.10}$$

or

$$\{u_{,i}\} = [T]\{\delta\} \tag{5.11}$$

Expressing the strains in the form

$$\{\varepsilon_x \quad \varepsilon_y \quad \varepsilon_z \quad \gamma_{xy} \quad \gamma_{yz} \quad \gamma_{xz}\}^T = [H]\{u_{1,x} \quad u_{1,y} \quad u_{1,z} \quad u_{2,x} \quad \cdots \quad u_{3,z}\} \tag{5.12}$$

where

$$[H] = [H]_L + [H]_{NL} \tag{5.13}$$

$$[H]_L = \begin{bmatrix} 1 & 0 & 0 & 0 & 0 & 0 & 0 & 0 & 0 \\ 0 & 0 & 0 & 0 & 1 & 0 & 0 & 0 & 0 \\ 0 & 0 & 0 & 0 & 0 & 0 & 0 & 0 & 1 \\ 0 & 1 & 0 & 1 & 0 & 0 & 0 & 0 & 0 \\ 0 & 0 & 0 & 0 & 0 & 1 & 0 & 1 & 0 \\ 0 & 0 & 1 & 0 & 0 & 0 & 1 & 0 & 0 \end{bmatrix} \tag{5.14}$$

$$[H]_{NL} = \begin{bmatrix} 1 & 0 & 0 & 0 & 0 & 0 & 0 & 0 & 0 \\ 0 & 0 & 0 & 1 & 0 & 0 & 0 & 0 & 0 \\ 0 & 0 & 0 & 0 & 0 & 0 & 1 & 0 & 0 \\ 0 & 1 & 0 & 0 & 0 & 0 & 0 & 0 & 0 \\ 0 & 0 & 0 & 0 & 1 & 0 & 0 & 0 & 0 \\ 0 & 0 & 0 & 0 & 0 & 0 & 0 & 1 & 0 \\ 0 & 0 & 1 & 0 & 0 & 0 & 0 & 0 & 0 \\ 0 & 0 & 0 & 0 & 0 & 1 & 0 & 0 & 0 \\ 0 & 0 & 0 & 0 & 0 & 0 & 0 & 0 & 1 \end{bmatrix} \tag{5.15}$$

and combining Eqs. (5.6) – (5.10), the following expression can be found:

$$\{\varepsilon_x \quad \varepsilon_y \quad \varepsilon_z \quad \gamma_{xy} \quad \gamma_{yz} \quad \gamma_{xz}\}^T = [B]\{\cdots \quad u_1 \quad u_2 \quad u_3 \quad \phi_1 \quad \phi_2 \quad \phi_3 \quad \cdots\}^T \tag{5.16}$$

$$[B] = [H][J]^{-1}[T] \tag{5.17}$$

The coordinates for a generic point on the shell are defined as

$$\begin{Bmatrix} x \\ y \\ z \end{Bmatrix} = \begin{Bmatrix} x_1 \\ x_2 \\ x_3 \end{Bmatrix} = \sum_k^N N_k \begin{Bmatrix} x_1^k \\ x_2^k \\ x_3^k \end{Bmatrix} + \sum_k^N N_k t \frac{h_k}{2} \vec{V}_{3_i} \tag{5.18}$$

The constitutive relation is

$$C = \begin{bmatrix} E_{11} & E_{12} & 0 & 0 & 0 & 0 \\ E_{12} & E_{22} & 0 & 0 & 0 & 0 \\ 0 & 0 & 0 & 0 & 0 & 0 \\ 0 & 0 & 0 & G_{12} & 0 & 0 \\ 0 & 0 & 0 & 0 & \frac{5}{6}G_{23} & 0 \\ 0 & 0 & 0 & 0 & 0 & \frac{5}{6}G_{31} \end{bmatrix} \tag{5.19}$$

The third row and column are empty because σ_{33} is negligible for plates and shells.

5.3 Adhesive

The adhesive layer is modeled by 3-D solid elements, "bricks," within offset nodes to the shell midplanes. This is equivalent to condensing out the degree of freedom of the continuum elements into the degree of freedom of the adjacent shells that model the adherends (Fig. 5.4). The formulation of this element is similar to Taylor's (1996) but includes geometrical nonlinearities. The element is called ADH3D following the notation given by Taylor (1996).

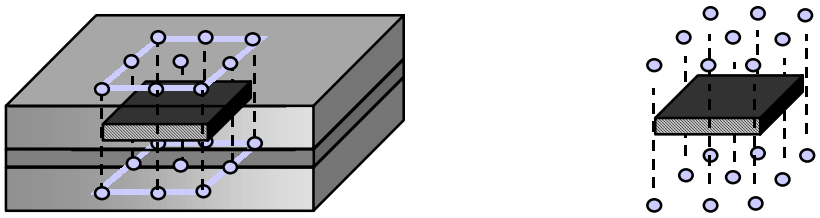

Figure 5.4. 3-D adhesive finite element configuration.

Displacement continuity is desired at the adhesive-adherend interfaces. This improves the accuracy of relatively coarse meshes. Fig. 5.5 shows the actual and the parent elements, and Fig. 5.6 shows the node arrangement and numbering in the parent element.

Quadratic interpolation functions are used in the planes of the element parallel to the adherend mid-planes in order to have compatibility of the displacements in the

adhesive/adherends interfaces. In the thickness direction, linear interpolation functions are used. Quadratic and linear Lagrange polynomials are used.

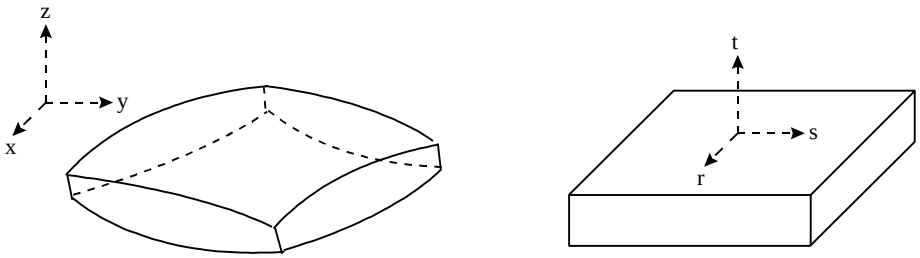

Real Element Parent Element

Figure 5.5. Finite and parent elements.

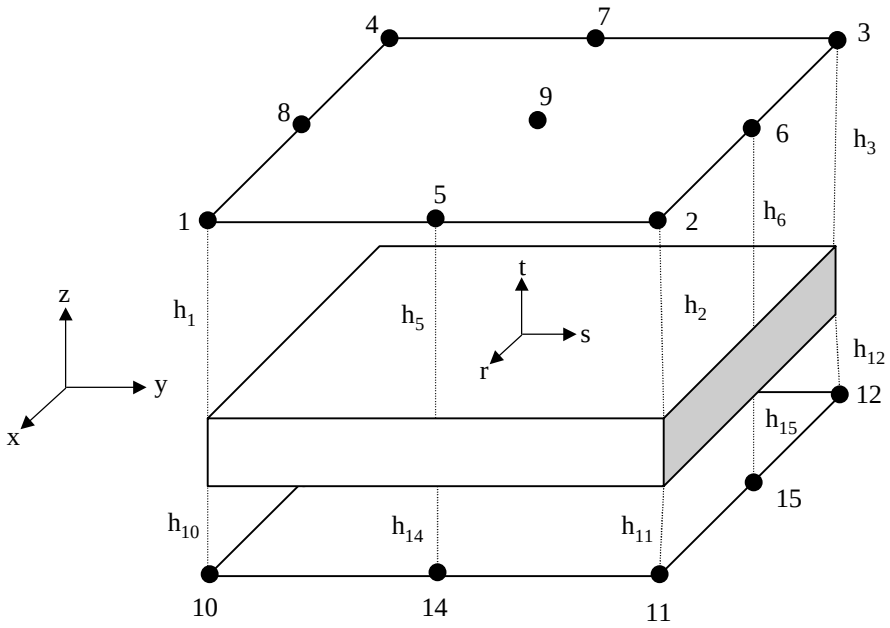

Figure 5.6. Adhesive element finite element configuration.

The coordinates of a generic point in the element are defined as

$$x_i = \sum_{k=1}^{n} N_k x_i^k \qquad (5.20)$$

and the displacements are

$$u_i = \sum_{k=1}^{n} N_k u_i^k \tag{5.21}$$

where

x_i = coordinate in the i^{th} direction of a generic point in the element

u_i = displacement in the i^{th} direction of a generic point in the element

x^k_i = coordinate in the i^{th} direction of the node k

u^k_i = displacement in the i^{th} direction of the node k

N_k = interpolation functions as defined in Taylor (1996)

The displacement vector can be expressed as follows:

$$\{u\} = \begin{Bmatrix} u \\ v \\ w \end{Bmatrix} = \begin{Bmatrix} u_1 \\ u_2 \\ u_3 \end{Bmatrix}$$

The nodal coordinates in the adhesive are defined as a function of the nodal coordinates of the adherends as

$$\begin{Bmatrix} x_1^k \\ x_2^k \\ x_3^k \end{Bmatrix} = \begin{Bmatrix} x^k_{1\,adher} \\ x_{2_{adher}} \\ x_{3_{adher}} \end{Bmatrix} + \frac{h_k}{2} \vec{V}_{3k} \tag{5.22}$$

and the nodal displacements are

$$\begin{Bmatrix} u^k \\ v^k \\ w^k \end{Bmatrix} = \begin{Bmatrix} u^k_{adher} \\ v^k_{adher} \\ w^k_{adher} \end{Bmatrix} + \frac{h_k}{2} \begin{Bmatrix} \phi^k_x \\ \phi^k_y \\ \phi^k_z \end{Bmatrix} x \vec{V}_{3k} \tag{5.23}$$

Analogous to the two-dimensional element, the coefficients of the interpolation functions for the adhesive, $N_{k,}$ are obtained by imposing equal displacements of adherends and adhesive in their interfaces. Accordingly,

$$\{u\}^{bottom}_{adhes} = \sum_{i}^{18} [N_i]^{bottom}_{adhes} \{u_i\}_{adhes} = \{u\}^{top}_{botton\ adher} = \sum_{i}^{9} [N_i]^{top}_{bottom\ adher} \{u_i\}_{bottom\ adher} \tag{5.22}$$

$$\{u\}^{top}_{adhes} = \sum_{1}^{18} [N_i]^{top}_{adhes} \{u_i\}_{adhes} = \{u\}^{bottom}_{upper\ adher} = \sum_{i}^{9} [N_i]^{bottom}_{upper\ adher} \{u_i\}_{upper\ adher} \qquad (5.23)$$

where

$[N_i]^{top}_{adhes}$ and $[N_i]^{bottom}_{adhes}$ = interpolation functions for the adhesive evaluated at the top and bottom interfaces, respectively.

$[N_i]^{top}_{upper\ adher}$ and $[N_i]^{bottom}_{bottom\ adhes}$ = interpolation functions for the upper and bottom adherends evaluated at the upper adherend-adhesive and bottom adherend-adhesive interfaces, respectively. These functions are known.

$[u]^{top}_{adhes}$ and $[u]^{bottom}_{adhes}$ = displacements of the adhesive at the top and bottom interfaces, respectively.

$[u]^{top}_{bottom\ adher}$ and $[u]^{bottom}_{upper\ adher}$ = displacements of the bottom adherend at the top and the upper adherend at the bottom, respectively.

$[u]^{top}_{adhes}$ and $[u]^{bottom}_{adhes}$ = displacements of the adhesive at the top and bottom interfaces, respectively.

$[u_i]_{adhes}$ = nodal displacements of the adhesive.

$[u_i]_{upper\ adher}$ and $[u_i]_{bottom\ adher}$ = nodal displacements of the adhesive at the top and bottom interfaces, respectively.

Displacements, u, v, and w are defined as complete quadratic polynomials in planes parallel to the shell's midplanes, the ρ and σ directions in Fig 5.3. Complete linear polynomials approximate these displacements in the direction perpendicular to the shell's midplanes, t in Fig 5.3. Substituting those displacement approximations in Eqs. 5.22 and 5.23, the coefficients of the trial functions are obtained. More details of this formulation can be found in Taylor (1996).

The derivatives of the displacements and the Jacobian matrix have the same form as Eqs. 5.6 and 5.7. Particularly, the expression for the derivative of the displacement in the i^{th} direction with respect to the j^{th} coordinate, both referred to time t, is

$$\frac{\partial^t u_i}{\partial^t x_j} = \sum_k N_{k,1}(u_i^{k\,t} + \frac{h_k}{2}(\vec{\phi}^k x \vec{V}_{3k})_i)J_{j1}^{-1} + \sum_k N_{k,2}(u_i^{k\,t} + \frac{h_k}{2}(\vec{\phi}^k x \vec{V}_{3k})_i)J_{j2}^{-1} + \sum_k N_{k,3}(u_i^{k\,t} + \frac{h_k}{2}(\vec{\phi}^k x \vec{V}_{3k})_i)^t J_{j3}^{-1} \tag{5.24}$$

where $\left(\vec{\phi}^k x \vec{V}_{3k}\right)_i$ is the component in the i direction of the cross product between the angular displacement vector and the normal to the adherend's midplane. This can be expressed as

$$\{u\}_{,x} = J^{-1}\{u\}_{,r} \tag{5.25}$$

where

$\{u\}_{,x}$ = derivative of displacement referred to the global system of coordinates
$\{u\}_{,r}$ = derivative of displacement referred to the local system of coordinates

The derivatives referred to the element coordinate system are

$$\begin{Bmatrix} u_{1,r} \\ u_{1,s} \\ u_{1,t} \\ u_{2,r} \\ \vdots \\ u_{3,t} \end{Bmatrix} = \sum_i^N \begin{bmatrix} N_{i,r} & 0 & 0 & 0 & \frac{h_i N_{i,r} \ell_3}{2} & -\frac{h_i N_{i,r} \ell_2}{2} \\ N_{i,s} & 0 & 0 & 0 & \frac{h_i N_{i,s} \ell_3}{2} & -\frac{h_i N_{i,s} \ell_2}{2} \\ N_{i,t} & 0 & 0 & 0 & \frac{h_i N_{i,t} \ell_3}{2} & -\frac{h_i N_{i,t} \ell_2}{2} \\ 0 & N_{i,r} & 0 & -\frac{h_i N_{i,r} \ell_3}{2} & 0 & \frac{h_i N_{i,r} \ell_1}{2} \\ \vdots & \vdots & \vdots & \vdots & \vdots & \vdots \\ 0 & 0 & N_i,t & \frac{h_i N_{i,t} \ell_2}{2} & -\frac{h_i N_{i,t} \ell_1}{2} & 0 \end{bmatrix} \begin{Bmatrix} u_1 \\ u_2 \\ u_3 \\ \phi_1 \\ \phi_2 \\ \phi_3 \end{Bmatrix}_i \tag{5.26}$$

This can also be expressed as

$$\{u,_i\} = [T]\{\delta\} \tag{5.27}$$

where {u,i}, [T], and {d} have the same meaning as in Eq. 5.11. The strains can be expressed in the following form:

$$\{\varepsilon_x \quad \varepsilon_y \quad \varepsilon_z \quad \gamma_{xy} \quad \gamma_{yz} \quad \gamma_{xz}\}^T = [H]\{u_{1,x} \quad u_{1,y} \quad u_{1,z} \quad u_{2,x} \quad \cdots \quad u_{3,z}\} \tag{5.28}$$

where

$$[H] = [H]_L + [H]_{NL} \tag{5.29}$$

and $[H]_L$ and $[H_{NL}]$ are defined in Eqs. 5.13 and 5.14. Combining Eqs. 5-25 – 5-27, the following expression can be found:

$$\{\varepsilon_x \quad \varepsilon_y \quad \varepsilon_z \quad \gamma_{xy} \quad \gamma_{yz} \quad \gamma_{xz}\}^T = [B]\{\cdots \quad u_1 \quad u_2 \quad u_3 \quad \phi_1 \quad \phi_2 \quad \phi_3 \quad \cdots\}^T \tag{5.30}$$

and

$$[B] = [H][J]^{-1}[T] \tag{5.31}$$

The constitutive relation is

$$C = \frac{E}{(1+\mu)(2\mu-1)}\begin{bmatrix} (\mu-1) & -\mu & -\mu & 0 & 0 & 0 \\ -\mu & (\mu-1) & -\mu & 0 & 0 & 0 \\ -\mu & -\mu & (\mu-1) & 0 & 0 & 0 \\ 0 & 0 & 0 & \frac{(2\mu-1)}{2} & 0 & 0 \\ 0 & 0 & 0 & 0 & \frac{(2\mu-1)}{2} & 0 \\ 0 & 0 & 0 & 0 & 0 & \frac{(2\mu-1)}{2} \end{bmatrix} \tag{5.32}$$

Once the [B] matrix has been built, the stiffness matrix corresponding to the adhesive layer can be computed. The matrix of the whole element is the assembly of the matrices of the two adherends and the adhesive layer.

5.4 Thermal and Moisture Effects

Thermal and moisture effects will be taken into account as in Taylor (1996) by defining initial strains, ε_o ,which do not produce stresses. Therefore, the initial strain tensor should be substracted from the total strain tensor to compute stresses. Accordingly, the stress-strain relation or constitutive law will take the form

$$\sigma = C(\varepsilon - \varepsilon_0) \tag{5.33}$$

$$\varepsilon_0 = \begin{bmatrix} \varepsilon_x \\ \varepsilon_y \\ \varepsilon_z \\ \gamma_{yz} \\ \gamma_{xz} \\ \gamma_{xy} \end{bmatrix} = \begin{bmatrix} \alpha\Delta T + \beta\Delta M \\ \alpha\Delta T + \beta\Delta M \\ \alpha\Delta T + \beta\Delta M \\ 0 \\ 0 \\ 0 \end{bmatrix} \tag{5.34}$$

where

α = thermal expansion coefficient

β = moisture expansion coefficient

ΔT = change in temperature

ΔM = change in humidity

5.5 Examples

Two examples are used to test the 3-D adhesive element: the popular single lap joint, and a crack patch geometry. The single lap joint geometry is used to test stress distributions and geometrically nonlinear effects. The crack patch geometry provides the opportunity to test the element in a "real" 3-D scenario, a problem which cannot be accurately modeled in 2-D.

5.5.1 Single Lap Joint

The single lap joint specimen depicted in Fig 5.7 is modeled using the three-dimensional version of the adhesive finite element (ADH3D). Even though symmetry conditions could be used, the whole structure was modeled, including the two lateral shells, to avoid any kind of assumption or simplification in the model. However, it is strongly recommended to use symmetry conditions in order to reduce the time of data preparation and computer runs. For this specimen, half of the specimen in the longitudinal direction could be modeled defining appropriate boundary conditions (Fig. 5.8).

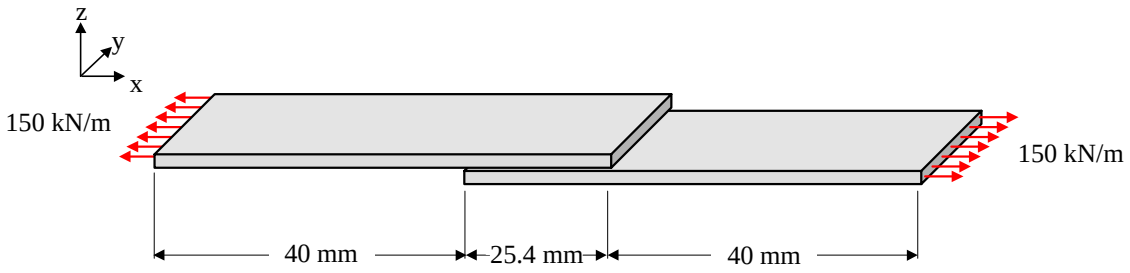

Figure 5.7. Three-dimensional single lap joint geometry.

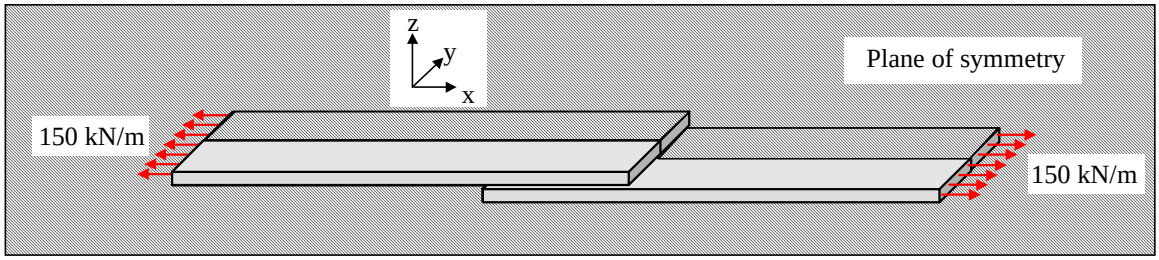

Figure 5.8. Single lap joint: symmetry condition.

The thickness of the adherends is1.6 mm, the adhesive layer thickness is 0.102 mm, and the specimen's width is 25.4 mm. All other geometric and loading properties are given in Fig. 5.6. Properties of the aluminum adherends and epoxy adhesive layer are given in Table 5.1.

Table 5.1. Single lap joint: material properties.

Material	E (GPa)	ν	h (mm)
Adherend	70.0	0.3	2.3
Adhesive	4.0	0.35	1.0

The finite element model of the single lap joint is composed of 1190 nodes and 252 elements (see Fig 5.9). The mesh is finer in the overlap than in the lateral shells. Since the most important effects occur at the overlap ends, the refinement of the mesh in this region would improve the accuracy of the model. In this example a uniform mesh models the whole overlap; however, the author recommends finer meshes in those regions where

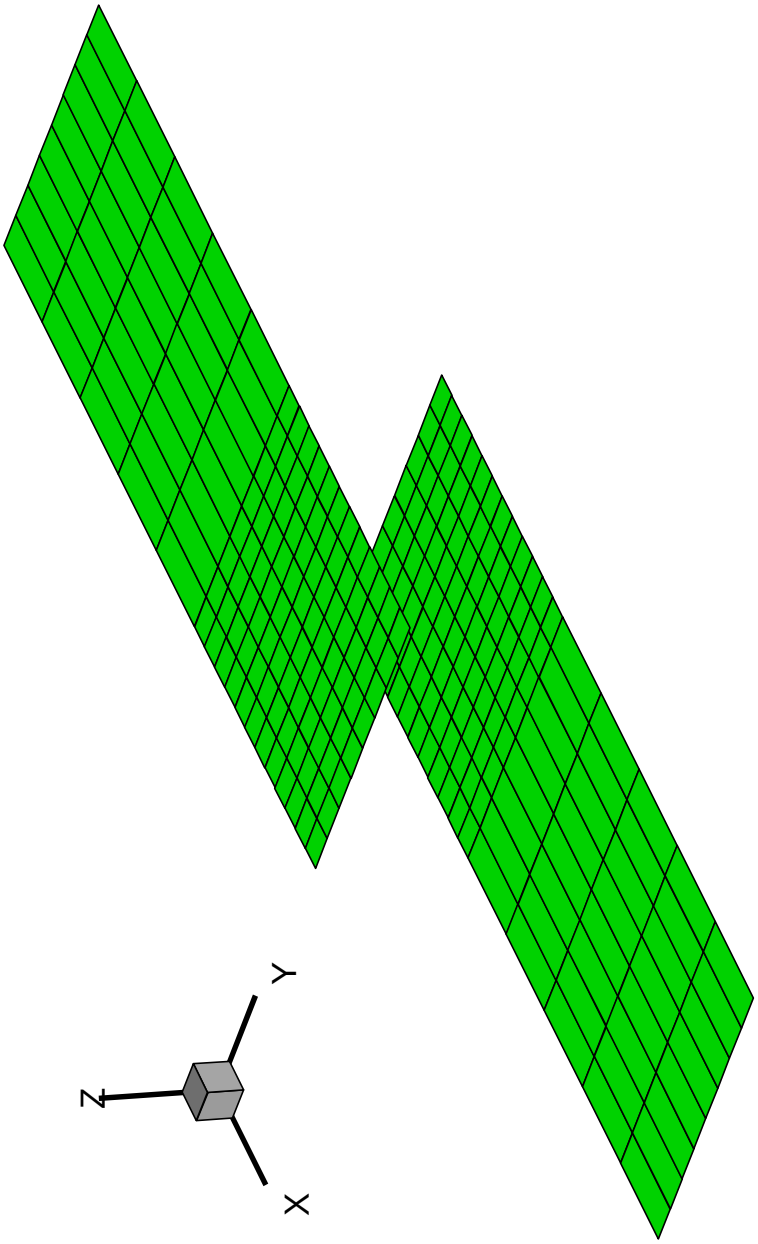

Figure 5.9. Finite element mesh of the single lap joint.

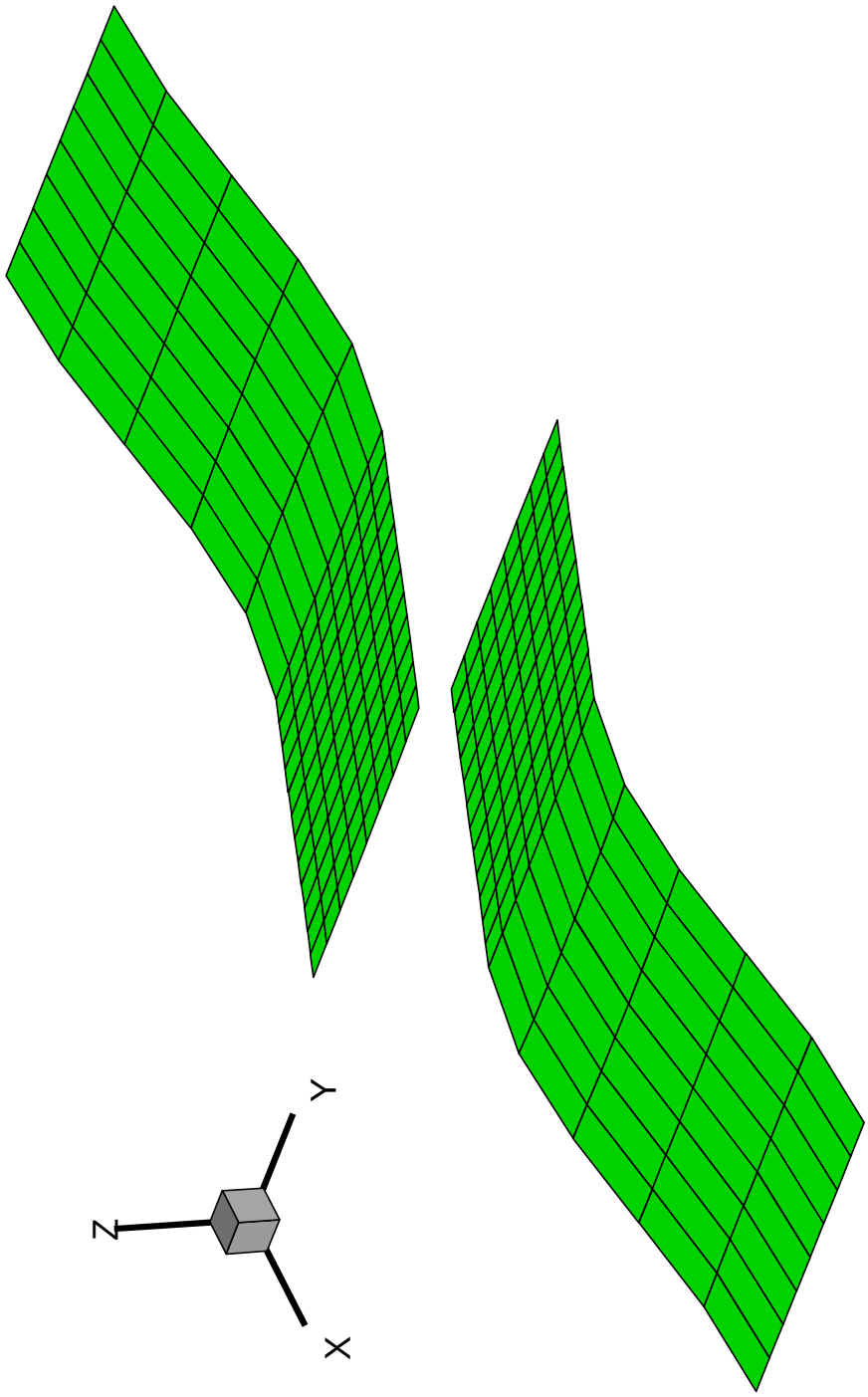

Figure 5.10. Displaced finite element mesh of the single lap joint.

stress concentrations are expected.

A displaced model is shown in Fig. 5.10; the symmetry condition with respect to a plane along the axial direction at the center of the joint (at y = 12.7) is illustrated in this figure. Also, anti-symmetry in the x direction can be readily verified. Displacements are amplified by a factor of 2 for display purposes.

Peel stress distributions at the mid-plane of the overlap region are shown in Fig. 5.11. Three-dimensional effects can be observed; specifically, the peel stresses are large at the center of the joint and decrease at the edges. This behavior is in qualitative agreement with experimental results of Adams et al. (1994). This is caused by Poisson effects and the anti-clastic bending of the adherends.

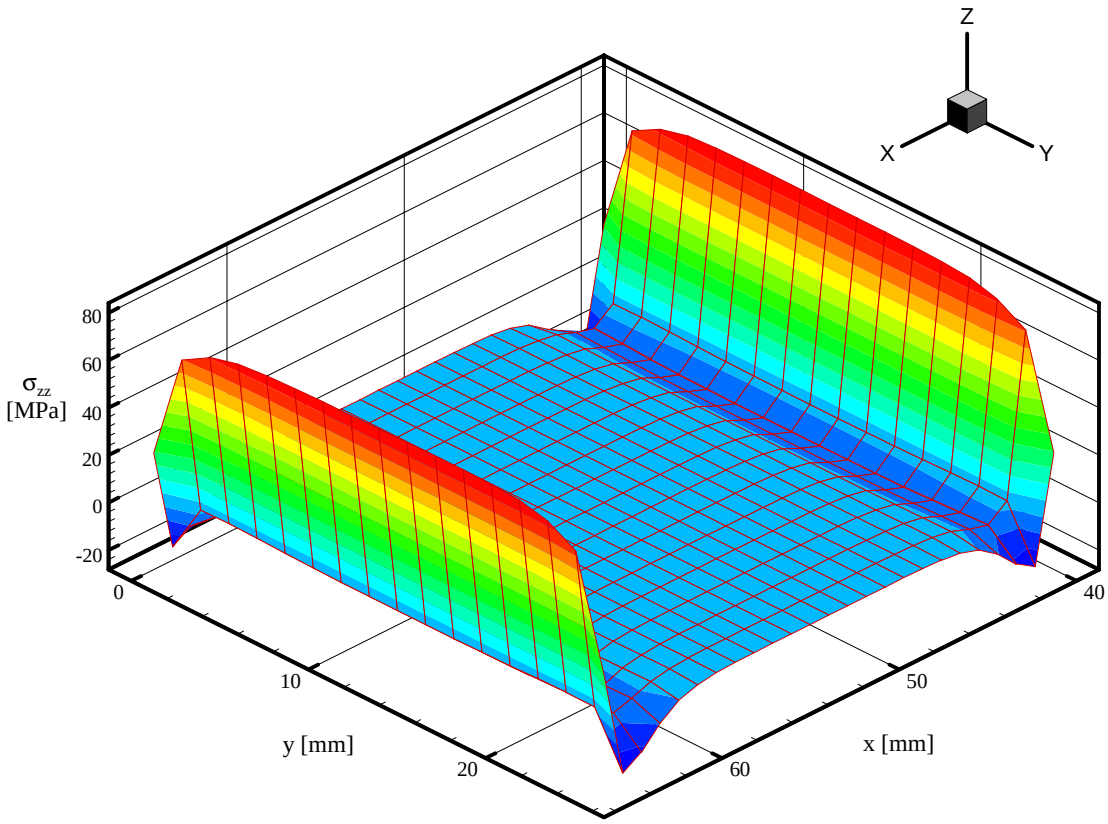

Figure 5.11. Peel stress (σ_{zz}) distribution in the midplane of the adhesive layer of the single lap joint example.

Figure 5.12 shows the shear stress (τ_{xz}) distribution in the xz direction Again three-dimensional effects are observed; however, they are not as pronounced as for the peel stresses.

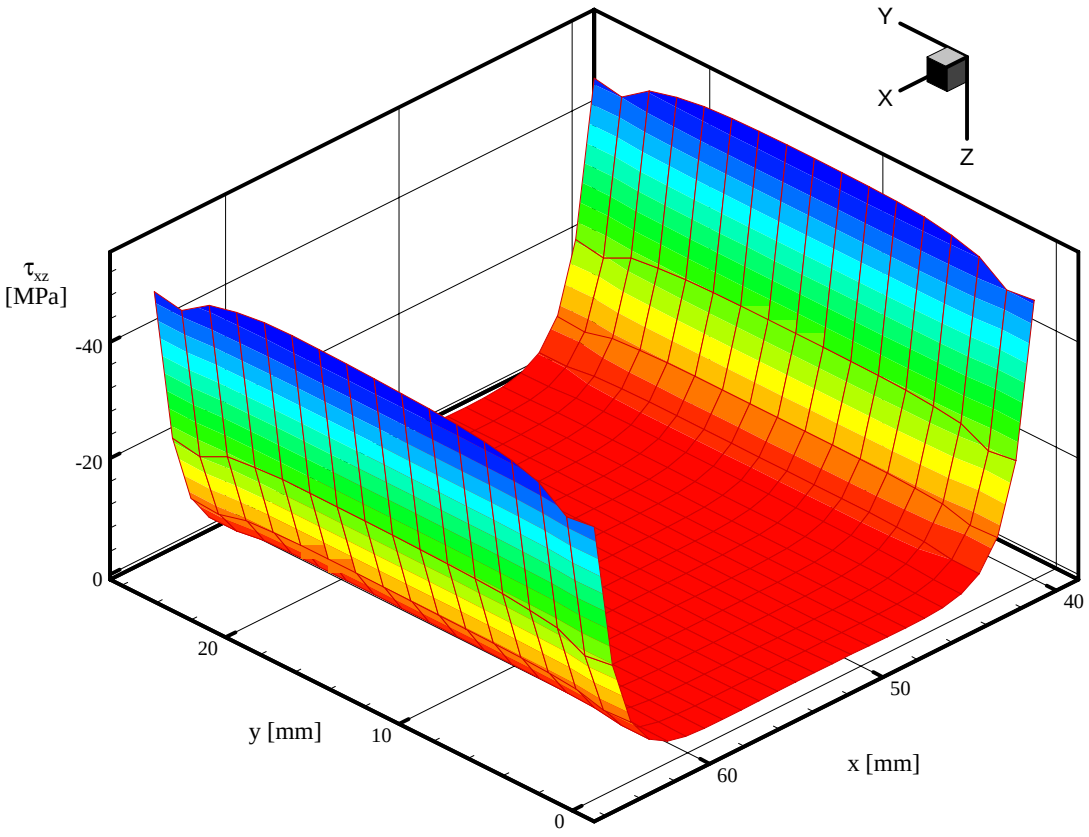

Figure 5.12. Shear stress (τ_{xz}) distribution in the midplane of the adhesive layer of the single lap joint example.

The shear stress (τ_{xy}),distribution in the xy direction in Fig. 5.13 shows a strong concentration at the two corners in the free edge of the overlap. However, the absolute values of these stresses are negligible relative to the other components of the stress tensor. The gaps shown in the corners suggest that a finer mesh is required in those regions.

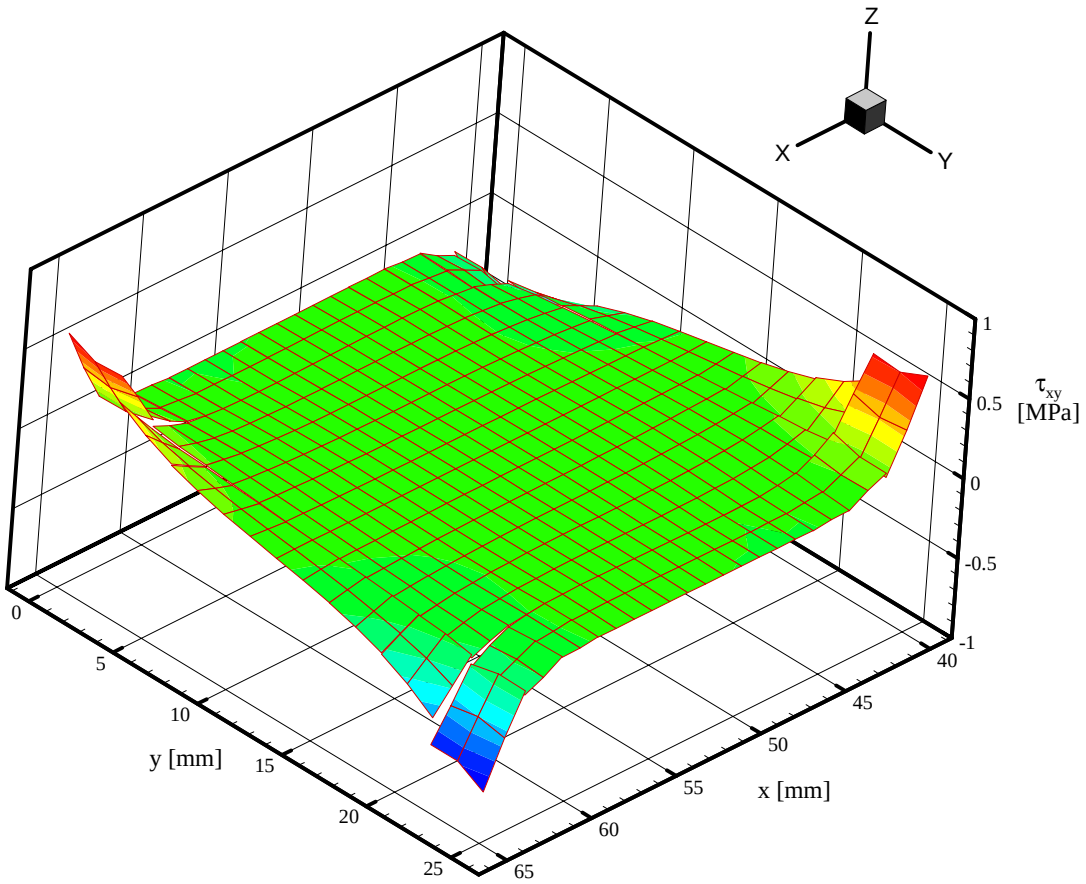

Figure 5.13. Shear stress (τ_{xy}) distribution in the midplane of the adhesive layer of the single lap joint example.

Fig. 5.14 shows the shear stress distribution in the yz direction (τ_{yz}). As in the case of τ_{xy}, there are strong stress concentrations at the two corners in the free edge of the overlap, but the maximum absolute values are on the order of the maximum values of the other components of the stress tensor.

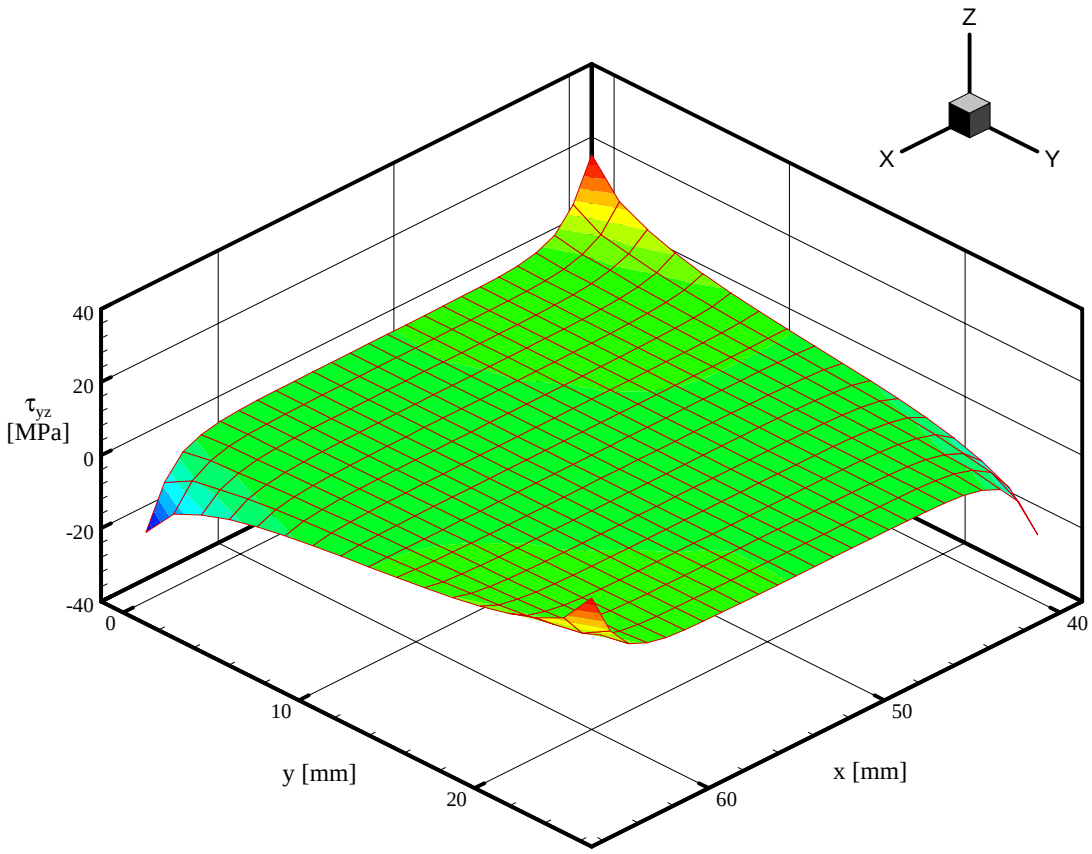

Figure 5.14. Shear stress (τ_{yz}) distribution in the midplane of the adhesive layer of the single lap joint example.

Figure 5.15 shows the stress distribution in the axial direction (σ_{xx}). The distribution is similar to that of the peel stresses (σ_{zz}).

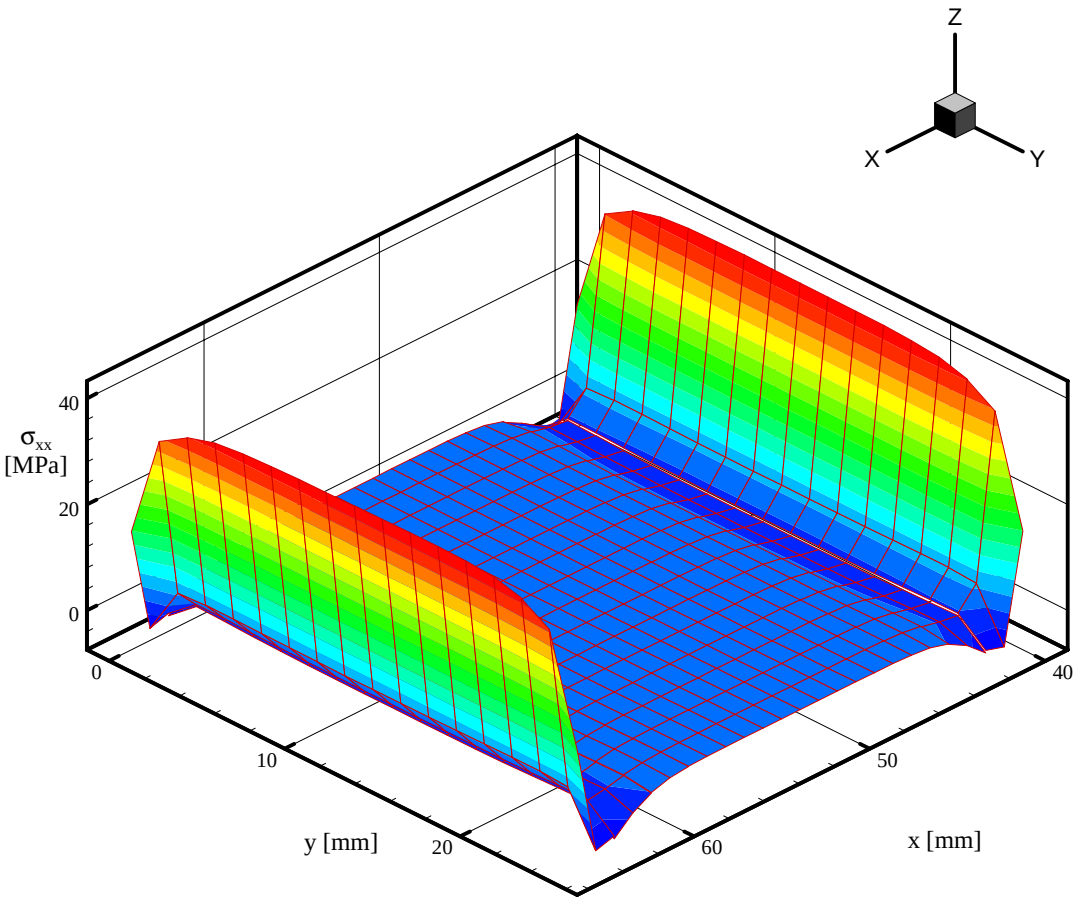

Figure 5.15. Axial stress (σ_{zz}) distribution in the midplane of the adhesive layer of the single lap joint example.

Figure 5.16 shows the stress distribution in the direction of the width of the overlap (σ_{yy}). Again, the distribution is similar to that of the peel stresses (σ_{zz}) as a consequence of the three-dimensional effects.

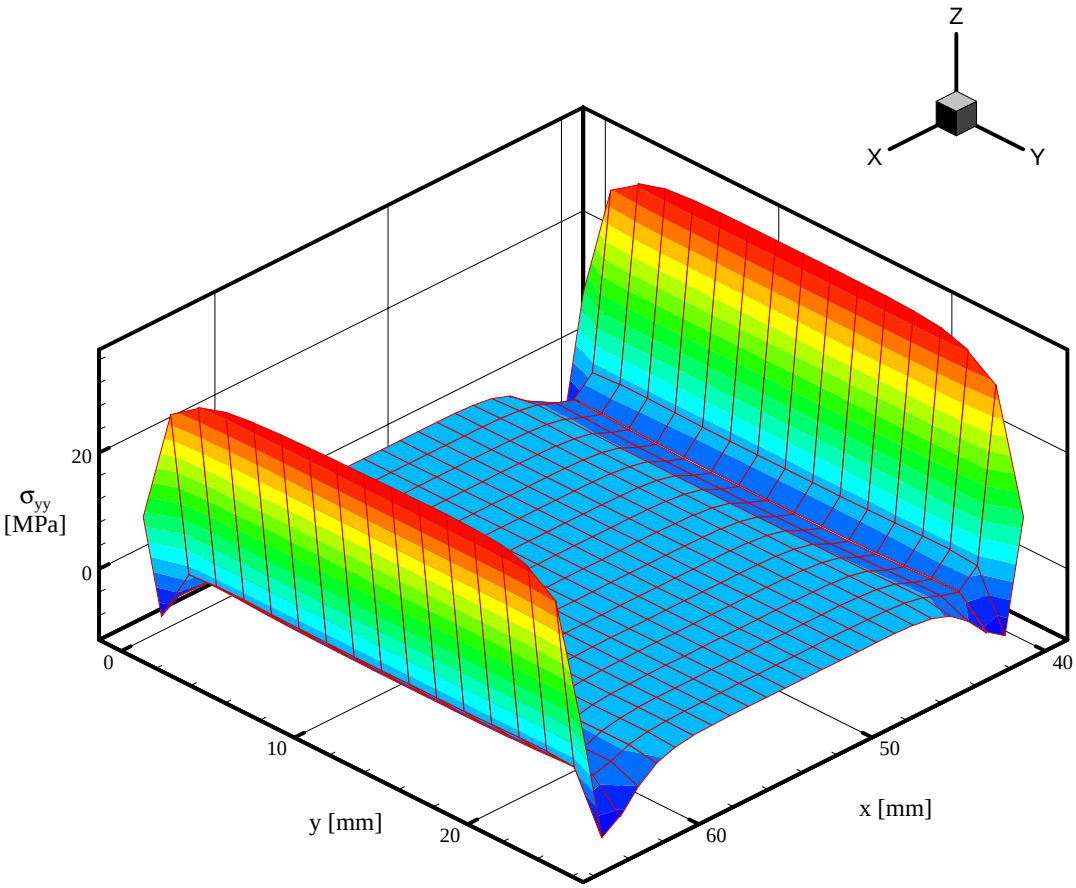

Figure 5.16. Transverse (σ_{yy}) stress distribution in the midplane of the adhesive layer of the single lap joint example.

Stress distributions in a single lap joint modeled with the new version of the three-dimensional adhesive finite element show complete agreement with those found in the literature (Tsai and Morton 1994a, Adams 1994,Taylor 1996).

5.5.2 Crack-Patch Geometry

A crack-patch repair geometry consists of a composite or metallic patch to reinforce a cracked metallic structure using adhesive materials. This technique has been very effictive in extending the service life of aging structures, such as aircraft, ships, and automobiles.

In this section a three-dimensional crack-patch geometry is analyzed with the ADH3D adhesive finite element model. This geometry is a true case of study where a 2-D analysis would not include important effects that can only be captured by using a three–dimensional model. Because of symmetry, half of the geometry was modeled. Figure 5.17 shows geometry and load conditions. Thermal, moisture, and nonlinear effects were not considered.

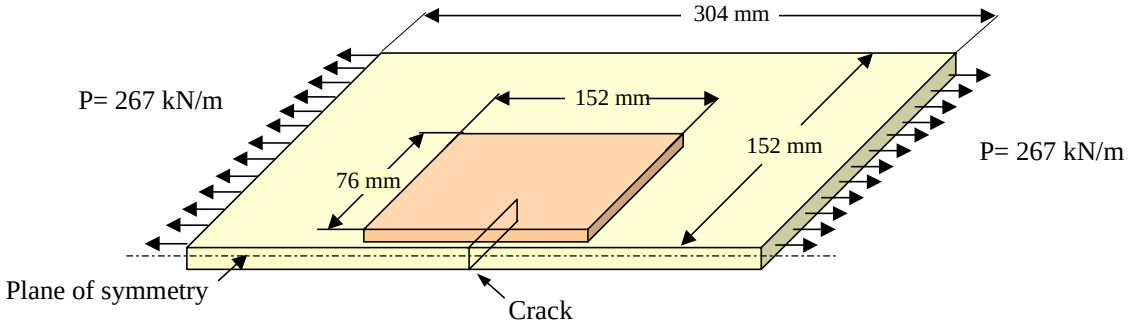

Figure 5.17. Crack-patch repair geometry.

The cracked shell is formed from a 2024-T3 aluminum alloy plate with a thickness of 2.3 mm; the crack half length is 25.4 mm. The patch is a carbon-epoxy tape with a uniform thickness of 1.0 mm, and the adhesive is an epoxy with a thickness of 0.23 mm. Material properties and thicknesses are summarized in Table 5.2.

Table 5.2. Crack-patch repair geometry, material properties.

Material	E (GPa)	ν_{12}	h (mm)	E_{22} (GPa)	G_{12} (GPa)
Adherend	71.7	0.3	2.3		
Patch	131	0.35	1.0	8.97	6.9
Adhesive	2.34	0.3	0.23		

The finite element model consists of 280 elements and 1222 nodes. Figure 5.18 shows the finite element mesh for a quarter of the structure and Fig. 5.19 displays an amplification of the patch region. The mesh is refined in the patch region and further refined in the

vicinity of the crack. Double symmetry conditions allow one to model only a quarter of the structure to reduce the number of degrees of freedom.

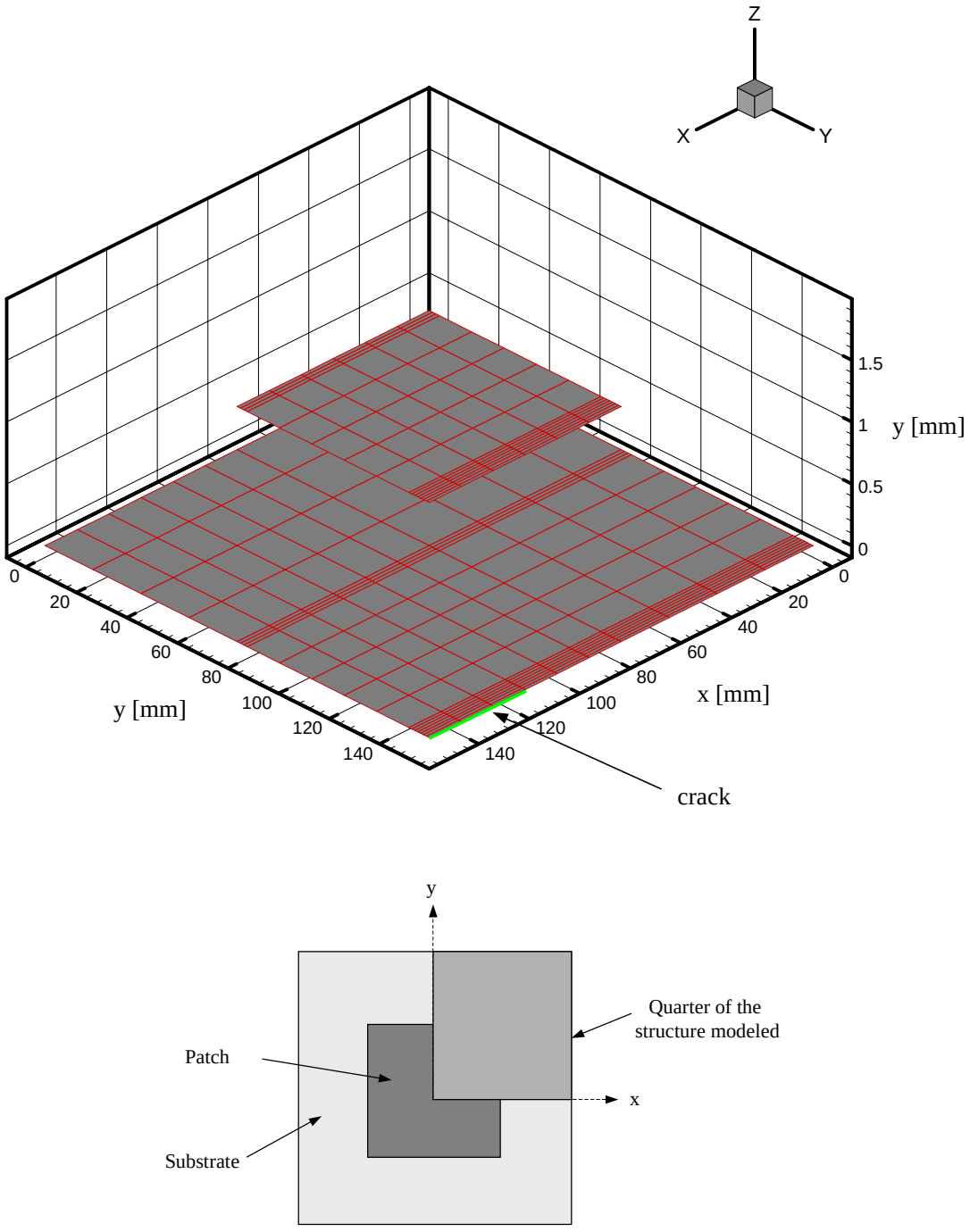

Figure 5.18. Finite element mesh of the crack-patch geometry.

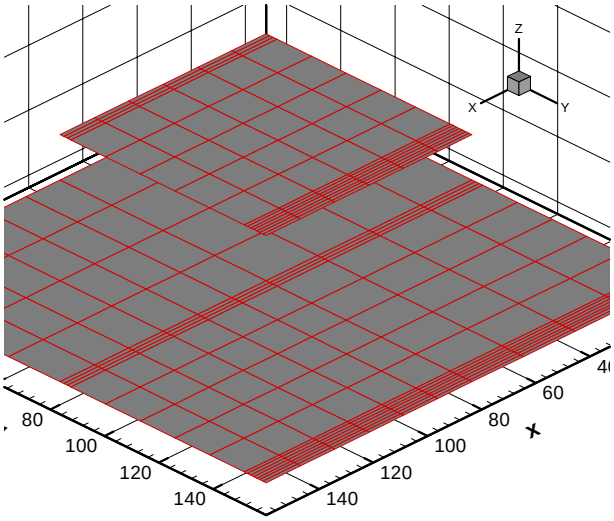

Figure 5.19. Finite element mesh of the crack-patch geometry. Magnification of the patch region.

A displaced model is shown in Fig. 5.20. The double symmetry conditions with respect to two perpendicular planes passing through the center of the structure are clearly shown in this figure.

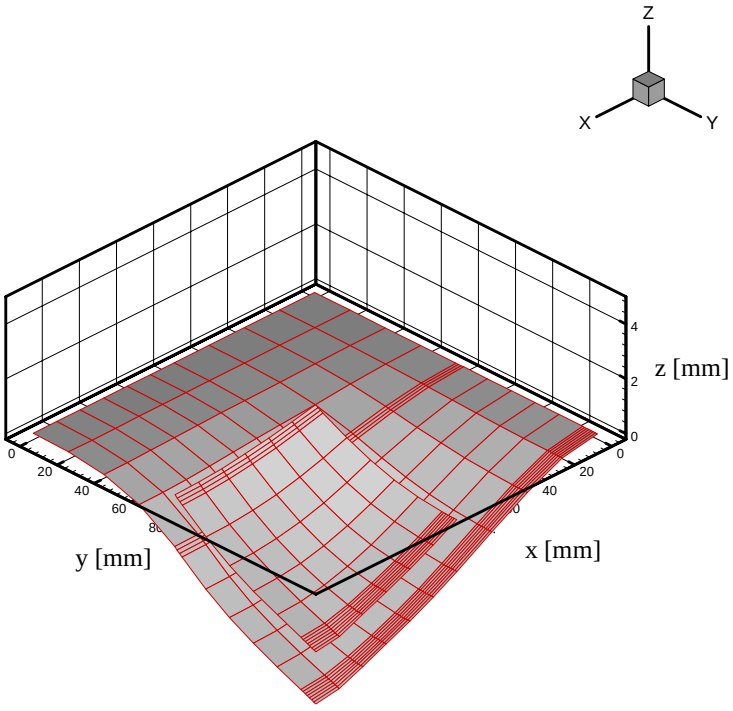

Figure 5.20. Displaced finite element mesh of the crack-patch geometry.

Peel stress distributions at the mid-plane of the patch region are shown in Fig. 5.21. It shows a large stress concentration in the crack region and a small concentration at the edges of the patch in the direction of loads.

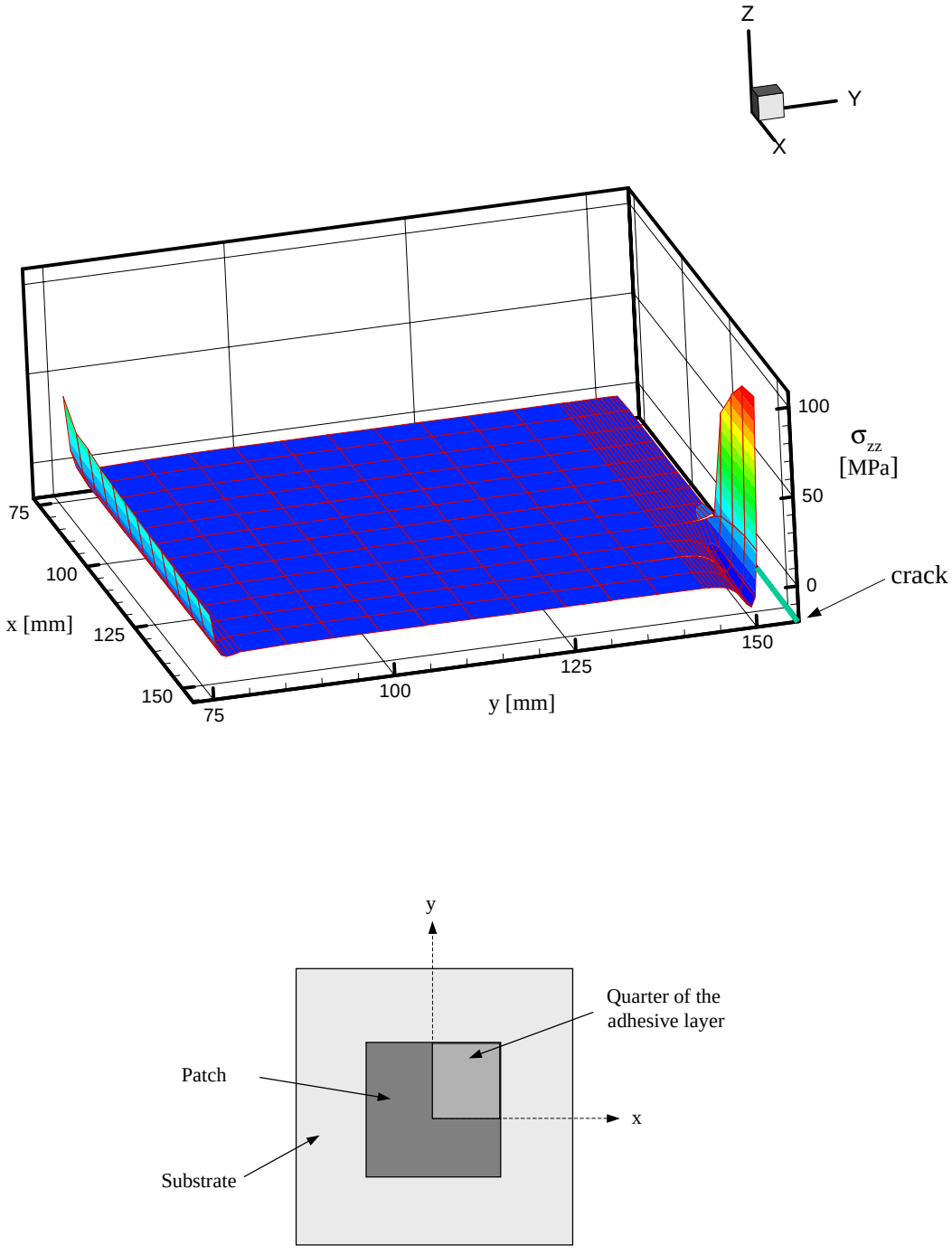

Figure 5.21. Transverse (σ_{zz}) stress distribution in the midplane of the adhesive layer quarter of the crack-patch repair example.

Figure 5.22 shows the shear stress (τ_{xz}) distribution in the xy direction. Again, a strong stress concentration is seen at the crack region and a smaller one at the patch edges.

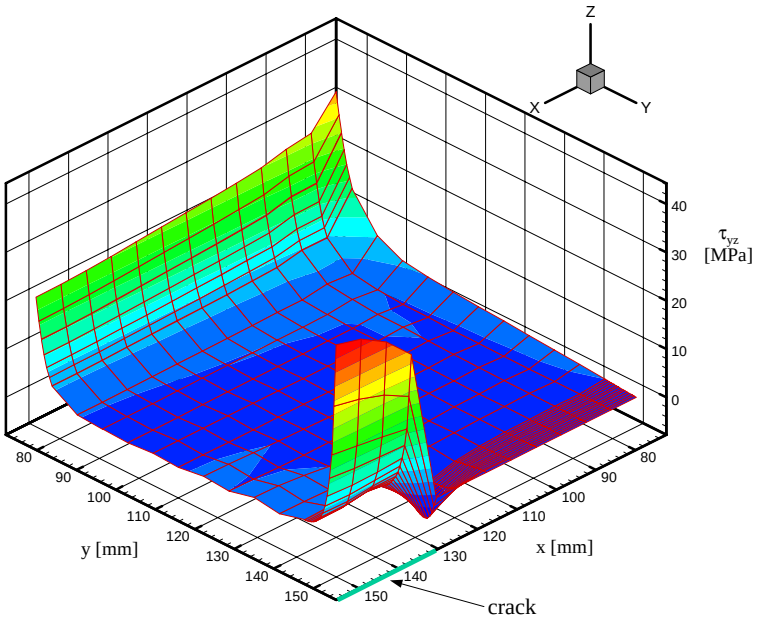

Figure 5.22. Shear stress (τ_{yz}) distribution in the midplane of the adhesive layer quarter of the crack-patch repair example.

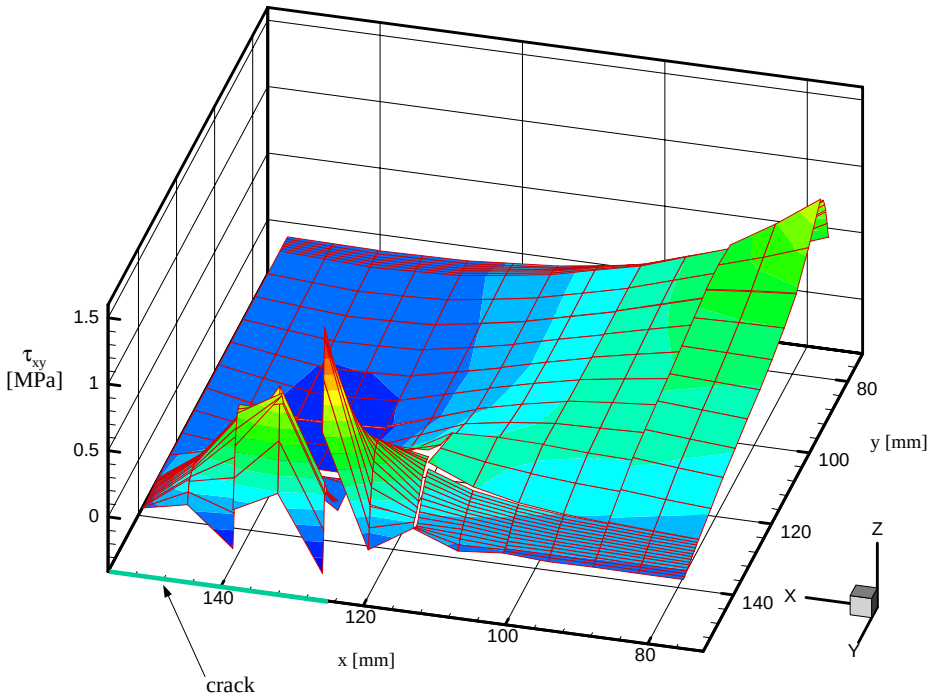

Figure 5.23. Shear stress (τ_{xy}) distribution in the midplane of the adhesive layer quarter of the crack-patch repair example.

The distributions of shear stresses τ_{xy} and τ_{yz} are shown in Figs. 5.23 and 5.24, respectively. Both cases show significant stress concentrations in the crack tip region.

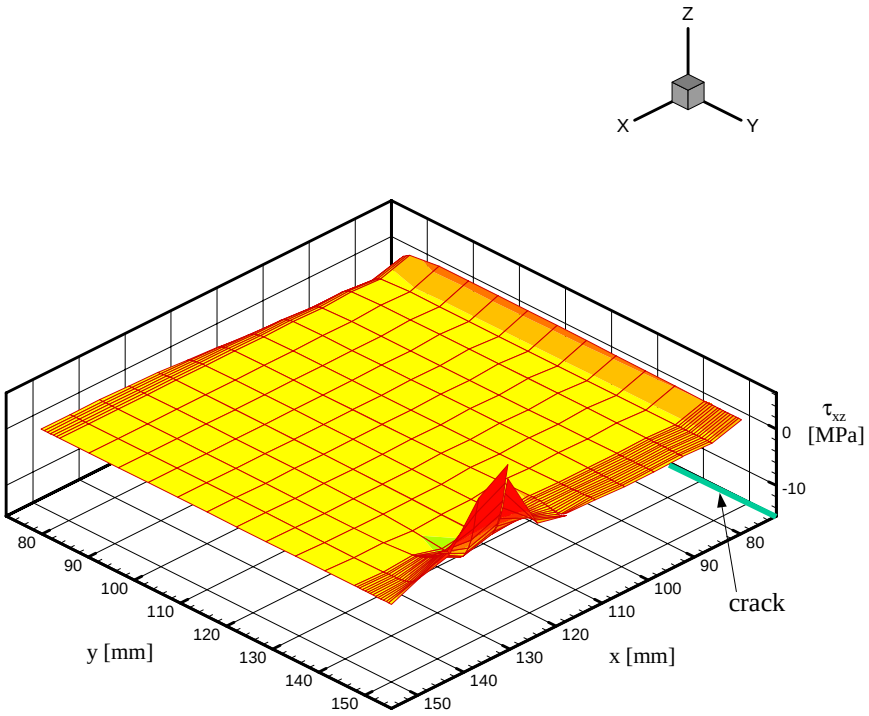

Figure 5.24. Shear stress (τ_{xz}) distribution in the midplane of the adhesive layer quarter of the crack-patch repair example.

Figures 5.25 and 5.26 show stress distributions in the direction of the loads (σ_{xx}) and perpendicular to them (σ_{zz}). These distributions are similar to those for the peel stress distribution but with smaller absolute values.

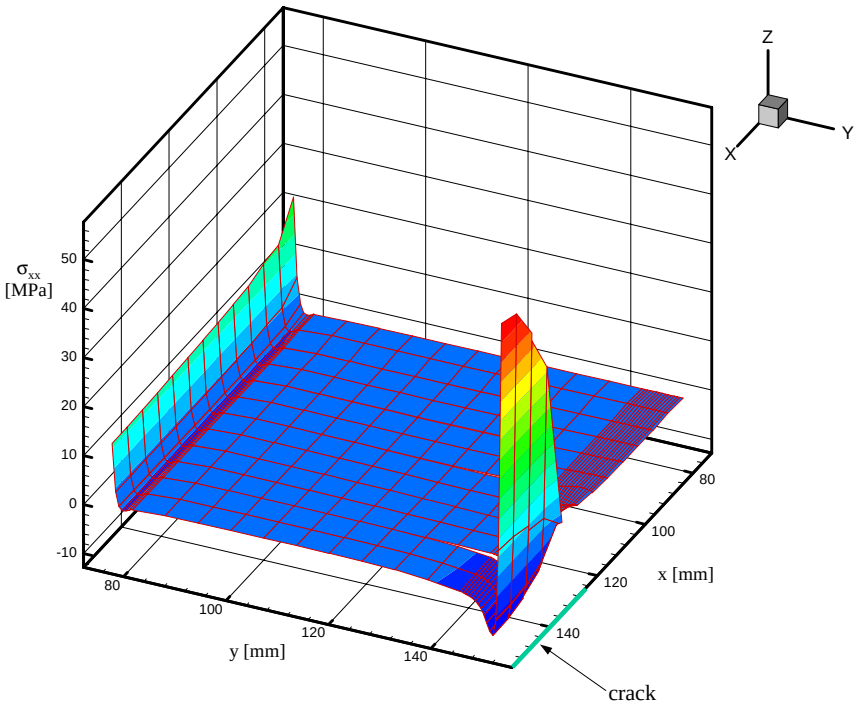

d

Figure 5.25. Axial stress (σ_{xx}) distribution in the midplane of the adhesive layer quarter of the crack-patch repair example.

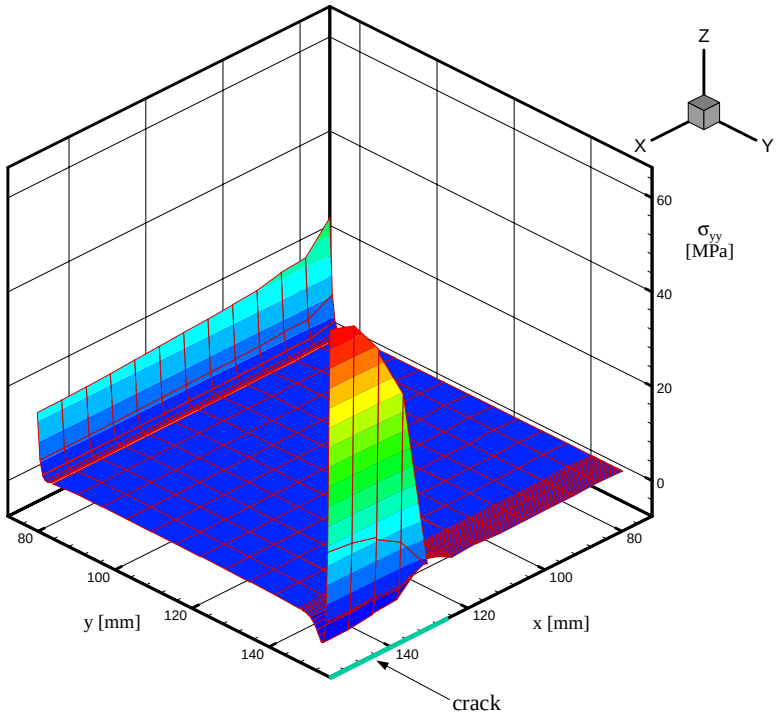

Figure 5.26. Axial (σ_{yy}) stress distribution in the midplane of the adhesive layer quarter of the crack-patch repair example.

Since peel stresses and shear stresses in the xz direction are larger than the other stress components, it is expected that damage will be initiated in the regions where both stresses have maximum values. Figures 5.25 and 5.26 show that these maximum values occur at the same region, near the crack tip.

5.5.3 Geometrically Nonlinear Single Lap Joint

Single lap joints are subjected to important geometrically nonlinear effects due to the eccentrically applied forces. The eccentricity of the two applied loads causes large rotations in the structure. In fact, single lap joints are highly nonlinear structures. For this reason, this geometry was selected to test the geometrically nonlinear features of the adhesive finite element, ADH3D.

A single lap joint studied by Tsai and Morton (1994a) was used as a test geometry. Tsai and Morton analyzed several single lap joint geometries. They divided them into short and long joints. Different thicknesses and material properties for the adhesive were used and results from nonlinear finite element analyses were compared with solutions from Goland and Reissner (1944). The typical single lap joint configuration of Tsai and Morton (1994) is shown in Fig 5.27.

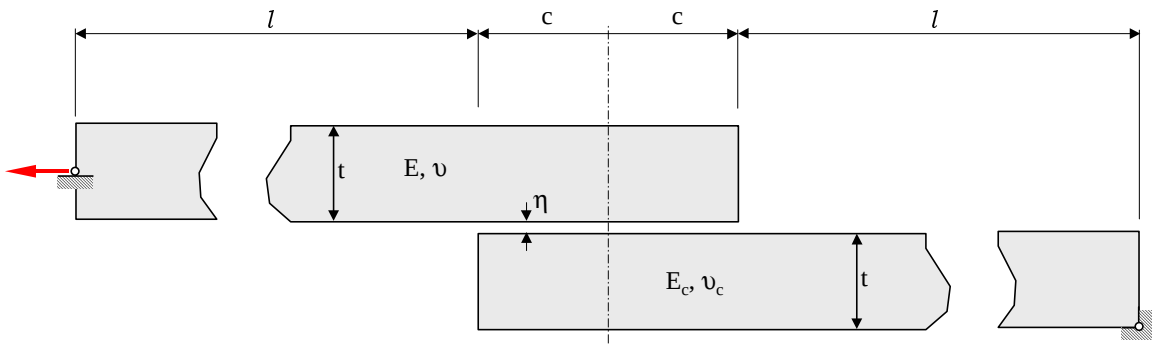

Figure 5.27. Single lap joint.

In this study, the short joint from Tsai and Morton's paper is modeled using the 3-D adhesive element. The geometric and material properties are: E = 70 Gpa, ν = 0.34, t =

1.6, and ν_c = 0.4. The following relations are verified in the specimen studied: l/c = 10, c/t = 4, ν/t = 0.078 and E_c/E = 0.008. These relations represent a short joint with a relatively flexible adhesive.

Tsai and Morton's (1994) analyses are based on plane-strain element models in ABAQUS and the Goland and Reissner expressions. Their results are compared to those from a finite element model using the ADH3D adhesive finite element. Fig. 5.28 shows the geometry modeled with ADH3D and Table 5.3 shows the geometric and material properties used. Young's modulus and the thickness of the adhesive are obtained applying the relations given in the previous paragraph.

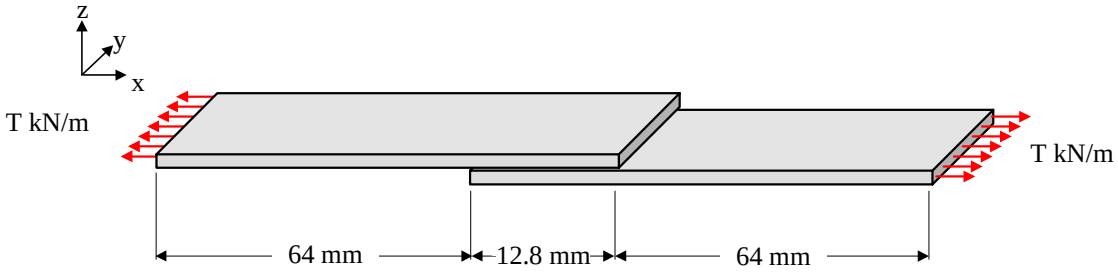

Figure 5.28. Three-dimensional single lap joint geometry modeled with ADH3D elements.

Table 5.3. Geometric and material properties for single lap joint.

Material	E (GPa)	ν	h (mm)
Adherend	70.0	0.34	1.6
Adhesive	0.56	0.40	0.125

The finite element model is composed of 350 nodes and 72 elements. The mesh is shown in Fig. 5.29.

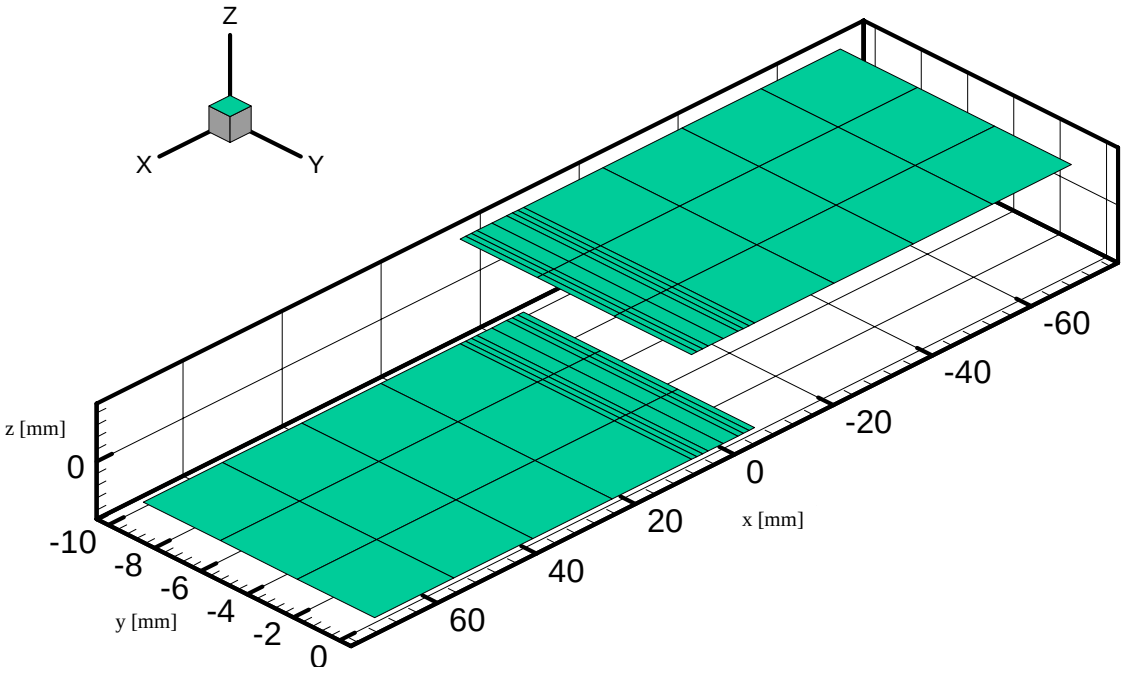

Figure 5.29. Finite element mesh of the three-dimensional single lap joint geometry modeled with ADH3D elements.

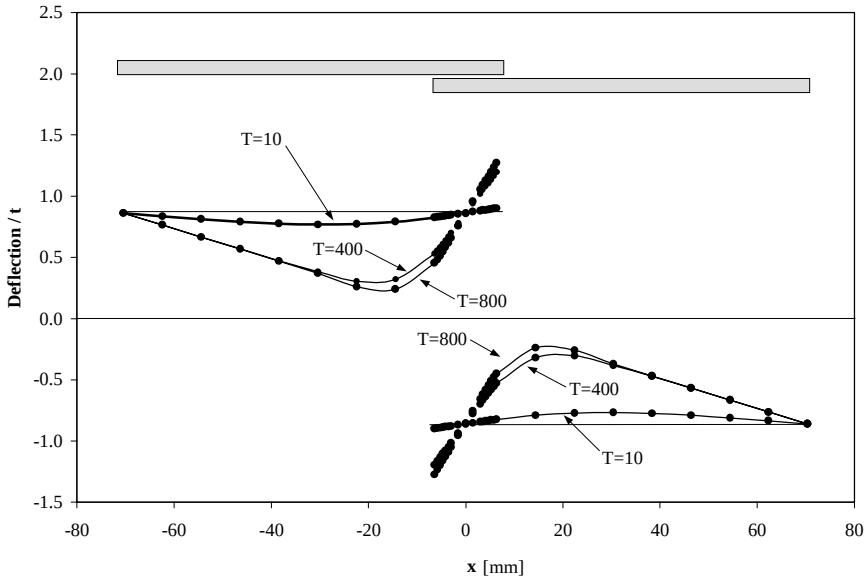

Figure 5.30. Deflections along the longitudinal direction of the three dimensional. single lap joint geometry modeled with ADH3D elements. Dimensions of T are [kN/m].

The finite element model specimen was subjected to three levels of T, the load per unit of width. Figure 5.30 shows deflections of the structure normalized relative to the thickness of the adherends for load levels T=10, T=400, and T=800 ($kN.m^{-1}$). As expected, deflections do not change significantly at high loads.

Normalized stress distributions σ_{xx}, $\sigma_{yy,}$ and τ_{xy} in the adhesive for a short joint with a flexible adhesive from Tsai and Morton (1994a) are shown in Figs. 5.31, 5.32, and 5.33 for the same three loads.

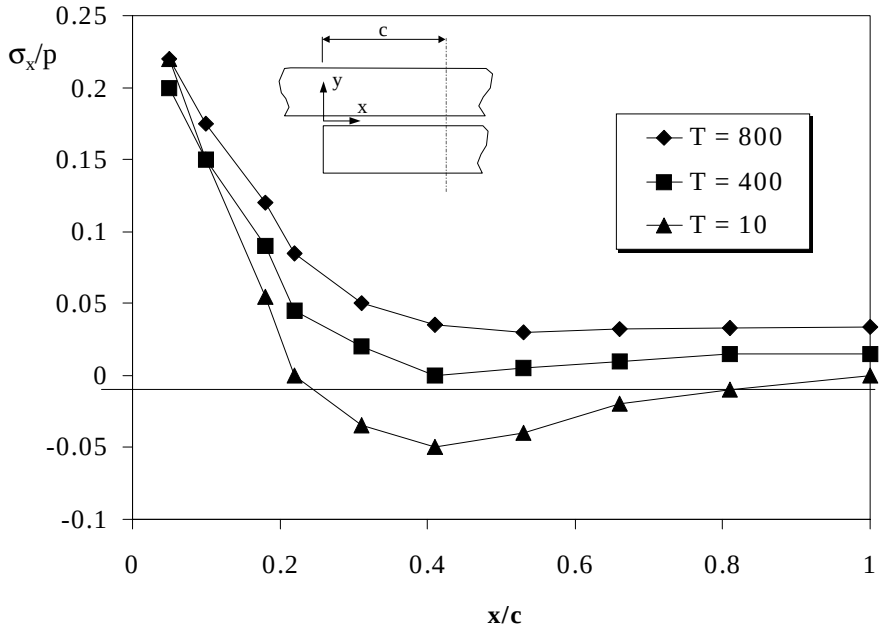

Figure 5.31. Adhesive axial stress (σ_x) distribution along the longitudinal direction of the two-dimensional single lap joint geometry modeled by Tsai and Morton (1994a). Dimensions of T are [kN/m].

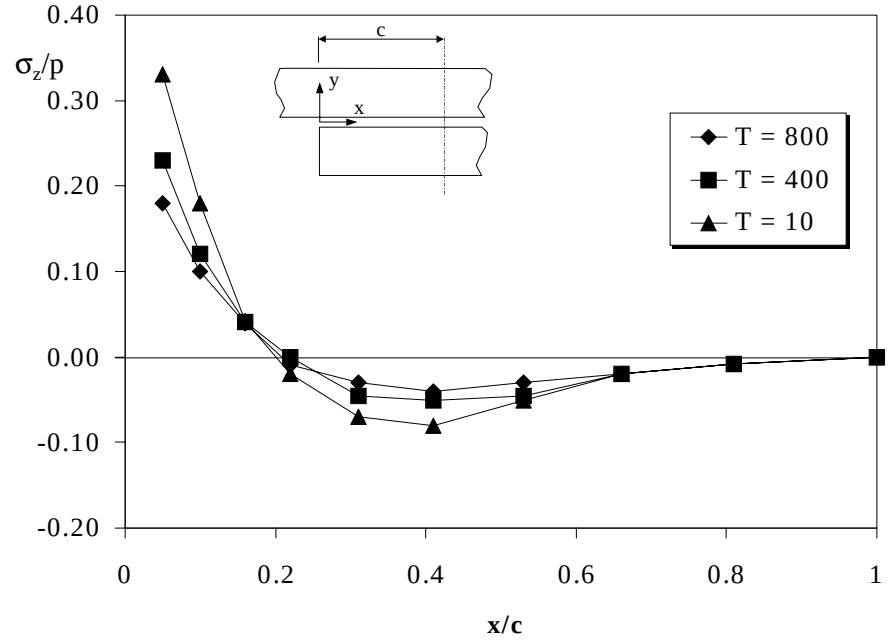

Figure 5.32. Adhesive peel stress (σ_z) distribution along the longitudinal direction of the two-dimensional single lap joint geometry modeled by Tsai and Morton (1994a). Dimensions of T are [kN/m].

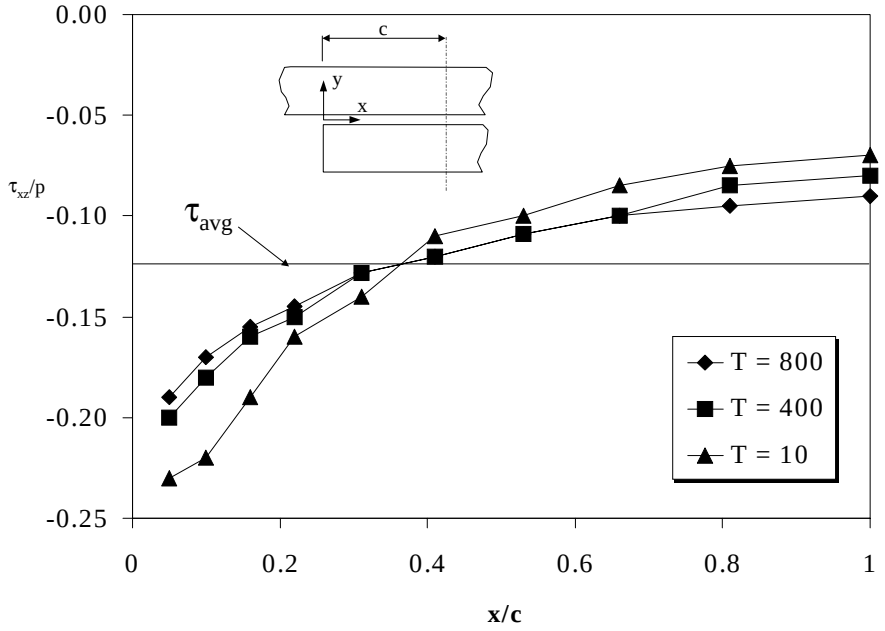

Figure 5.33 Adhesive shear stress (τ_{xz}) distribution along the longitudinal direction of the two-dimensional single lap joint geometry modeled by Tsai and Morton (1994a). Dimensions of T are [kN/m].

Stresses are normalized with respect to p, which is the load T multiplied by the adherends' thickness, t. Thus

$$p = Tt$$

Figures 5.34, 535, and 5.36 show the stress distributions obtained from the ADH3D model. These distributions correspond to the stresses in the midplane of the adhesive layer at the center of the specimen in the plane of symmetry. This is because the two-dimensional analysis made by Tsai and Morton (1994a) considered the plane strain behavior which approximates better to the conditions at the mentioned place. Figures 5.37 and 5.38 shows comparisons between peel and shear stresses from Tsai and Morton (1994a) and the adhesive finite element model respectively. There is a good agreement between the results from both approaches.

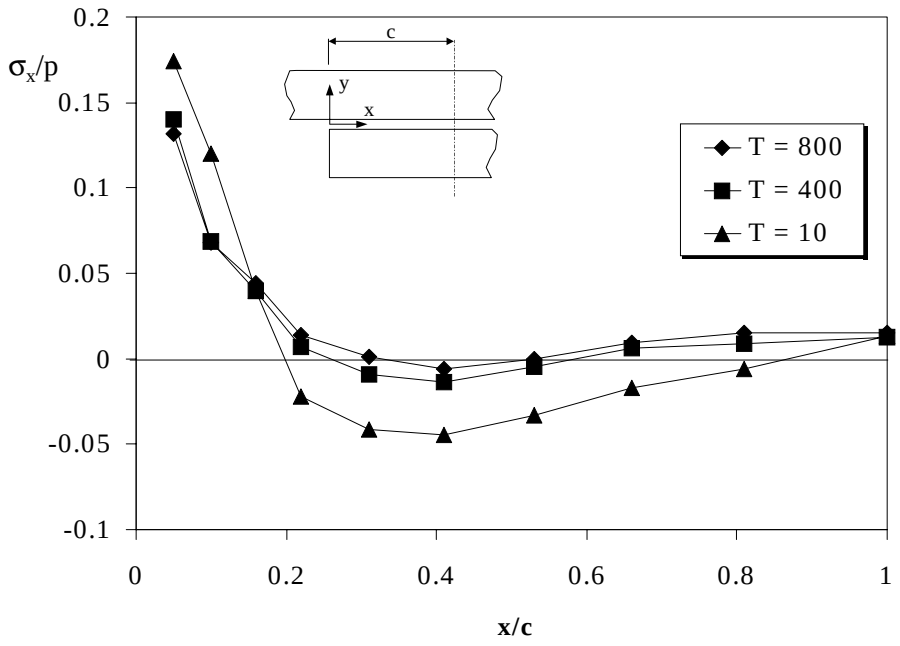

Figure 5.34. Adhesive axial stress (σ_x) distribution along the longitudinal direction of the three-dimensional single lap joint geometry modeled with ADH3D elements. Dimensions of T are [kN/m]and p

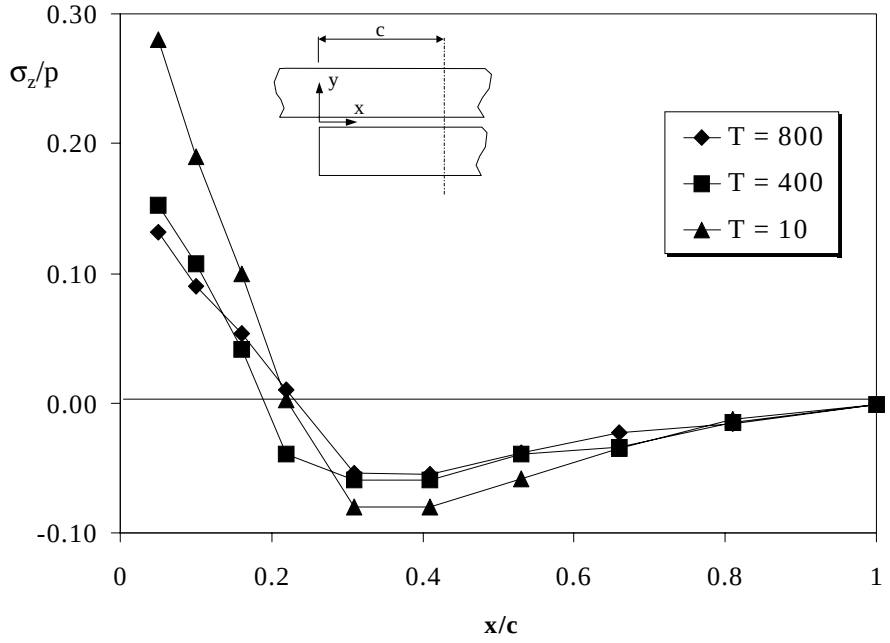

Figure 5.35. Adhesive peel stress (σ_z) distribution along the longitudinal direction of the three-dimensional single lap joint geometry modeled with ADH3D elements. Dimensions of T are [kN/m].

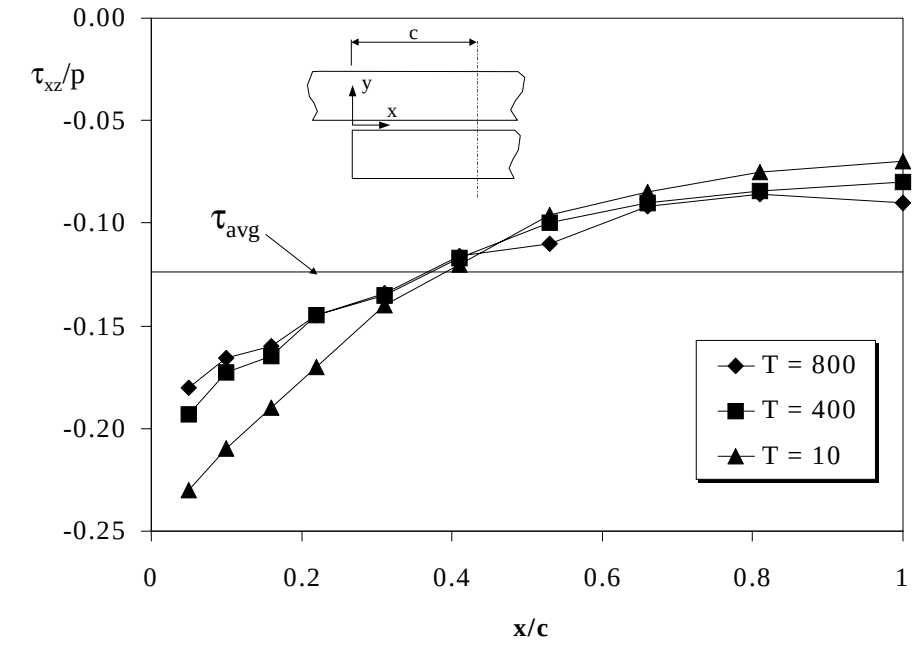

Figure 5.36. Adhesive shear stress (τ_{xz}) distribution along the longitudinal direction of the three-dimensional single lap joint geometry modeled with ADH3D elements. Dimensions of T are [kN/m].

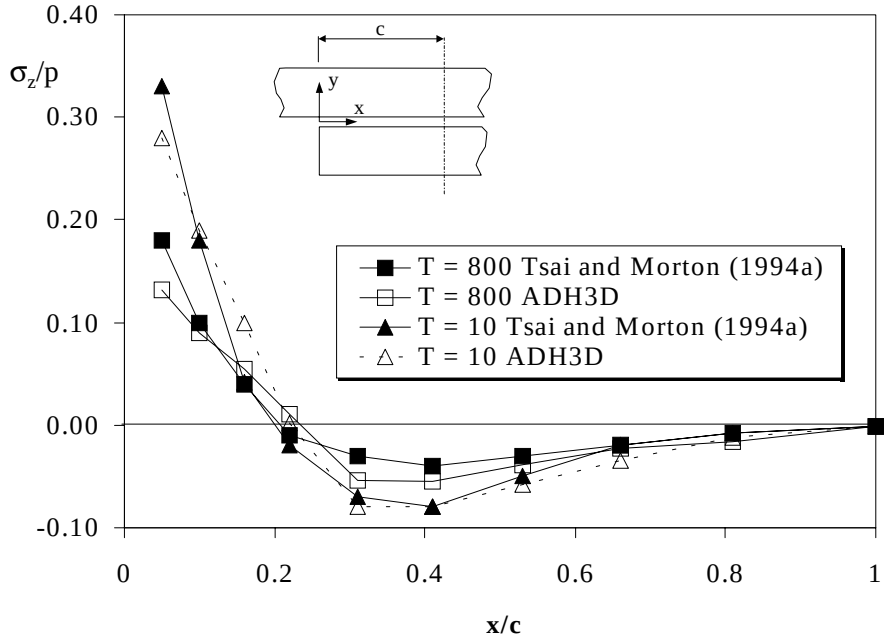

Figure 5.37. Comparison between adhesive peel stress (σ_z) distribution along the longitudinal direction of the three-dimensional single lap joint geometry modeled with ADH3D elements and from Tsai and Morton (1994a). Dimensions of T are [kN/m].

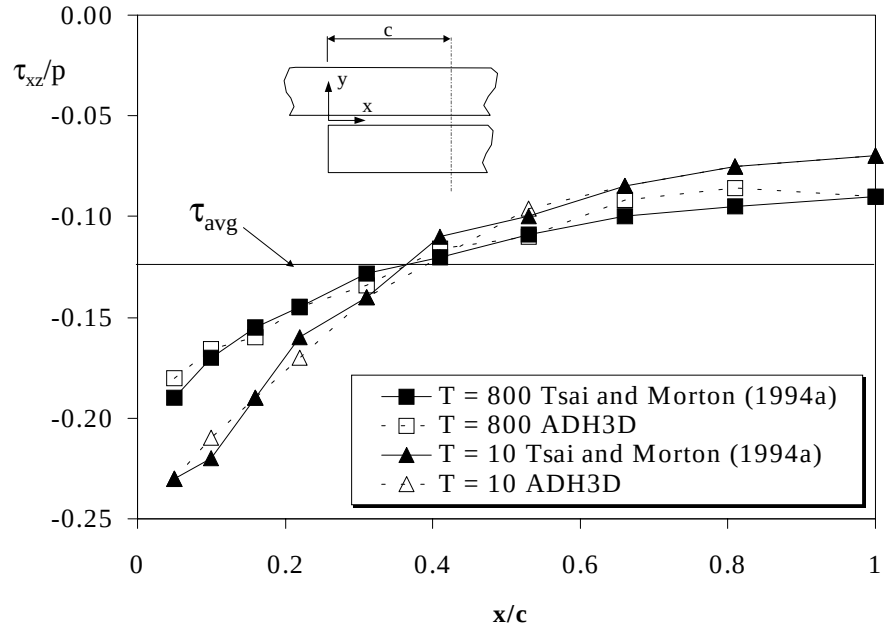

Figure 5.38. Comparison between the adhesive shear stress (τ_{xz}) distributions along the longitudinal direction of the of the three-dimensional single lap joint geometry modeled with ADH3D elements and from Tsai and Morton (1994a). Dimensions of T are [kN/m].

5.6 Conclusions

A new ADH3D adhesive finite element model which uses shell elements to model the adhesive layer was formulated and implemented in a computer program. This element satisfies C^0 displacement continuity and continuity between the adhesive layer and the adherends.

The element formulation includes geometrical nonlinearities and thermal and moisture effects. Strength of material stress distributions for three-dimensional joint configurations are obtained with this element.

Single lap joint and crack patch geometries were studied and results were discussed and compared with other solutions. Geometrically nonlinear behavior was studied and compared with previous results from the literature.

Chapter 6

Analysis of Fatigue-Crack Growth in Adhesively Bonded Joints

6.1 Introduction

The advantages of adhesive joints and the efficiency of adhesively bonded composite patches to increase the durability of damaged structures are demonstrated in the literature (Baker 1988). However, debonds can occur as a consequence of many factors such as flaws during the bonding process or cracks during the service life. Debonds reduce the efficiency of joints and composite patches and may lead to failure.

Studies dealing with debond in adhesively bonded patches include the work by Naboulsi and Mall (1996). They used shell finite elements to model a cracked plate, a composite patch, and adhesive components of a cracked-patch repair geometry. Their analyses of double- and single-sided patches showed good agreement with analytical expressions. Naboulsi and Mall (1997) investigated thermal effects on cracked aluminum panels repaired with adhesively bonded patches. Ratwani (1979) and Sun et al. (1996) studied bonded composite patch repair of cracked metallic structures under isothermal mechanical loads. They analyzed redistribution of stresses and computed stress intensity factors for the patched structure.

In this chapter, an analytical method for durability analysis of adhesively bonded patch repair of cracked structures is presented. Specifically, fatigue life expectancy of the patch is computed as the number of cycles needed to cause a predefined debond area to reach the patch's edge. Once this situation is reached, the patch is no longer effective and the structure behaves as if it were unpatched. A power-law fatigue crack growth relationship is used to compute debond area extensions. This fatigue law requires fracture

mechanics parameters such as the strain energy release rate. These parameters are computed with the three-dimensional adhesive finite element model presented earlier in this work.

The analytical procedure includes the following steps:

1. Determine the load characteristics.
2. Compute meaningful parameters to characterize the crack.
3. Assume a crack growth law.
4. Determine the crack extensions.
5. Modify the model to account for the new crack position.

The objectives of this chapter are: (1) to demonstrate that the finite element model of adhesively bonded joints can be applied to analyze situations such as the debond process of a crack-patch repair geometry; (2) to show that the adhesive finite element model gives reasonably accurate results with a relatively small number of elements and nodes.

6.2 Determination of Load Characteristics

Structures can be subjected to a variety of actions. The determination of the characteristics of the loads that act on a structure is one of the most important tasks of the engineer. The fatigue failure mechanism involves cyclic loads. This kind of load has two important characteristics: frequency and amplitude (Fig. 6. 1).

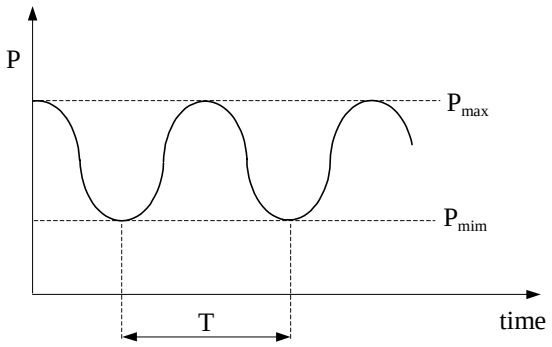

Figure 6.1. Constant amplitude and frequency cyclic load.

where P_{max} - P_{min} is the amplitude and Δt^{-1} is the cyclic frequency. Actual loads have a more irregular pattern than the simple case shown in Fig. 6.1, with a range of frequencies and local peak values of the amplitude. However, in the present work, constant frequency and amplitude are used.

6.3 Fracture Mechanics Parameters

Linear fracture mechanics has been widely used to study the fatigue behavior of adhesively bonded joints. Kinloch and Osiyemi (1993) showed that the rate of crack growth in a double-cantilever beam is a function of the maximum strain energy release rate. Therefore, strain energy release rates are used in this work as a fracture mechanics parameter to predict the lifetime of adhesive joints.

A large number of methods to compute strain energy release rates can be found in the literature. They are divided by Badari Narayana et al. (1994) into the following groups: (i) virtual crack extension (Park, 1974; Hellen, 1975); (ii) crack opening displacement (Chan et al. 1970); (iii) the nodal force method using singular elements; (iv) direct estimation of stress intensity factors with hybrid elements; and (v) the J-integral using Eshelvi's energy momentum. Most of these methods require a good representation of the singularity around the crack front. This is achieved by using very fine meshes in the crack tip region.

A different approach to calculate stress intensity factors and strain energy release rates using only forces and displacements from a standard finite element was proposed in the late 70's. It is based on Irwin's concept of the crack closure integral which states that strain energy release rates can be calculated by considering an incremental crack extension and evaluating the work needed to close the crack. This estimation requires the computation of the work done from the finite element analyses of two configurations.

Kanninen and Rybicki (1977) proposed a procedure to compute strain energy release rates following Irwin's integral concept from one finite element analysis by combining the forces and displacements of the elements forming the crack tip. The procedure is known as the modified crack closure integral method, and the expressions they obtained are valid only for two-dimensional four-node quadrilateral elements.

Shivakumar et al. (1988) extended the Kanninnen and Rybicky method to three-dimensional configurations. They obtained expressions of strain energy release rates for 8- and 20-node brick elements. Badari and Narayana et al. (1994) used the modified crack closure integral method to compute strain energy release rates for 8-node brick elements; they introduced the concept of sub-area integration to estimate values at various points inside the element.

In this work the modified crack closure integral method is used to compute strain energy release rate parameters along the crack front. This method gives accurate results even without exact stress field representation and with relatively coarse meshes (Shivakumar et al. 1988). This significantly reduces the number of degrees of freedom needed to obtain accurate results.

The expression of total strain energy release rate, G_T, when the crack front extends an infinitesimal area ΔA is

$$G_T = \lim_{\Delta A \to 0} (\Delta U / \Delta A) \tag{6.1}$$

where ΔU is the change in the strain energy. Figure 6.2 shows the geometry, coordinate system, and notation used for an arbitrary crack inside a three-dimensional body. A local coordinate system, r and s, is defined in the plane of the crack. The local coordinate axis s is perpendicular to the crack front path.

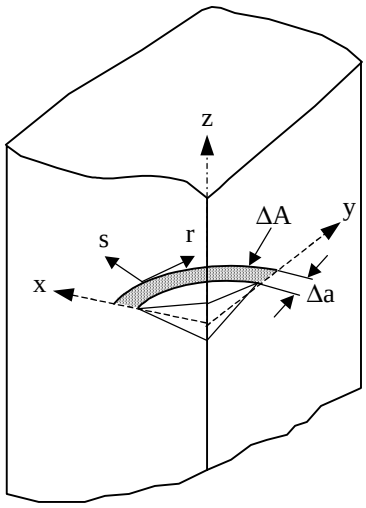

Figure 6.2. Crack in a three-dimensional body, coordinate system and notation.

Figure 6.3 shows the finite element mesh in the crack plane.

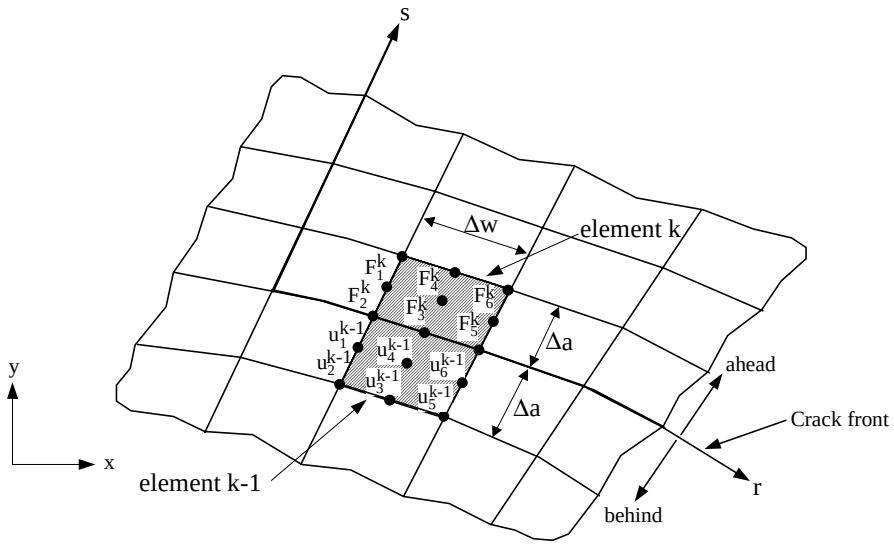

Figure 6.3. Finite element mesh in the crack plane at the crack front.

Considering the k^{th} element and a sufficiently small Δa, the strain energy release rate for the opening mode I is

$$G_I = \lim_{\Delta A_k \to 0} \frac{1}{\Delta A_k} \int_{\Delta A_k} \sigma_z u_z \, dr ds \tag{6.2}$$

where

σ_z = peel stress in element i

u_z = displacement of element j in the z direction

ΔA_k = differential area of element k

r and s = local coordinates

The stress σ_z in the element can be expressed as

$$\sigma_z = b_0 + b_1\xi + b_2\eta + b_3\zeta + \cdots + b_{18}\zeta^2 \tag{6.4}$$

where ξ, η, and ζ are the element coordinates, and b_0, b_2, … b_{18} are constants to be determined from the equivalent forces F_{zj} using the relation

$$F_{zj} = \iiint_{V_e} N_j^T \sigma_z |J| d\xi d\eta d\zeta \tag{6.5}$$

The interpolation functions N_j are taken from Taylor (1996). V_e is the volume of the element, and $|J|$ is the determinant of the Jacobian matrix. Equation 6.5 yields a system of 18 equations from which can be set which the coefficients b_I are computed.

The displacement u_z can also be expressed as

$$u_z = a_0 + a_1\xi + a_2\eta + a_3\zeta + \cdots + a_{18}\zeta^2 \tag{6.6}$$

Again, a_0, a_2, … a_{18} are constants to be determined. They can be calculated using the nodal displacements as follows:

$$\begin{Bmatrix} u_{z1} \\ u_{z2} \\ \vdots \\ u_{z18} \end{Bmatrix} = \begin{bmatrix} 1 & 1 & \cdots & 1 \\ 1 & 1 & \cdots & -1 \\ \vdots & \vdots & \vdots & \vdots \\ 1 & -1 & \cdots & -1 \end{bmatrix} \begin{Bmatrix} a_0 \\ a_1 \\ \vdots \\ a_{18} \end{Bmatrix} \tag{6.7}$$

Therefore, Eqs. 6.4 and 6.6 give stresses and displacements expressed as functions of the local coordinates ξ, η and ζ,. Substituting Eqs. 6.4 and 6.6 into Eq. 6.2, G_I is obtained. Strain energy release rate values for opening modes II and III are obtained following the same procedure. Adding the values of $G_{I,}$ $G_{II,}$ and G_{III} we obtain the total strain energy release rate, $G_{T.}$

If the sides of the element are straight lines, Eq. 6.2 becomes

$$G_I = \frac{1}{2\Delta w_k} \sum_i^6 F_i^k u_i^{K+1} \tag{6.7}$$

In other words, the strain energy release rate is the product of the nodal forces ahead of the crack front and the displacement behind the crack front (Fig. 6.4).

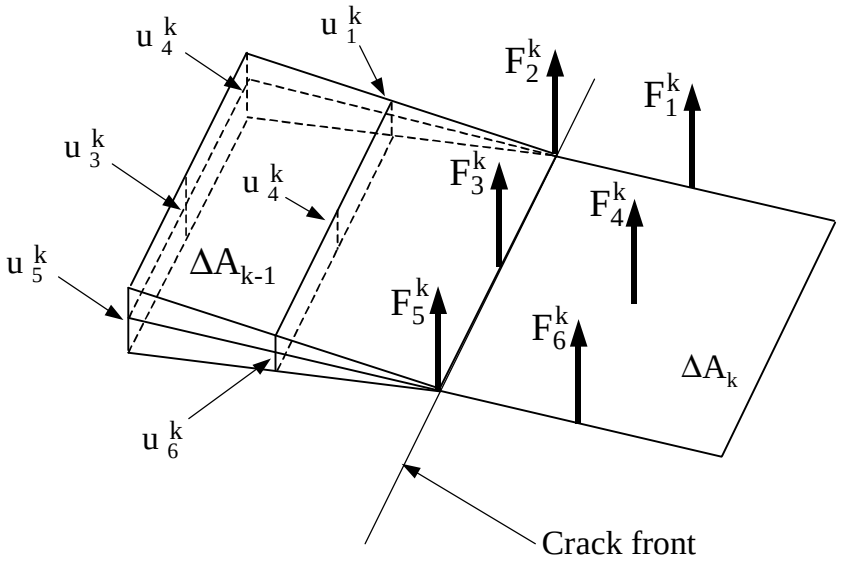

Figure 6.4. Nodal displacements and forces in the adhesive element.

Nodal forces in the above expressions are extracted by multiplying the element stiffness matrix with the nodal displacements:

$$\{F_i^k\} = [K_k]\{u_i^k\} \tag{6.8}$$

where $\{F_i^k\}$ are the nodal forces, $[K_k]$ is the stiffness matrix of the k^{th} element, and $\{u_i^k\}$ are the nodal displacements.

6.4 Fatigue-Crack-Growth Law

As stated in Chapter 2, several crack growth rate laws have been formulated. Some of them relate crack growth rate to the stress intensity factor range, while others add the influence of the mean stresses, threshold, and maximum values of the stress intensity factor. All of these relations refer to stress intensity factors for mode I. However, the flexibility of the finite element method to analyze arbitrary structures requires a mixed mode failure mechanism as a crack growth rate law. Lin and Liechti (1987) gave correlations between the logarithms of crack growth rates, log(da/dN), and logarithms of energy release rates ranges, log(ΔG). They showed that the relation between these two parameters follows a power law similar to the Paris-Erdogan law for most of the cases. Kinloch and Osiyemi (1993) used a form of the Paris equation to relate total strain energy release rate with crack growth rate. A simplified version is commonly used:

$$\frac{da}{dN} = D\Delta G^n \tag{6.9}$$

where

D and n = material dependent constants

ΔG = range of strain energy release rate

da = differential crack extension

dN = differential number of load cycles

The strain energy release range is defined as follows:

$$\Delta G = G_{max} - G_{min} \tag{6.10}$$

where G_{max} and G_{min} are the strain energy release rates for P_{max} and P_{min}, repectively.

6.5 Determination of Crack Extensions

To compute the crack extension for a certain number of load cycles, the crack growth curve, Eq. 6. 9, is integrated:

$$\Delta N = \int_{a_1}^{a_2} \frac{1}{D\Delta G^n} da \tag{6.11}$$

Equation 6.11 gives the number of cycles needed to extend the crack from the initial crack length, a_1, to the final crack length, a_f. Since G is assumed constant during that crack extension, Eq. 6.11 becomes

$$\Delta N = \frac{1}{DG^n}\left(a_2 - a_1\right) = \frac{1}{DG^n}\Delta a \tag{6.12}$$

Crack extensions can be computed using the above procedure and a new debond areas is defined. If the procedure is continued, a prediction of the debond process is obtained.

6.6 Algorithm to Simulate Debonding

In this section an algorithm capable of handle the debonding process of a crack-patch repair geometry is implemented. This geometry was selected for the simulation because it is of interest to the industry. Debond of the patch produces changes in the stress distributions across the bonded areas.

A predefined elliptical debond area is considered in this example to facilitate mesh generation and debond area extensions. However, the procedure is general and can be applied to any arbitrary debond region.

The procedure consists of the following steps:

1. Define the initial configuration and loads; this step includes definition of the initial geometry with a predefined debond area.
2. Perform a finite element analysis for the initial configuration; the three-dimensional adhesive finite element model is used.
3. Compute the strain energy release rate along the debond line; the modified crack closure integral method is used to compute strain energy release rates along the crack front or debond.
4. Calculate debond extensions for each node; by integrating the crack-growth power law, crack or debond area extensions are calculated for each node along the debond line.
5. Redefine the geometry to account for debond region extensions; a FORTRAN computer program computes the new nodal coordinates for the elements in the vicinity of the debond line; elements outside the vicinity of the debond line are not modified.
6. Perform a new finite element analysis for the updated configuration; standard finite element analysis of the new geometry including the enlarged debonded region is performed.

The procedure is repeated until a failure condition is reached. The failure condition is a user determined parameter which can be defined as a maximum number of load cycles or when the debond area reaches the edge of the patch. Figure 6.8 shows a flow chart of the procedure described above.

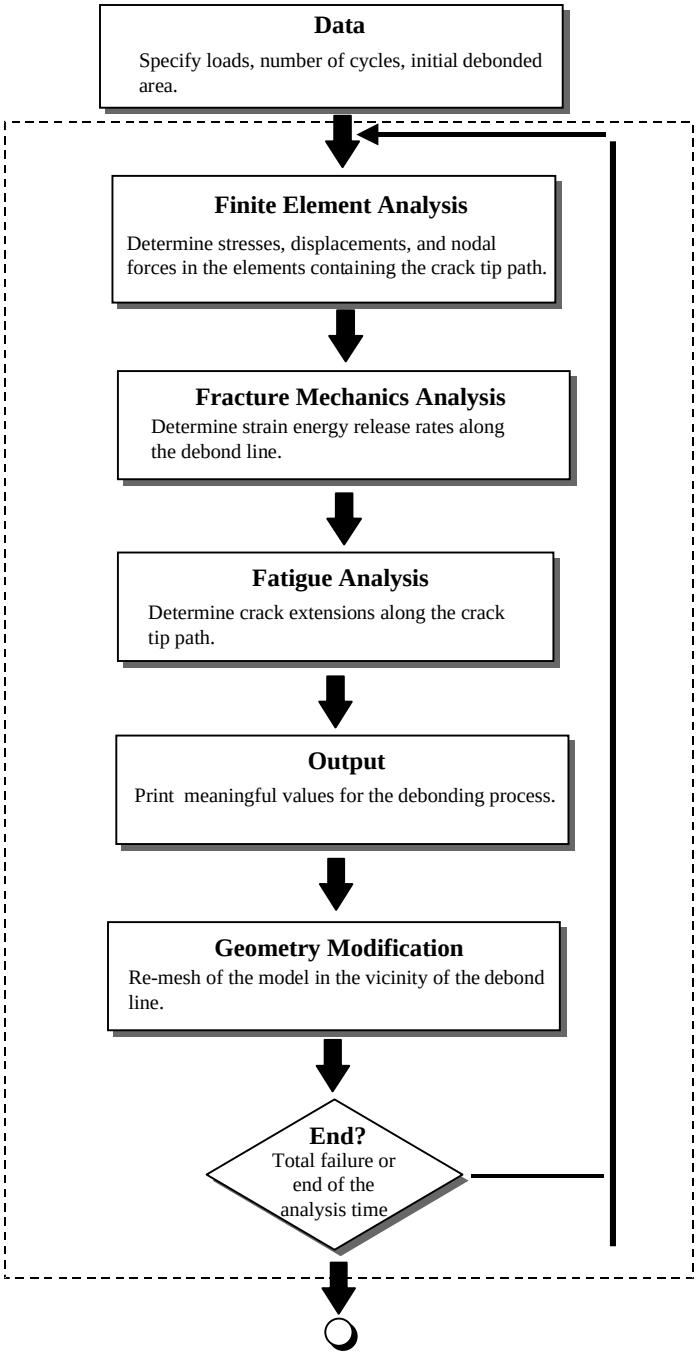

Figure 6.5. Flow chart of the debond process algorithm.

6.7 Examples

Two examples are presented in this section: the analysis of the strain energy release rate in a crack lap shear configuration, and the numerical simulation of the debonding process in a crack-patch repair geometry. The objective of the first one is to test the three-dimensional modified crack closure integral method proposed to obtain fracture mechanics parameters along the crack front. The objective of the second example is to test the proposed algorithm in a three-dimensional scenario which is frequently found in industrial applications.

6.7.1 Crack Lap Shear geometry

This geometry was already analyzed in chapter 3 using the two-dimensional version of the adhesive finite element model (Fig. 3.13). It corresponds to Johnson's round-robin study (1987) of equal thickness adherend specimens with debond length 101 mm.

The adhesive thickness is 0.13 mm and the width for the adhesive and adherends is 25.4 mm. The material properties are 72.45 GPa and 1.932 GPa for the Young's moduli, and 0.33 and 0.4 for the Poisson's ratios of adherend and adhesive, respectively. The applied load is 11,120 kN.

The finite element model consists of 850 nodes and 300 elements. Figure 6.6 shows a displaced finite element model of the specimen. The mesh in the crack tip region is finer than in the rest of the structure because small elements are required to compute fracture mechanics parameters.

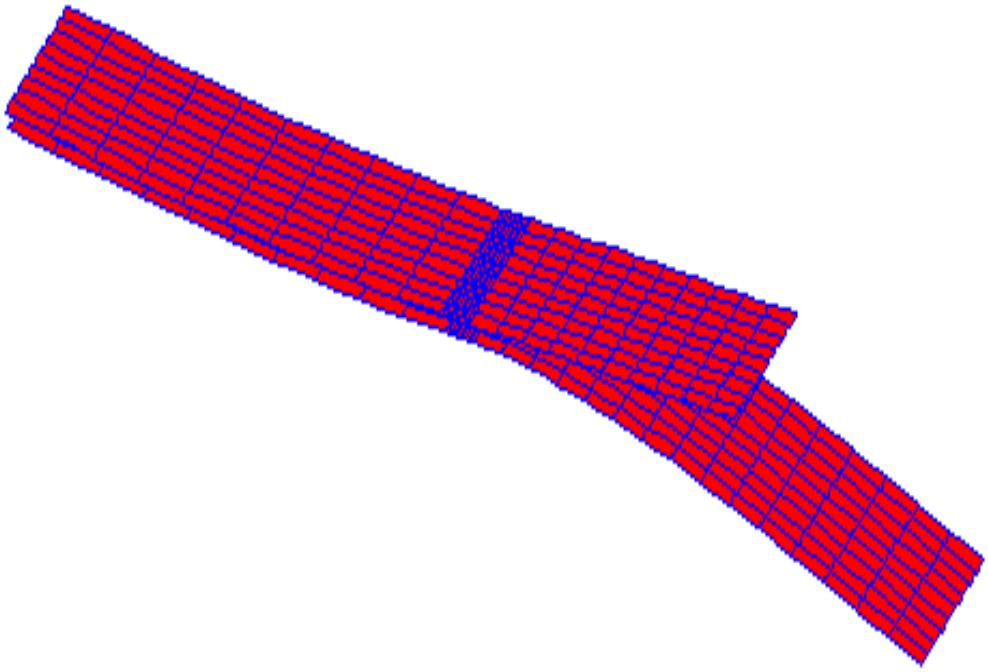

Figure 6.6. Displaced finite element model of the cracked lap shear specimen

Values of total strain energy release rates for modes I, II, and II along a straight crack tip path are presented in Fig. 6.7.

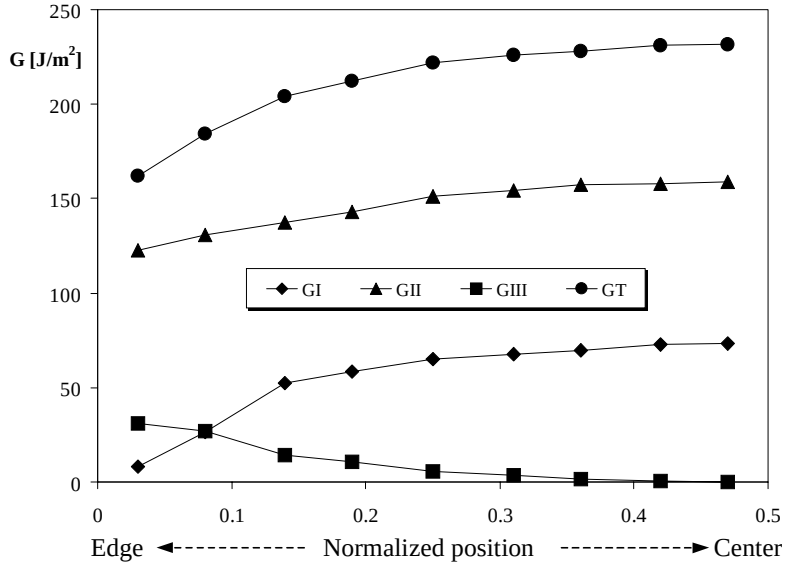

Figure 6.7. Strain energy release rates along the crack tip path.

Figure 6.7 shows good performance of the three-dimensional adhesive finite element to represent the variation of the strain energy release rate along the thickness of the specimen. G_I and G_{II} assume maximum values at the center of the specimen and they decrease towards the edges. This is because the conditions at the center of the specimen are closer to the plane strain condition in a two-dimensional analysis. On the other hand, G_{III} decreases towards the center of the specimen and is almost zero at the center. G_{III} is theoretically negligible in a crack lap shear specimen, and the small value of G_{III} is caused by Poisson effects, which produce differences of displacements from one point to the other in the direction of the specimen's thickness. G_T follows a behavior similar to G_I and G_{II}; in other words, it decreases towards the edges and has a maximum value at the center of the specimen.

In all cases, values obtained for G_I, G_{II}, and G_T are comparable to those summarized in Johnson's (1987) ASTM round-robin study of the CLS specimen which reports results from a number of researchers. Different approaches were used, and considerable variation in the results was found. Figure 6.8 shows total energy release rates for the 101 mm long debond specimen from each researcher. Results from two-dimensional and three-dimensional adhesive finite element models are also included in Fig. 6.9. There is a very good agreement among the results obtained from the two- and three-dimensional adhesive finite element models and the other approaches used. Values of the three-dimensional adhesive model are higher than those of two-dimensional analyses, but they are very close to the three-dimensional analysis by Lof (Johnson 1987). This is due, in part, to the fact that plane stress conditions were assumed for the two-dimensional analyses.

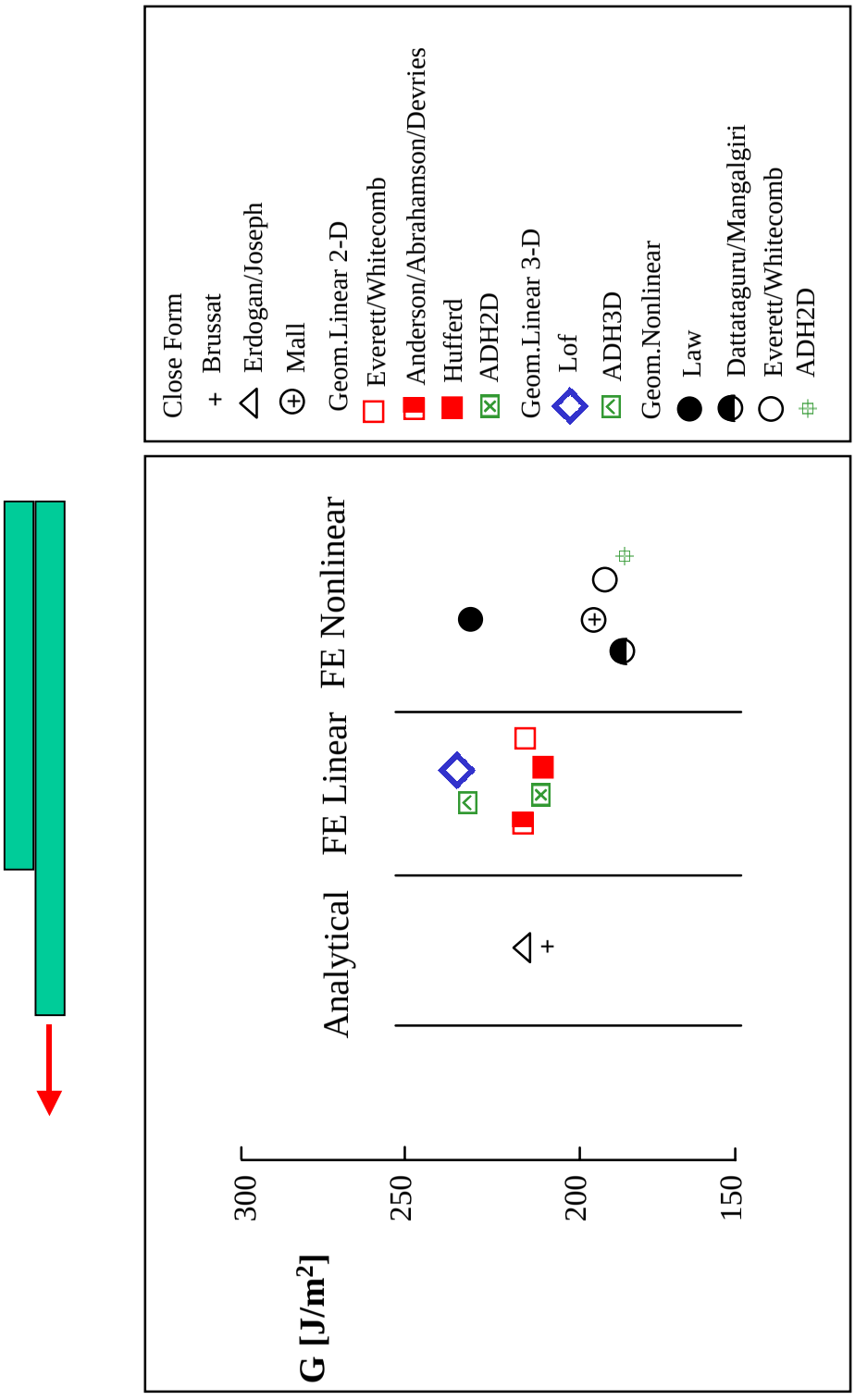

Figure 6.8. Total strain energy release rate results of ASTM round-robin crack lap shear 101 mm debond length specimen, including new results from ADH2D and ADH3D approach.

6.7.2 Crack-Patch Repair Geometry

A crack-patch repair geometry with an initial elliptical debond is analyzed using the ADH3D adhesive finite element model (Fig. 6.9). This geometry was studied by Naboulsy and Mall (1996). The algorithm developed to simulate the debonding of the patch is applied to this geometry. Figure 6.11 shows the geometry and dimensions of half of the specimen.

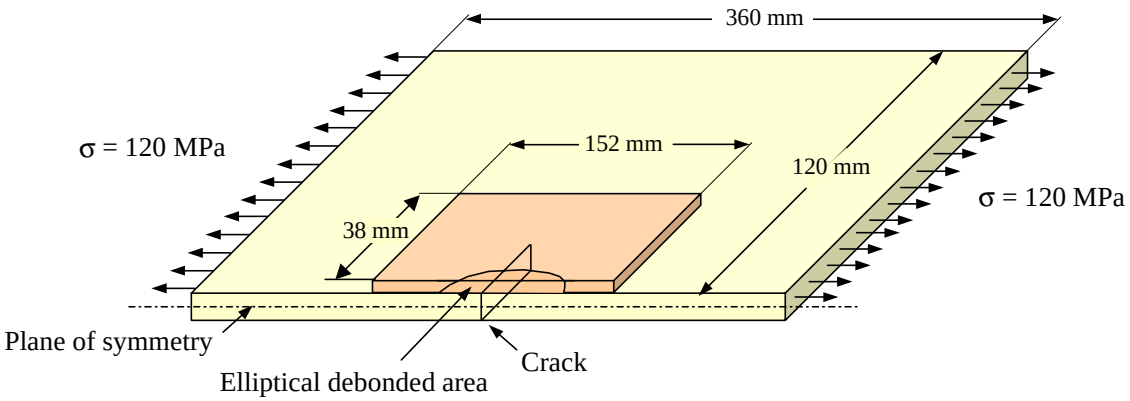

Figure 6.9. Crack-patch repair geometry.

The aluminum plate has a center crack with a length of 50 mm. The elliptical debond has a semi-major axis of 50 mm and a semi-minor axis of 20 mm (Fig 6.10).

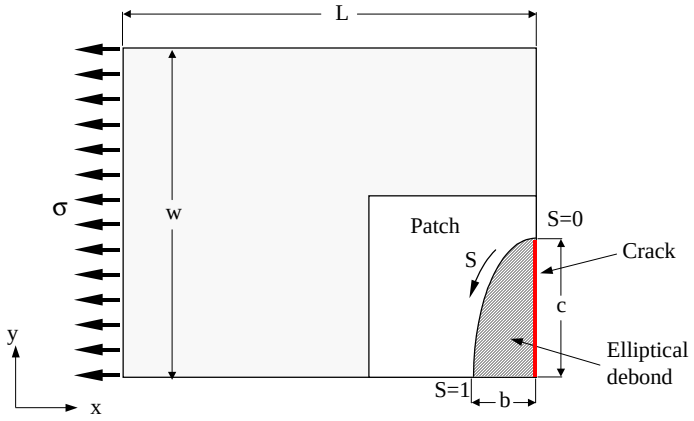

Figure 6.10. Quarter of the crack-patch repair geometry with elliptical debond.

The arc length, S, defines the position of a point along the crack front. The patch is made of boron/epoxy, and it is glued to the shell by an epoxy adhesive. Material properties are presented in Table 6.1.

Table 6.1 Material properties for the crack-patch repair geometry.

Material	E (GPa)	ν	h (mm)
Aluminum	71.7	0.3	2.29
Patch	E_1= 208 E_2= 25.4 E_3= 25.4	ν_{12} = 0.16 ν_{23} = 0.035 ν_{13} = 0.16	0.762
Adhesive	2.34	0.32	0.1061

The finite element mesh of a quarter of the structure, with 1308 nodes and 290 elements, is shown in Fig 6.11.

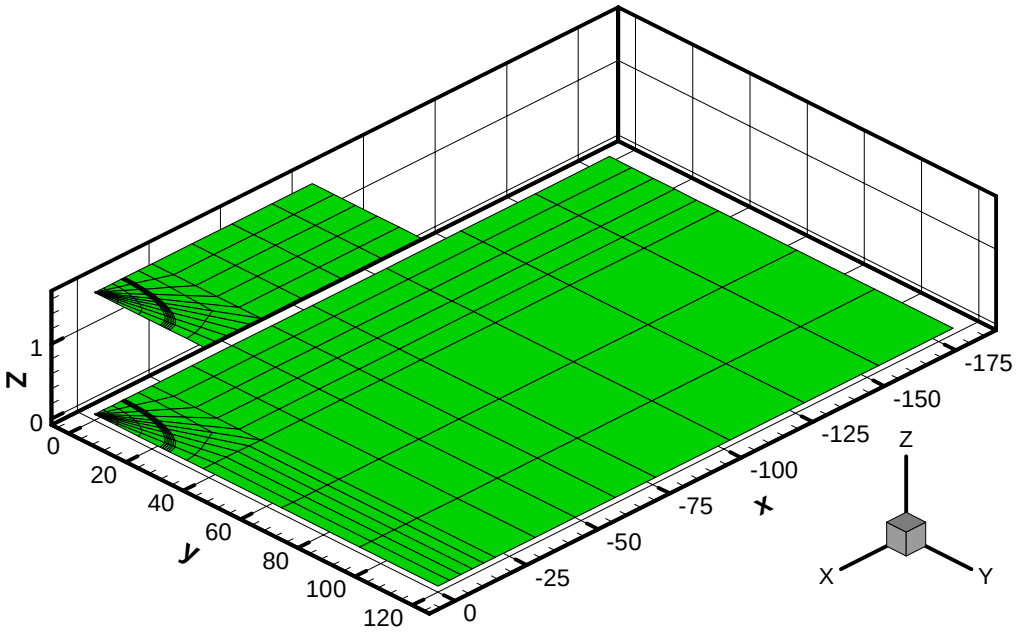

Figure 6.11. Finite element model of a quarter of the crack-patch repair geometry with elliptical debond.

The elliptical debond was modeled using straight-side elements. A FORTRAN computer program was written to generate the mesh in the debond area. Figure 6.12 shows an amplified view of the finite element model of the debond area.

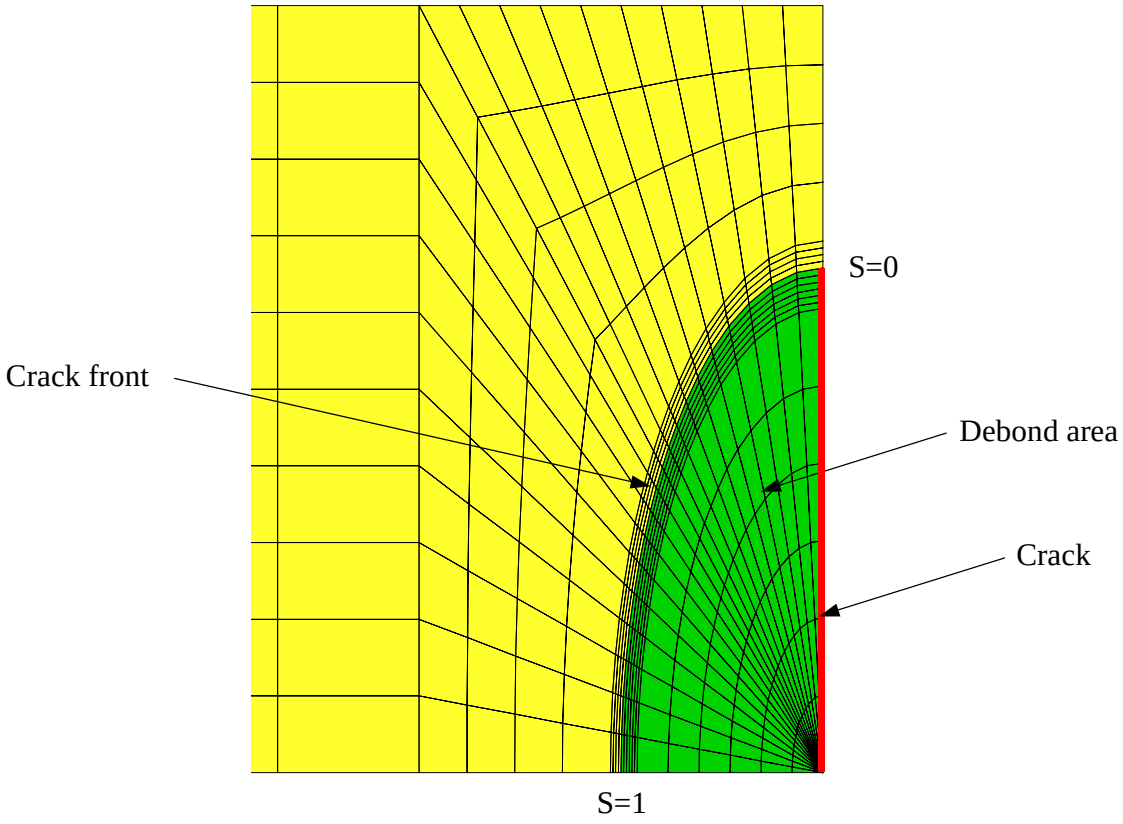

Figure 6.12. Finite element model of the debond area.

The shaded region in Fig. 6.12 represents the initial debond. The triangular elements of the corner are collapsed quadrilateral elements with two coincident nodes.

The modified crack closure integral method is extended to three-dimensional geometries to compute the total strain energy release rate, G_T, at the crack front. For comparison purposes, these values are normalized with respect to the applied stress multiplied by the shell's thickness, σh_c. Figure 6.13 shows the values obtained compared with values from Naboulsi and Mall (1997).

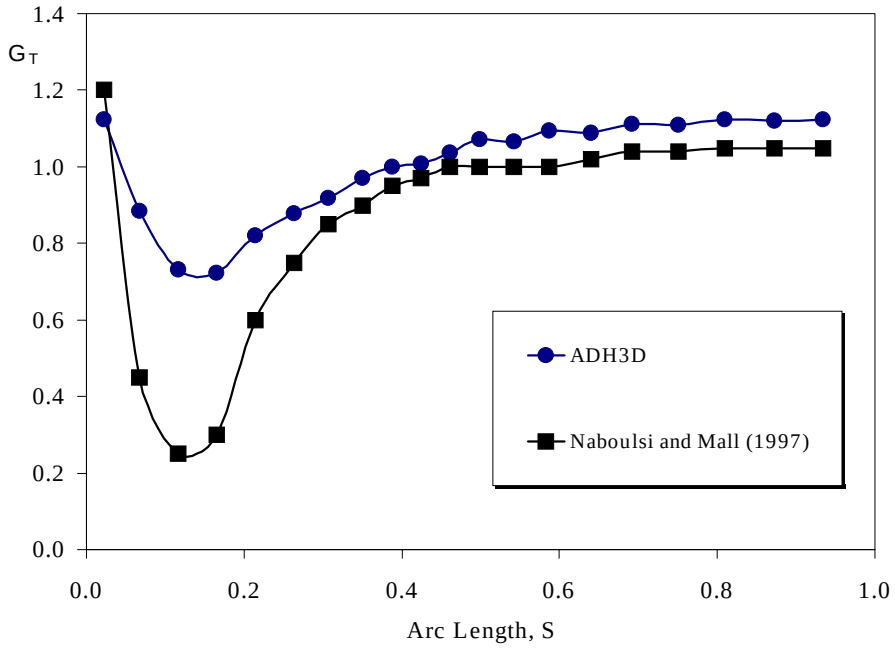

Figure 6.13. Strain energy release rate along the debond front for a crack-patch repair geometry with elliptical debond.

There is good agreement between both solutions shown in Fig. 6.13; the most critical region is in the vicinity of the crack tip. Experiments showed that the largest debond growth occurs in that region (Denney and Mall 1996, as referenced in Naboulsi and Mall 1997).

Using the Paris-Erdogan form of the proposed fatigue crack-growth law (Eq. 6.9), crack or debond extensions are computed. The load considered is represented in Fig. 6.14.

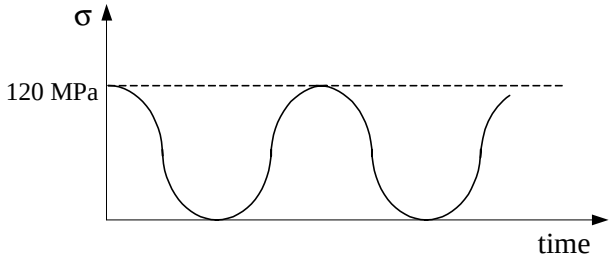

Figure 6.14. Cyclic load applied to the crack-patch repair geometry.

Since the minimum tension is zero, $G_{min} = 0$, $\Delta G = G_{max}$, and Eq. 6.9 becomes

$$\frac{da}{dN} = D G_{max}^{n} \tag{6.13}$$

where $D = 1.903 \times 10^{-18}$ and $n = 3.59$ (Kinloch and Osiyemi 1993). These values correspond to a cold-cured epoxy-paste adhesive. Crack extensions are obtained with Eq. 6.12 and a predefined number of 1,000,000 cycles.

Once crack or debond length extensions are computed, a new crack front can be defined. Next, the mesh is updated in the vicinity of the debond line. The updated mesh in the debond area is shown in Fig. 6.15.

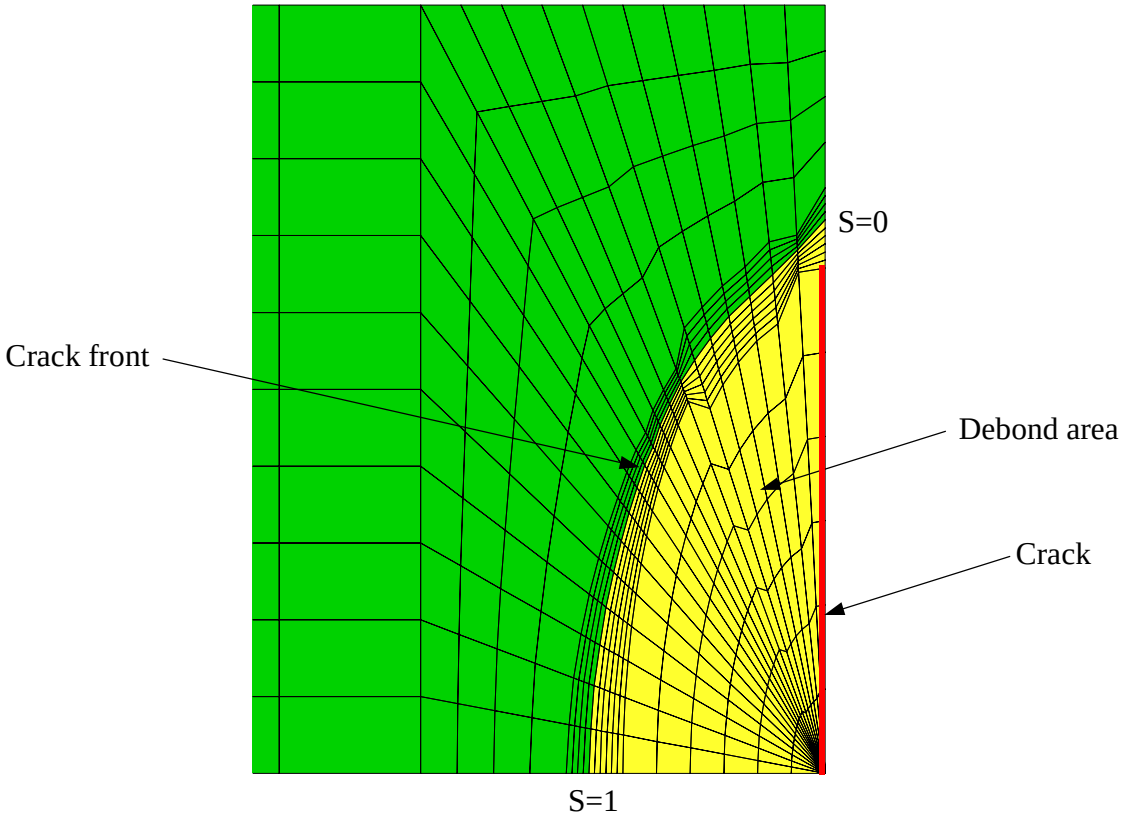

Figure 6.15. Finite element model of the debond area of the crack-patch repair geometry with updated elliptical debond after 1,000,000 cycles.

As expected, the new debond area is largest in the region around the crack tip, which agrees with experimental results (Denney and Mall, 1996 as referenced in Naboulsi and Mall 1997). This procedure can be continued to track the debond process; Figure 6.16 shows the debond area after 4,000,000 cycles.

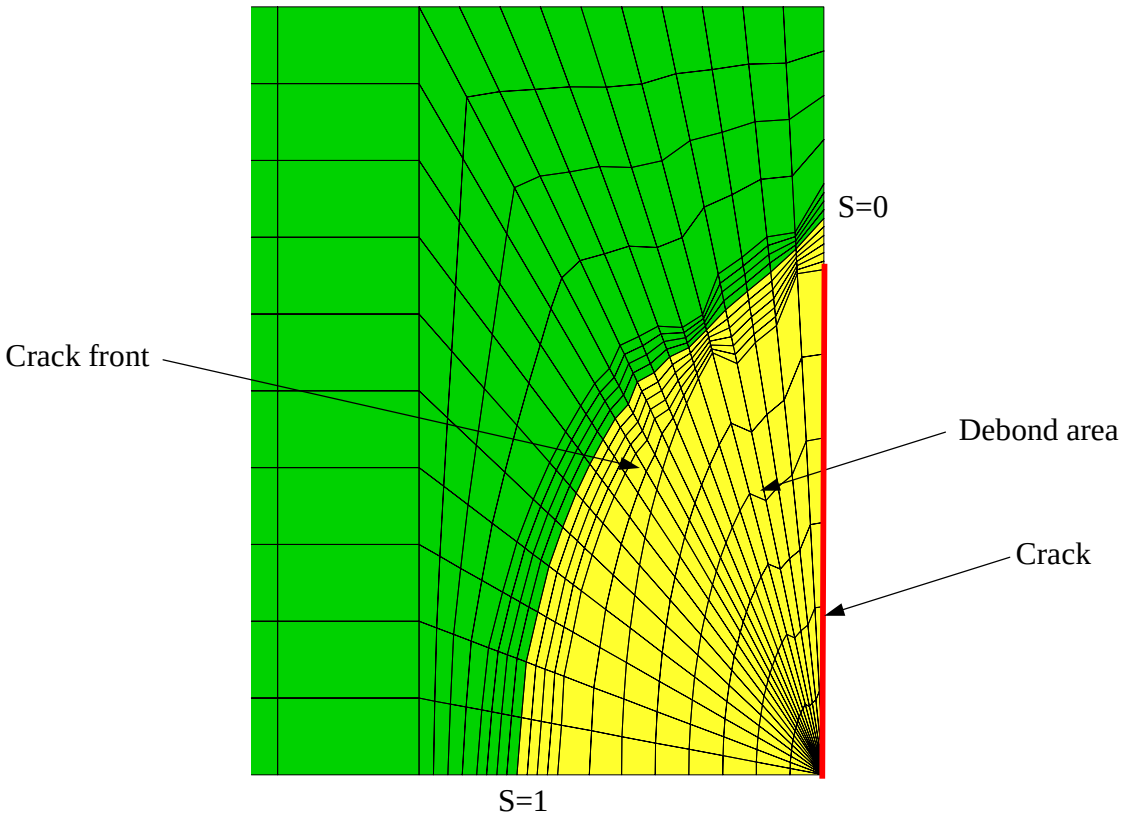

Figure 6.16. Finite element model of the debond area of the crack-patch repair geometry with updated elliptical debond after 4,000,000 cycles.

6.8 Summary and Conclusions

The usefulness of the three-dimensional adhesive finite element to compute fracture mechanics parameters has been demonstrated. Specifically, a cracked lap-shear specimen, which corresponds to the equal adherend example in the Johnson round-robin paper (1987), was analyzed with the three-dimensional adhesive finite element model. Results compared very well with those obtained with the three-dimensional analysis by

Lof (Johnson 1989). Distributions of strain energy release rates, total and for each mode, follow the expected variation and tend towards the plane-strain state at the longitudinal plane of symmetry of the specimen.

The algorithm implemented to simulate the debond process in a crack-patch repair geometry produced results which agree with those by Denney and Mall (1996), referenced in Naboulsi and Mall (1997). Although the literature on this problem is not very extensive, recent works by Naboulsi and Mall (1997) agrees with the results obtained with the adhesive finite element model. Values of strain energy release rates along the crack front agree with those of the adhesive finite element model within 5%. Only in a region of S values between 0.05 and 0.15 (Fig 6.12) is discrepancy larger; this suggests the need for a finer finite element mesh than the one used.

In summary, the capability of the three-dimensional adhesive finite element model to predict fatigue life of adhesive joints and adhesively bonded patch repairs of cracked shells has been demonstrated. Reasonably accurate results are obtained with relatively coarse meshes. The three-dimensional adhesive finite element model is an efficient tool for the analysis of adhesive structures, including fracture mechanics and fatigue considerations.

Chapter 7

Conclusions and Recommendations

7.1 Summary

Two- and three-dimensional versions of a finite element model, which includes geometrical nonlinearities, is presented. Fracture mechanics parameters are obtained with both models. They agree with results from standard finite element analysis and with well-known analytical expressions. An algorithm for durability analyses of crack-patch repair geometry is also presented.

The two-dimensional adhesive finite element model represents the adherends as Bernoulli/Euler beams and the adhesive layer as a single plane-strain/stress element through the thickness of the adhesive layer. The element satisfies C^0 continuity in the adhesive/adherend interfaces, which means that special interpolation functions were selected for the continuum element representing the adhesive. These interpolation functions are cubic Hermite polynomials in the axial direction and linear Lagrange polynomials in the transverse direction. The degrees of freedom of the adhesive layer are condensed out into the degrees of freedom of the adherends; in other words, the adhesive element has its nodes “offset” to those in the beams elements which model the adherends. This allows the reduction in the number of degrees of freedom needed to model adhesive joints consisting of beam-like adherends.

Geometrically nonlinear effects are considered in the finite element formulation. An updated Lagrangian formulation is adopted for this model. The modified Newton-Raphson method is used for the solution of the nonlinear system of equations. Thermal and moisture expansion of both the adhesive and the adherend are also included in the formulation.

The three-dimensional adhesive finite element models the adherends as shells and the adhesive layer as a three-dimensional solid element, “brick”, with offset nodes. Specifically, the degrees of freedom of the adhesive element are condensed out into the degrees of freedom of the shells, which model adjacent adherends. The adherends are modeled as shells instead of plates used in the previous work by Taylor, (1996). Shells are more efficient than plates for modeling curved members, which frequently appear in adhesive joints. These shell models are based on the Mindlin theory, which includes shear deformations.

An updated Lagrangian formulation is adopted to consider geometrically nonlinear effects, and the nonlinear system of equations generated is solved with the modified Newton-Raphson Method. Thermal and moisture effects are also included in the model. The element is limited to linearly elastic materials.

A computer implementation of the two- and three-dimensional adhesive finite element model was written in FORTRAN. The three-dimensional version has mesh generator commands and the output can be specialized to generate graphical representation of the results. The two- and three-dimensional versions can run on any ordinary personal computer, and the adhesive finite element model can also be included in the element library of general purpose finite element programs such as ABAQUS (1997).

An algorithm to study debonds of adhesive joints and crack patch geometries is proposed. The modified crack closure integral method is used to compute fracture mechanics parameters. A form of the Paris-Erdogan equation is used as a crack-growth fatigue law. Debond extension is computed and a local re-meshing is performed in the crack-front area.

A special computer program to generate elliptical meshes was written in FORTRAN. It complements the adhesive finite element program generating the mesh in the region

around the crack front. The program also updates the mesh to consider the crack extensions caused by fatigue phenomena.

7.2 Conclusions

Single lap joints were analyzed with the two–dimensional adhesive finite element model. Results compare very well with those obtained from a standard finite element analysis (ABAQUS 1997). The geometric nonlinear behavior agrees with results from ordinary finite element analysis. For relatively small loads or stiff structures, geometric nonlinearities do not produce important effects in single lap joints.

A crack lap shear specimen was analyzed and strain energy release rates were obtained and compared with results from other finite element analyses and analytical expressions; there is an excellent agreement among all of the solutions. The two-dimensional adhesive finite element model together with the modified crack closure integral method yield reliable values of strain energy release rates, even for relatively coarse meshes.

The geometrically nonlinear adhesive finite element model was used to obtain stress distributions in single lap joints. Results show clearly the importance of the third dimension in the analysis. Results were compared with two-dimensional analyses from well-known analytical expressions and with three-dimensional finite element analyses.

A crack-patch repair specimen was also modeled and results correspond to those from the previous work by Taylor (1996). The shell/brick element assembly was able to capture stress concentrations at the edges and at the corner of the patch, which were not reflected in Taylor's (1996) results.

Modeling a single lap joint subjected to various levels of load tested geometric nonlinear capabilities. Results compare well with the two-dimensional geometric nonlinear analysis by Tsai and Morton (1994a).

Fracture mechanics parameters were computed for a crack lap shear using the three-dimensional adhesive finite element model. Strain energy release rates along the width of the specimen were obtained and good agreement with the three-dimensional analysis found in the literature (Johnson 1987) was found. Three-dimensional values are found to be higher than two-dimensional ones. This suggests that two-dimensional analysis is not able to represent all the three-dimensional effects, even if the specimen has a predominantly two-dimensional geometry. Strain energy release rates for a crack-patch repair specimen with an elliptical debond were obtained along the debond line. Results are reasonably close to those from others studies.

An algorithm to represent debonding by fatigue was implemented and applied to a crack-patch repair scenario with an initial elliptical debond. Results seem to be reasonable and the predicted debond shows a pattern observed experimentally. Unfortunately, not much information about this topic is available at the moment, even though a large amount of work is currently going on.

In summary, strength of material stress distributions, fracture mechanics parameters, and debond predictions caused by cohesive cracks in the adhesive layer can be obtained with less effort than conventional finite element models. Therefore, the three-dimensional geometrically nonlinear adhesive finite element model seems to be an efficient and useful tool to analyze configurations where composite or metallic materials are bonded using relatively stiff adhesives.

7.3 Future Work and Recommendations

The two- and three-dimensional adhesive finite element model can be improved in several areas. The following recommendations are made.

1. The inclusion of material nonlinearities in the formulation would represent an important contribution to broaden the applicability of this model because, in many real situations, materials do not follow a linear law.

2. The extension of two- and three-dimensional models to include stepped adherends and tapered adhesive layers would facilitate the analysis of real structures because these configurations are widely used by the industry.

3. The consideration of a visco-elastic formulation of the model is recommended, because adhesives are polymeric materials which frequently have important time dependent effects.

4. Dynamic finite element analysis could eventually be added to the model.

5. The improvement of the user-interface to facilitate input data and interpretation of results is recommended.

6. The addition of mid-side nodes in the adhesive layer with degree of freedom condensed out into the adherend's degrees of freedom would be a good improvement when more information is needed along the thickness of the adhesive layer.

7. The evaluation of the performance of the model for different geometries and load conditions would be helpful to find limitations and to propose improvements.

8. The implementation of a general re-meshing technique to update the mesh during the simulation of the debond process is recommended. The re-meshing process should be automated.

9. The use of analytical and hybrid elements which include the singularity caused by the crack would reduce the need of re-meshing to update the finite element model to consider crack extensions.

10. The inclusion in the formulation of the shell, which models the adherends, of the penalty terms that avoid the shear locking phenomenon is recommended when thin structures are considered.

REFERENCES

ABAQUS (1997). *General-Purpose Finite Element System*, Hibbit, Karlson & Sorensen, Inc, 100 Medway Street, Providence, RI.

Adams, R. D. and Mallick, V. (1992). 'A method for the stress analysis of lap joints', *J. Adhesion* **38**, 199-217.

Adams, R. D. and Peppiatt, N. A. (1973). 'Effect of Poisson's ration strains in adherends on stresses of an idealized lap joint', *J. Adhesion* **8**, 134-139.

Adams, R. D. and Wake, W. C. (1991). *Structural Adhesive Joints*, Elsevier Science Publishers Ltd, London, UK.

Akin, J. E. (1976). 'The generation of elements with singularities', *Int. J. Num. Meth. Engng.* **10**, 1249-1260.

Allman, D. J. (1977). 'A theory for elastic stresses in adhesive bonded lap joints', *Quaterly J. Mechanics and Applied Mathematics* **30**, 415-436.

Amijima, S. and Fujii, T. (1987). 'A microcomputer program for stress analysis of adhesive-bonded joints', *Int. J. Adhesion and Adhesives* **7**, 199-204.

Aminpour, M. A. and Holsapple, K. A. (1991). 'Near-field solutions for propagating cracks at the interface of dissimilar anisotropic elastic materials', *Engng. Fracture Mech.* **36**, 93-103.

Badari Narayana, K., Dattaguru, B., Ramamurthy, T. S., andVijayakumar, K. (1994). 'A general procedure for modified crack closure integral in 3D problems with cracks', *Engng. Fracture Mech.* **27**, 167-176.

Baker, A. A. and Jones, R. (1988). *Bonded Repair of Aircraf Structures*, Martinus Nijhoff, New York.

Barbero, E. J. and Reddy, J.N. (1992). 'The jacobian derivative method for three-dimensional fracture mechanics', *Communications in Applied Numerical Methods* **6**, 507-518.

Barsoum, R.S. (1976). 'On the use of isoparametric finite elements in linear fracture mechanics', *Int. J. Num. Meth. Engng.* **10**, 25-37.

Bathe, K.J. (1996). *Finite Element Procedures*, Prentice-Hall, Englewood Cliffs, New Jersey.

Belytschko, L. and Lu, Y. Y., (1994). 'Fracture and crack growth by element free Galerkin methods', *J. Modelling Simul. Mater. Sci. Eng.* **2**, 519-534.

Benzley, S. E. (1974). 'Representation of singularities with isoparametric finite elements', *Int. J. Num. Meth. Engng.* **8**, 537-207.

Bigwood, D. A. and Crocombe, A. D. (1989). 'Elastic analysis and engineering design formulae for bonded joints.' *Int. J. Adhesion and Adhesives* **9**, 229-242.

Bigwood, D. A. and Crocombe, A. D. (1990). 'Non-linear adhesive bonded joint design analysis.' *Int. J. Adhesion and Adhesives* **10**, 31-41.

Brussat, T. R., Chiu, S.T., and Mostovoy, S., (1977). ' Fracture mechanics for structural adhesive bonds-final report', *AFML-TR-77-163, Air Force Materials Laboratory*, Wright-Patterson AFB, Ohio.

Byskov, E. (1970). 'The calculation of stress intensity factors using the finite element method with cracked elements', *Int. J. of Fracture Mechanics* **6**, 159-167.

Carpenter, W. C. and Barsoum, R. (1989). 'Two finite elements for modeling the adhesive in bonded configurations', *J. Adhesion* **30**, 25-46.

Chan, S. K., Tuba, I. S., and Wilson, W. K. (1970). 'On the finite element method in linear fracture mechanics', *Engineering Fracture Mechanics* 21-17.

Chen, D. and Cheng, S. (1983). 'An Analysis of Adhesive-Bonded Single-Lap Joints', *J. of Applied Mechanics* **50**, 109-115.

Chiu, W. K. and Jones, R. (1992). 'A numerical study of adhesively bonded lap joints', *Int. J. Adhesion and Adhesives* **12**, 219-225.

Cook, R. D., Malkus, D. S., and Plesha, M. E. (1989). *Concepts and Applications of Finite Element Analysis*, 3rd Ed. John Wiley and Sons, Inc. New York.

Cooper, P. A. and Sawyer, J. W. (1979). 'A critical examination of stresses in an elastic single lap joint', *NASA TP 1507*.

Crisfield, M. A. (1991). *Non-linear Finite Element Analysis of Solids and Structures*. Wiley & sons, New York.

Crocombe, A. D. and Bigwood, D. A. (1992). 'Development of a full elasto-plastic adhesive joint design analysis', *J. Strain Analysis* **27**, 211-218.

Davidson, B. D., Hu, H., and Schapery, R. A. (1995). 'An analytical crack-tip element for layered elastics structures', *Transactions of the ASME* **62**, 294-305.

Dattaguru, B., Everett Jr., R. A., Whitcomb, J. D., and Johnson, W. S. (1984). 'Geometrically nonlinear analysis of adhesively bonded joints', *J. Eng. Mat. and Tech.* **106**, 59-65.

Delale, F. and Erdogan, F. (1981). 'Viscoelastic analysis of adhesively bonded joints', *J. Applied Mechanics* **48**, 331-338.

Demarkles, L. R. (1955). 'Investigation on the use of rubber analogue in the study of the stress distribution in riveted and cemented joints', *NASA TN3413*.

Ewalds, H. L. and Wanhil, R. J. (1984). *Fracture Mechanics*, Edward Arnold, London, UK.

Fawkes, A. J., Owen, D. R. J., and Luxmoore, A. R. (1979). 'An assesment of crack tip singularity models for use with isoparametric elements', *Engineering Fracture Mechanics* **11**, 143-159.

Forman, R. G., Kearney, V. E., and Engel, R. M. (1967). 'Numerical analysis of crack propagation in cyclic-loaded structures'. *Trans. ASME, J. Basic Engng.* **89**, 459-463.

Goland, M. and Reissner, E. (1944). 'The stresses in cemented joints', *J. Applied Mechanics* **11**, A17-A27.

Haber, R. B. and Koh, H. M. (1985). 'Explicit expressions for energy release rates using virtual crack extensions', *Int. J. Num. Meth. Engng.* **21**, 301-315.

Harris, J. A. and Adams, R. D. (1984). 'Strength prediction of bonded single lap joints by non-linear finite element methods', *Int. J. Adheshion and Adhesives*, 65-78.

Hart-Smith, L. J. (1973). 'Further developments in the design and analysis of adhesive-bonded structural joints', Douglas Aircraft Co. Report 6922.

Hellen T. K. (1975). 'On the method of virtual crack extensions', *Int. J. Num. Meth. Engng.* **9**, 187-207.

Hellen T. K. (1989). 'Virtual crack extension method for non-linear materials', *Int.J. Num. Meth.Engng,* **28**, 929-942.

Henshell, R. D. and Shaw, K. G. (1975). 'Crack tip elements are unnecessary', *Int. J. Num. Meth. Engng.* **9**, 495-509.

Holzer, S. M., Watson, L. T., and Vu, P. (1981). 'Stability analysis of Lamella domes', *Proceedings of the ASCE Symposium on Long Span Roof Structures*, St. Louis, MO, 179-209.

Jeandrau, J. P. (1991). 'Analysis and design data for adhesively bonded joints', *Int. J. adhesion and adhesives* **11**, 71-79.

Johnson, W. S. (1987). 'Stress analysis of the cracked-lap-shear specimen: an ASTM round-robin', *J. of Testing and Evaluation*, 303-324.

Kinloch, A. J., and Osiyemi, S. O. (1993). 'Predicting the fatigue life of adhesively-bonded joints', *J. Adhesion* **43**, 79-90.

Lai, Y. H. and Dillard, D. A. (1995), 'The crack lap shear specimen revisited: a closed-form solution', *Int. J. Solids and Structures*, (in press).

Levy, N., Marcal, P. V., Ostergen, W. J., and Rice, J. R. (1971). 'Small scale yielding near a crack in plane strain: a finite element analysis', *Int. J. Fracture Mech.* **7(2)**, 143.

Lin, C. and Liechti, K. M. (1987). 'Similarity concepts in the fatigue fracture of adhesively bonded joints', *J. Adhesion* **21**, 1-24.

Meguid, S. A. (1989). *Engineering Fracture Mechanics*. Elsevier Science Publishers Ltd., London, UK.

Mostovoy, S. and Ripling, E. J. (1975) *In Adhesion Science and Technology*, Plenum Press, N. Y., **9B**, 513-562.

Muskhelishvili, N. I. (1963). *Some Basic Problems of the Mathematical Theory of Elasticity* (2nd ed. translated 1962) by J. R. M. Radok from the 4th Russian ed. (1954). Noordhoff, Groningen, The Netherlands.

Naboulsi S. and Mall S. (1997). 'Thermal effects on adhesively bonded composite repair of cracked aluminum panels', *Theoretical and Applied fracture Mechanics* **26**, 1-12.

Nikishkov, G. P. and Atluri, S. N. (1987). 'Calculation of fracture mechanics parameters for an arbitrary three-dimensional crack, by the 'equivalent domain integral' method', *Int. J. Num. Meth. Engng.* **24**, 1801-1821.

Oplinger, D. W. (1991). 'A layered beam theory for single lap joints', *U. S. Army Materials Technolgy Laboratory*, Report # MTL TR 91-23.

Owens, D. R. J. and Fawkes, A. J. (1983). *Engineering Fracture Mechanics: Numerical Methods and Applications*, Pineridge Press Ltd., Swansea, UK.

Paris, P. C. and Erdogan, F. (1963). 'A critical analysis of crack propagation laws', *Trans. ASME, J. Basic Engng.* **85**, 528-534.

Parks, D. M., (1974). 'A stiffness derivative finite element technique for determination of crack-tip stress intensity factors', *Int. J. Fracture* **10**, 487-502.

Rao, A. K., Raju, I. S. and Krishna Murty, A. V. (1971).'A powerful hybrid method in finite element analysis', *Int. J. Num. Meth. Engng.* **3**, 389-403.

Ratwani, M. M. (1979). 'Analysis of cracked adhesively bonded laminated structures', *AIAA J.* **17**, 988-994.

Renton, W. J. and Vinton, J. R. (1977). 'Analysis of adhesively bonded joints between panels of composite materials', *J. Applied Mechanics* **44**, 101-106.

Reddy, J.N (1993). *An Introduction to the Finite Element Method*, 2nd Ed. McGraw-Hill INC, New York.

Rice, J. R. (1968). 'A path-independent integral and the approximate analysis of strain concentration by notches and cracks', *Trans. ASME J. Appl. Mech.* **35**, 379-386.

Richardson, G., A. D. Crocombe, and P. A. Smith. (1993). 'A comparison of two- and three- dimensional finite element analyses of adhesive joints', *Int. J. Adhesion and Adhesives* **13**, 193-200.

Rybicki, E. F. and Kanninen, M. F. (1977). 'A finite element calcultion of stress intensity factors by a modified crack closure integral', *Engrg. Fracture Mech.* **9**, 931-938.

Shivakumar, K. N., Tan, P. W., and Newman, J. C. Jr. (1988). 'A virtual crack-closure technique for calculating stress intensitive factors for cracked three dimensional bodies', *Int. J. Fracture* **56**, R43-R50.

Sun, C. T., Klug, J., and Arons, C. (1996). 'Analysis of cracked aluminium plates repaired with bonded composite patches', *AIAA J.* **34**, 369-374.

Taylor, M. W. (1996). *Special finite elements for modelling adhesively bonded joints in two- and three-dimensions.* Thesis submitted in partial fulfillment of the Ms. of Science degree in the Engineering Mechanics Dept. of Virginia Polytechnic Institute and State University, Blacksburg, VA.

Tong, P., Pian, T. H. H., and Larry, S. J. (1973). 'A hybrid-element approach to crack problems in plane elasticity', *Int. J. Num. Meth. Eng.* **7**, 297-308.

Tracey, D. M. (1971). 'Finite elements for determination of crack tip elastic stress intensity factors', *Engr. Fracture Mech.* **3**, 255-266.

Tracey, D. M. and Cook, T. S. (1977). 'Analysis of power type singularities using finite elements', *Int. J. Num. Meth. Engng.* **11**, 1225-1235.

Tsai, M. Y. and Morton, J. (1994a). 'An evaluation of analytical and numerical solutions to the single-lap joint', *Int. J. Solids Structures* **31**, 2537-2563.

Tsai, M. Y. and Morton, J.(1994b). 'Three-dimensional deformations in a single-lap joint', *J. of Strain Analysis* **29**, 137-145.

Volkerson, O. (1938). 'Die Nietkraft Verteilung in Zugbeanspruchten mit Konstanten Laschenquerschritten', *Luftfahrtforschung* **15**, 41-47.

Weissberg, V. and Arcan, M. (1992). 'Invariability of singular stress fields in adhesive bonded joints', *Int. J. of Fracture* **56**, 75-83.

Wooley, G. R. and Carver, D. R. (1971). 'Stress concentration factors for bonded lap joint', *J. Aircraft* **8**, 817-820.

Yadagiri, S., Papi Reddy, C., and Sanjeeva Reddy, T. (1987). 'Viscoelastic analysis of adhesively bonded joints', *Computers and Structures* **27**, 445-454.

Appendix A

Analytical Cracked Adhesive Finite Elements

Introduction

The calculation of stress intensity factors with finite element methods is becoming increasingly popular, but it is still a difficult task (Fawkes et al. 1979). A large number of methods have been formulated but an adequate representation of the crack tip singularity is a common problem for most of these approaches. Fortunately, the form of the singularity for linear fracture mechanics is unique and well known. A classification of the different methods is presented.

Elements with special shape functions were introduced by Levi et al. (1971), who modeled the $1/\sqrt{r}$ singularity by overlapping two nodes of a four-node element and reducing it to a triangular element. The two overlapped nodes represent the crack tip. This approach facilitates a radial distribution of displacements. Special interpolation functions model the $\sqrt{r}$ strain singularity at the crack tip. Henshell and Shaw (1975) simplified the procedure by just moving two mid-side nodes of an 8-node isoparametric element to the quarter position. This automatically produces $1/\sqrt{r}$ singularities at the crack tip. This element have proven to give excellent results (Fawkes et al. 1979), but it does not model the traction- free condition at the crack face. Henshell and Shaw (1975) demonstrated that this effect is negligible if fine meshes are used in the vicinity of the crack tip.

Benzley (1974) first used elements with standard shape functions. He used regular rectangular elements and imposed the $1/\sqrt{r}$ singularity at the crack tip by superposition of a special function. These elements present displacement incompatibility when they are connected to the regular finite elements modeling the rest of structure. This

nonconformity can be corrected by specifying that the singularity functions are zero at the boundaries of the element.

Elements based on analytical solutions allow the computation of fracture mechanics parameters and crack extensions without the generation of a new finite element mesh; this is achieved by redefining the crack tip position. Owens and Fawkes (1983) developed an analytical element for an eight-node rectangular element. The element stiffness matrix is formulated in standard form, but the displacement field is expressed in terms of mode I and II coefficients. This element models the region where the crack tip is located; when it is connected to the regular finite elements, which model the rest of the structure, equilibrium conditions are violated. Owens and Fawkes (1983) developed an interface element to connect the analytical element to ordinary finite elements; they called it a matching element.

Hybrid elements were developed to solve the displacement incompatibility at the boundary between analytical and ordinary finite elements. This condition can be removed by imposing equal displacements in both elements at their common boundaries. Using Lagrange multipliers in the energy functional can enforce this condition.

In this study, an extension to three-dimensional geometries of Owens and Fawkes', (1983) analytical element is proposed. The specialization to the three-dimensional adhesive finite element model is also presented. This technique looks promising for modeling cracked elements and crack propagation because it greatly reduces the need for re-meshing and it represents the singularity exactly. The objective is to use this approach to model debonds in adhesive joints and patches using relatively few degrees of freedom.

7.2 Element Formulation

The derivation of the stiffness matrix of a finite element can be based on displacement or stress fields. If a displacement field is used, the formulation is a stationary potential energy operation. If a stress field is used, the formulation is a stationary complementary

energy operation. If stress and displacements are used in the formulation, it is reasonable to expect results somewhere in between these two bounds. Formulations based on displacements and stress fields are called mixed formulations.

The formulation is based on the classical energy functional

$$\pi = U - W = \frac{1}{2}\int_V \sigma^T D\sigma dV - \int_s u^T T dS \qquad \text{(A-1)}$$

where

U = strain energy
W = work done by surface tractions
σ = stress vector
u = displacement vector
T = prescribed surface tractions
V = element volume
S = boundary surface with applied tractions

The analytical expressions for stress and displacement fields for an edge crack in a semi-infinite continuum are used to formulate the analytical cracked adhesive element. The stresses can be written as

$$\begin{Bmatrix} \sigma_x \\ \sigma_y \\ \sigma_z \\ \tau_{xy} \\ \tau_{yz} \\ \tau_{xz} \end{Bmatrix} = \sum_{n=1}^{\infty} \frac{n}{2} r^{(n/2-1)} \left[a_n^I \begin{Bmatrix} f_x^I(\theta, n) \\ f_y^I(\theta, n) \\ f_z^I(\theta, n) \\ 0 \\ 0 \\ f_{xz}^I(\theta, n) \end{Bmatrix} + a_n^{II} \begin{Bmatrix} f_x^{II}(\theta, n) \\ f_y^{II}(\theta, n) \\ f_z^{II}(\theta, n) \\ 0 \\ 0 \\ f_{xz}^{II}(\theta, n) \end{Bmatrix} + a_n^{III} \begin{Bmatrix} 0 \\ 0 \\ 0 \\ f_{xy}^{III}(\theta, n) \\ f_{yz}^{III}(\theta, n) \\ 0 \end{Bmatrix} \right] \qquad \text{(A-2)}$$

and displacements can be expressed as

$$\begin{Bmatrix} u \\ v \\ w \end{Bmatrix} = \sum_{n=1}^{\infty} \frac{1}{G}\left(\frac{r}{2\pi}\right)^{n/2} \left[a_n^{I} \begin{Bmatrix} f_u^{I}(\theta,n) \\ f_v^{I}(\theta,n) \\ 0 \end{Bmatrix} + a_n^{II} \begin{Bmatrix} f_u^{II}(\theta,n) \\ f_v^{II}(\theta,n) \\ 0 \end{Bmatrix} + a_n^{III} \begin{Bmatrix} 0 \\ 0 \\ f_w^{III}(\theta,n) \end{Bmatrix} \right] \tag{A-3}$$

Equations (A-2) and (A-3) can be written in matrix form as

$$\sigma = Pa \tag{A-4}$$

$$u = Aa \tag{A-5}$$

where

$$P = \begin{bmatrix} \frac{1}{2}r^{-1/2}f_x^{I}(\theta,1) & f_x^{I}(\theta,2) & \cdots & \frac{1}{2}r^{-1/2}f_x^{II}(\theta,1) & f_x^{II}(\theta,2) & \cdots & 0 & 0 & \cdots \\ \frac{1}{2}r^{-1/2}f_y^{I}(\theta,1) & f_y^{I}(\theta,2) & \cdots & \frac{1}{2}r^{-1/2}f_y^{II}(\theta,1) & f_y^{II}(\theta,2) & \cdots & 0 & 0 & \cdots \\ \frac{1}{2}r^{-1/2}f_z^{I}(\theta,1) & f_z^{I}(\theta,2) & \cdots & \frac{1}{2}r^{-1/2}f_z^{II}(\theta,1) & f_z^{II}(\theta,2) & \cdots & 0 & 0 & \cdots \\ 0 & 0 & \cdots & 0 & 0 & \cdots & \frac{1}{2}r^{-1/2}f_{xy}^{III}(\theta,1) & f_{xy}^{III}(\theta,2) & \cdots \\ 0 & 0 & \cdots & 0 & 0 & \cdots & \frac{1}{2}r^{-1/2}f_{yz}^{III}(\theta,1) & f_{yz}^{III}(\theta,2) & \cdots \\ \frac{1}{2}r^{-1/2}f_{xz}^{I}(\theta,1) & f_{xz}^{I}(\theta,2) & \cdots & \frac{1}{2}r^{-1/2}f_{xz}^{II}(\theta,1) & f_{xz}^{II}(\theta,2) & \cdots & 0 & 0 & \cdots \end{bmatrix} \tag{A-6}$$

$$A = \frac{1}{G}\begin{bmatrix} \left(\frac{r}{2\pi}\right)^{1/2} f_u^{I}(\theta,1) & \frac{r}{2\pi}f_u^{I}(\theta,2) & \cdots & \left(\frac{r}{2\pi}\right)^{1/2} f_u^{II}(\theta,1) & \frac{r}{2\pi}f_u^{II}(\theta,2) & \cdots & 0 & 0 & \cdots \\ \left(\frac{r}{2\pi}\right)^{1/2} f_v^{I}(\theta,1) & \frac{r}{2\pi}f_v^{I}(\theta,2) & \cdots & \left(\frac{r}{2\pi}\right)^{1/2} f_v^{II}(\theta,1) & \frac{r}{2\pi}f_v^{II}(\theta,2) & \cdots & 0 & 0 & \cdots \\ 0 & 0 & \cdots & 0 & 0 & \cdots & \left(\frac{r}{2\pi}\right)^{1/2} f_w^{III}(\theta,1) & \frac{r}{2\pi}f_w^{III}(\theta,2) & \cdots \end{bmatrix} \tag{A-7}$$

$$a = \begin{Bmatrix} a_1^{I} & a_2^{I} & \cdots & a_1^{II} & a_2^{II} & \cdots & a_1^{III} & a_2^{III} & \cdots \end{Bmatrix}^T \tag{A-8}$$

$f_x^{I}(\theta,n)$, $f_x^{II}(\theta,n)$, $f_y^{I}(\theta,n)$, $f_y^{II}(\theta,n)$, $f_z^{I}(\theta,n)$, $f_z^{II}(\theta,n)$, $f_{xz}^{I}(\theta,n)$, $f_{xz}^{II}(\theta,n)$, $f_{xy}^{III}(\theta,n)$, $f_{yz}^{III}(\theta,n)$, $f_u^{I}(\theta,n)$, $f_u^{II}(\theta,n)$, $f_v^{I}(\theta,n)$, $f_v^{II}(\theta,n)$,, and $f_w^{III}(\theta,n)$ are functions of the angle θ and the index n. Figure A-1 shows components of the above expressions.

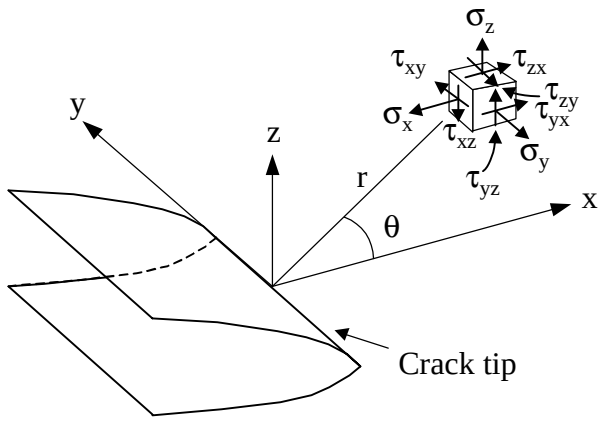

Figure A-1. Cartesian and polar coordinates with origin at the crack tip

Some vector components can be associated with the stress intensity factors for the three modes as follows

$$a_1^{I} = \frac{K_I}{\sqrt{2\pi}}$$

$$a_1^{II} = \frac{K_{II}}{\sqrt{2\pi}}$$

$$a_1^{III} = \frac{K_{III}}{\sqrt{2\pi}}$$

Assuming plane-strain conditions and an isotropic material, energy release rates are obtained as

$$G_I = (1-\nu^2)\frac{K_I^2}{E}$$

$$G_{II} = (1-\nu^2)\frac{K_{II}^2}{E}$$

$$G_{III} = (1+\nu)\frac{K_{III}^2}{E}$$

For crack extensions under mixed-mode opening modes, the total strain energy release rate is given by

$$G_T = G_I + G_{II} + G_{III}$$

The coefficients a in Eqs. A-4 and A-5 can be expressed as functions of the displacements of the adhesive, δ', by evaluating Eq. A-5 at the corners and mid-side of the adhesive element as follows:

$$\delta' = A'a \tag{A-10}$$

where $\delta' = \{u'_1 \quad v'_1 \quad w'_1 \quad \cdots \quad w'_{18}\}^T$ are the displacements in the upper and bottom faces of the adhesive element (Fig. A-2), and the matrix A' represent an interpolation of the matrices A'_i of each plane shown in Fig. A-2. Regular quadratic Lagrange polynomials are used for this interpolation. Therefore A' takes the form

$$A' = \begin{bmatrix} N_1 A'_1 & 0 & 0 \\ 0 & N_2 A'_2 & 0 \\ 0 & 0 & N_3 A'_3 \end{bmatrix}$$

and the vector a is expressed as

$$a = \begin{Bmatrix} a_1 \\ a_2 \\ a_3 \end{Bmatrix}$$

where

$$a_i = \begin{Bmatrix} a_1^I \\ a_2^I \\ \vdots \\ a_1^{II} \\ a_2^{II} \\ \vdots \end{Bmatrix}_{\text{plane i}}$$

Introducing T, the transformation matrix which relates δ' with the nodal displacement of the adherends, δ, Eq. A-10 becomes

$$\delta' = T\delta = A'a \tag{A-11}$$

where $\delta = \{u_1 \quad v_1 \quad w_1 \quad \phi_{x_1} \quad \phi_{y_1} \quad \phi_{z_1} \quad \cdots \quad \phi_{z_{18}}\}^T$ are the nodal displacements of the adherends.

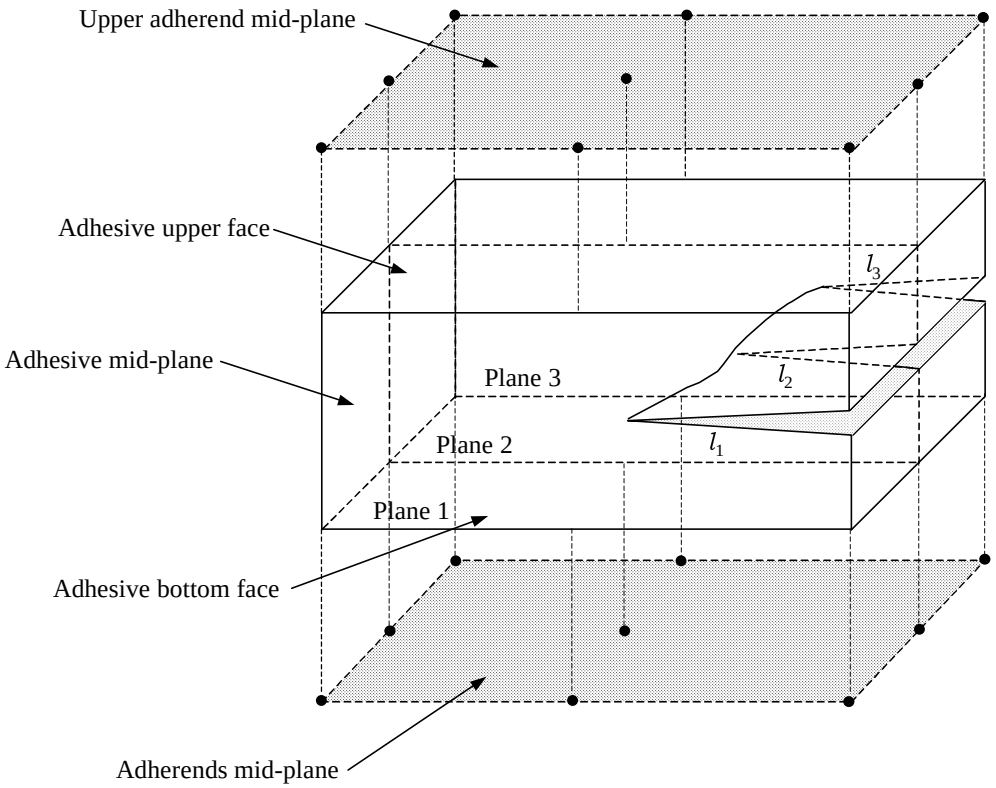

Figure A-2. Analytical adhesive element configuration

Therefore, the coefficients a are related to the nodal displacements as follows

$$A'^{-1}T\delta = \overline{A}^{-1}\delta = a \tag{A-12}$$

where $\overline{A}^{-1} = A^{-1}T$. Equation A-5 does not include rigid-body motion terms because the fracture mechanics displacement field is relative to the position of the crack front.

Therefore, displacements of the crack front need to be added to those from fracture mechanics expressions. Equation A.5 is written as

$$u - u_c = Aa$$

where $u_c = N\delta$ are the displacements of the crack front, and $N = \{N_1 \quad N_2 \quad \cdots \quad N_{108}\}$. Thus, Eq. A-11 becomes

$$\delta' = T\delta = A'a + u_c = A'a + N\delta \tag{A-13}$$

so

$$\delta[T - N] = A'a$$

Finally, Eq. A-12 is written as

$$A^{-1}[T - N]\delta = \overline{A}^{-1}\delta = a \tag{A-14}$$

where $\overline{A}^{-1} = A'^{-1}[T - N]$. Therefore, the unknown coefficients a are related to the nodal displacements of the adherends. Substituting from Eqs. A-4 and A-5 in Eq. A-1 and taking the variation with respect to the unknown coefficients a and applying Eq. A-14, a finite element model for the analytical element is obtained as

$$K\delta = F$$

where

$$K = \overline{A}^{-1^T} \int_V P^T D P dV \, \overline{A}^{-1} \tag{A-15}$$

$$F = \overline{A}^{-1^T} \int_S \overline{A}\, T dS \qquad \text{(A-16)}$$

For the adhesive finite element the matrix $\overline{A}^{-1}$ is not square; consequently, $\overline{A}$ can not be obtained. Therefore, forces F due to distributed tractions can not be discretized using Eq. A-16.

Since the matrix $\overline{A}$ depends on the nodal coordinates, it is constant over the volume of the element and, thus, is outside the integral in Eq. A-15. Therefore, defining

$$H = \int_V P^T D P dV$$

Equation A-15 can be written as

$$K = A'^{-1^T} H A'^{-1} \qquad \text{(A-17)}$$

Tractions could be discretized using a lumped criterion because the matrix $\overline{A}$ is not square and, consequently, its inverse can not be obtained.

7.3 Summary and Conclusions

An adhesive finite element has been formulated using fracture analytical mechanics solutions for the stress and displacement fields around the crack front. Accurate results for fracture mechanics parameters have been obtained using this formulation for two-dimensional cases. The objective of this section was to extend the formulation to three-dimensions and specialize the resulting expressions for the adhesive finite element presented in this work.

The application of this analytical element in the analysis of the debond process in an adhesive joint should result in a significant reduction of re-meshing needs. Once crack

extensions, Δl_i 's, are computed, values of crack lengths, l_i's, are updated and a new debond area is defined (Fig. A-5). The process can be continued until failure is reached.

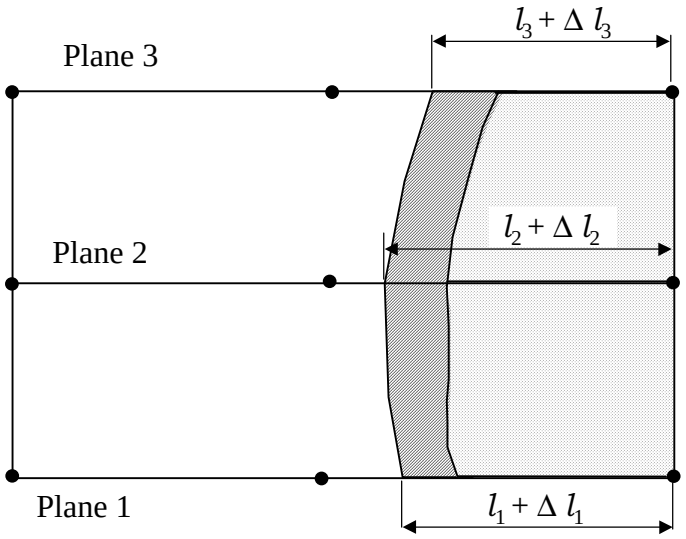

Figure A-5. Debond process using the analytical cracked adhesive element

However, some re-meshing may still be required when most of the element is debonded as shown in Fig. A-6.

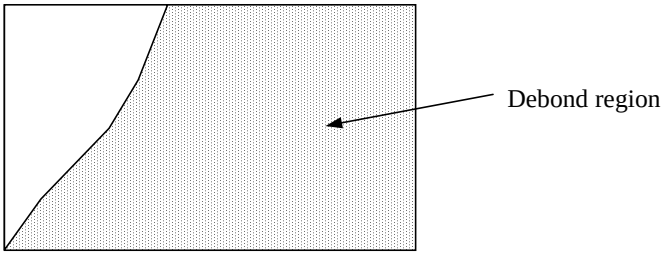

Figure A-6. Analytical cracked adhesive element requiring re-meshing

These elements satisfy internal equilibrium and compatibility, but boundary displacement continuity is violated. Therefore, convergence is not guaranteed although non-conforming element are widely used and perform successfully (Owens and Fawkes 1992). In fact, just refining the mesh should improve results of models using nonconforming elements.

This limitation can be overcome by following a hybrid technique, where conformity is enforced by including a constraint condition in the energy function formulation by the use of Lagrange multipliers.

In summary, a three-dimensional adhesive finite element model was developed to compute fracture mechanics parameters. The formulation of the model is based on the fracture mechanics analytical expressions for the stress and displacement fields. The model has not been tested yet, but the formulation seems to be promising. Non-conformability of displacements at the boundary of the element seems to be the most important limitation of the proposed model.

VITA

Raul Andruet was born in Cordoba, a city in the center of Argentina, in July of 1955. He received his civil engineering degree from the "Universidad Catolica de Cordoba" in 1979. He worked at INCONAS, a civil engineering consulting firm in Argentina, for ten years and was involved with the design and structural verification of hydroelectric power plants. In 1989 he returned to school and obtained the Master of Science degree in Civil Engineering at Virginia Polytechnic Institute and State University in 1991. He is currently completing the requirements for the Doctor of Philosophy degree in Engineering Science and Mechanics at Virginia Polytechnic Institute and State University.